



Pontifícia Universidade Católica
do Rio de Janeiro

Alessandra Carvalho de Souza e Silva

Further development of the new generation of *N*-acylhydrazones containing the 1-methylimidazole group and their evaluation against models of endocrine and neuroendocrine aggregopathies

Tese de Doutorado

Thesis presented to the Programa de Pós-Graduação em Química of PUC-Rio in partial fulfillment of the requirements for the degree of Doutor em Química.

Advisor: Prof. Dr. Nicolás A. Rey
Co-Advisor: Prof. Dr. Daphne S. Cukierman

Rio de Janeiro
March 2024



Pontifícia Universidade Católica
do Rio de Janeiro

Alessandra Carvalho de Souza e Silva

Further development of the new generation of *N*-acylhydrazones containing the 1-methylimidazole group and their evaluation against models of endocrine and neuroendocrine aggregopathies

Thesis presented to the Programa de Pós-Graduação em Química of PUC-Rio in partial fulfillment of the requirements for the degree of Doutor em Química. Approved by the Examination Committee:

Prof. Dr. Nicolás Adrián Rey

Advisor

Departamento de Química – PUC-Rio

Prof. Dr. Daphne Schneider Cukierman

Co-Advisor

UERJ

Prof. Dr. Yraima Moura Lopes Cordeiro

UFRJ

Prof. Dr. Marciela Scarpellini

UFRJ

Prof. Dr. Lívia Batista Lopes Escobar

Departamento de Química – PUC-Rio

Prof. Dr. Jones Limberger

Departamento de Química – PUC-Rio

Dr. Anna De Falco

Departamento de Química – PUC-Rio

Rio de Janeiro, March 20th, 2024

All rights reserved

Alessandra Carvalho de Souza e Silva

Graduated in Chemistry at the Federal Institute of Rio de Janeiro in 2015. Has a Master's degree in Chemical Engineering from the Federal Rural University of Rio de Janeiro (2020). Started her Ph.D. on March 2020 at PUC-Rio.

Bibliographic data

Silva, Alessandra Carvalho de Souza e

Further development of the new generation of *N*-acylhydrazones containing the 1-methylimidazole group and their evaluation against models of endocrine and neuroendocrine aggregopathies / Alessandra Carvalho de Souza e Silva ; advisor: Nicolás A. Rey ; co-advisor: Daphne S. Cukierman. – 2024.

139 f. : il. color. ; 30 cm

Tese (doutorado)–Pontifícia Universidade Católica do Rio de Janeiro, Departamento de Química, 2024.

Inclui bibliografia

1. Química – Teses. 2. *N*-acil-hidrazonas. 3. Cobre(II). 4. Doença de Alzheimer. 5. Diabetes mellitus tipo 2. I. Rey, Nicolás Adrián. II. Cukierman, Daphne Schneider. III. Pontifícia Universidade Católica do Rio de Janeiro. Departamento de Química. IV. Título.

CDD: 540

Acknowledgements

I would like to thank PUC-Rio and the Department of Chemistry, for all the support provided to carry out this work.

This study was financed in part by the *Coordenação de Aperfeiçoamento de Pessoal de Nível Superior - Brasil (CAPES)* - Finance Code 001.

To the members of this thesis committee: thank you for accepting the invitation to read and collaborate with this work.

To all collaborators (professors, student, postdocs and technicians) of this work: Álvaro for the help with NMR analyses; Dr. Claudio Fernández, Dr. Phelippe do Carmo Gonçalves and student Jesica S. Flores for the A β NMR studies; Prof Dr. Anderson de Sá Pinheiro and his student Karina de Carvalho Pougy for their help in the NMR analysis involving the hIAPP₁₈₋₂₂ peptide.

I would like to thank the *Laboratório Multiusuário de Espectrometria de Massas (LAMEM)* at Federal Fluminense University (UFF) for the ESI-MS analysis. Also, to the *Laboratório de Biologia Molecular Estrutural (LaBiME)* of the Federal University of Rio de Janeiro (UFRJ) for the support in the protein aggregation experiments.

I would like to thank my advisor Prof. Nicolás A. Rey, for accompanying me these 4 years on this academic journey in general and not only for all the assistance necessary to prepare this work, but also for teaching me the conduct and care appropriate to this profession. For your availability to answer my questions, always with excellence. Your advice, constructive criticism and reflections were indispensable throughout this journey at LABSO-Bio. Therefore, I am extremely grateful for the maturity and growth, as well as the opportunity to work in an area of research that captured my heart.

I would like to thank my co-advisor, Prof. Dr. Daphne S. Cukierman, for being a teacher as well as a friend, and for your presence from the beginning. Even before you became my mentor, you taught me and helped me in my most fragile moments. For your enviable teaching style, which made studying and learning easier throughout my doctorate, I also thank you.

To Barbara Marinho, who worked with me directly during the most difficult time, in the middle of the pandemic, but made our work fun. I am grateful for the long days doing countless replicas of experiments, in which we spent whole days, but even though we were tired, together the time was very pleasant. It was a great pleasure to work alongside you and see your evolution more and more each day.

To Dayanne Martins for the tips, advice and partnership. A great professional, thank you for everything.

To my parents, Severino and Lucrécia: if it weren't for you, I wouldn't have made it here, you are my refuge. Thank you for all your patience on the days when I felt

like giving up, but my mom was there by my side, calming me down and showing me that I can do anything I want, and that giving up is for the weak, and that I am stronger than I imagine. Mom, thank you for all hugs and for never letting go of my hand when I needed, I love you so much.

To my fiancé Alexander Katz: for showing up in my life in the middle of all the chaos and lifting me up with your support and encouragement. For your affection and conversations, because when I was stressed and tired, you showed me that I can achieve my biggest dreams. I love you immensely.

Thanks to Leonny, Fran and Cris who were PUC-Rio's gifts to me. At the beginning of this journey, the four of us studied together and helped each other in subjects that were not easy at all. To my friend Leonny, the one that keeps this group together, holding all desperate girls' outbreaks, and chided me many times. I can only say one thing, I will carry this friendship with me until the end of my life. I love my quartet.

I would like to thank anyone who somehow helped me, even if only for an instant.

The PhD represented a huge growth not only professionally, but also personally, in which I found new strength and was given the opportunity to develop intensely. Surpassing all the systemic and personal difficulties, overcoming the tribulations, I recognize myself as a better person, besides a better qualified chemist.

Abstract

De Souza e Silva, Alessandra Carvalho; Cukierman, Daphne Schneider (Co-Advisor); Rey, Nicolás Adrián (Advisor). **Further development of the new generation of *N*-acylhydrazones containing the 1-methylimidazole group and their evaluation against models of endocrine and neuroendocrine aggregopathies.** Rio de Janeiro, 2024. 139p. Tese de Doutorado - Departamento de Química, Pontifícia Universidade Católica do Rio de Janeiro.

Both Alzheimer's disease (AD) and type-2 diabetes *mellitus* (T2DM) are considered metal-enhanced aggregopathies, in which the anomalous interactions between copper(II) and the A β and IAPP peptides, respectively, lead to protein misfolding, aggregation and oxidative stress. In this scenario, our research group proposed the use of 1-methylimidazole-containing *N*-acylhydrazones as metallophores, aiming to compete with the interaction of this metal ion with amyloidogenic proteins, intervening in the process of aggregation and restoring metal homeostasis. In the present work, two new compounds of this series were proposed, based on the structure of mescaline and nicotine: **X1TMP** and **X1NIC**. The first was evaluated in biophysical models of AD using the A β ₁₋₄₀ peptide and its fragment A β ₁₋₁₆ and was compared to its unsubstituted analogue **X1Benz**. **X1NIC**, on the other hand, was synthesized separately as its (*E*) and (*Z*) isomers, and they were in turn studied using the coordinating hIAPP₁₈₋₂₂ fragment in the context of T2DM. **X1TMP** and **X1Benz** were both able to lessen the copper-mediated production of ROS and prevent A β aggregation in the presence and absence of this metal. The formation of ternary species with different stabilities was clearly demonstrated for the studied compounds in both AD and T2DM systems using different techniques. In the case of T2DM, however, only **X1NIC-(E)** seemed able to remove copper(II) from hIAPP₁₈₋₂₂ at ligand excess conditions, which is consistent with its higher affinity for this ion. It is worth mentioning that all tridentate hydrazones [**X1TMP**, **X1Benz** and **X1NIC-(E)**] presented similar, moderate, apparent affinity constant values, while **X1NIC-(Z)** had a weaker interaction with copper since it performs as a bidentate ligand. In general, these new compounds demonstrated promising metallophoric activity and proved ability to interfere with the anomalous copper-peptide interactions. It is possible that the

ternary species are enough to partially passivate the metal, avoiding deleterious redox cycling effects.

Keywords

N-acylhydrazones; copper(II); Alzheimer's disease; type 2 diabetes *mellitus*.

Resumo Expandido em Português

De Souza e Silva, Alessandra Carvalho; Cukierman, Daphne Schneider; Rey, Nicolás Adrián. **Desenvolvimento adicional da nova geração de *N*-acil-hidrazonas contendo o grupo 1-metilimidazol e sua avaliação contra modelos de agregopatias endócrinas e neuroendócrinas**. Rio de Janeiro, 2024. 139p. Tese de Doutorado - Departamento de Química, Pontifícia Universidade Católica do Rio de Janeiro.

O termo agregopatia é utilizado para definir doenças relacionadas ao dobramento incorreto e conseqüente agregação patológica de proteínas. A doença de Alzheimer (DA) caracteriza-se pela agregação do peptídeo β -amiloide ($A\beta$), enquanto o diabetes *mellitus* tipo 2 (DMT2) está relacionado ao polipeptídeo amiloide das ilhotas pancreáticas (IAPP). O dobramento defeituoso de proteínas e peptídeos leva à formação de oligômeros solúveis e tóxicos, que eventualmente acarretam morte celular. Além disto, ambas doenças apresentam uma componente endócrina (ou neuroendócrina no caso da DA), devido ao papel da insulina em suas fisiopatologias. Uma vez que a interação entre certos íons metálicos, como cobre(II), e determinados peptídeos é considerada uma das causas agravantes da agregação proteica, busca-se impedir ou atenuar as interações anômalas metal-proteína através da utilização de metalóforos hidrazônicos. Estes são compostos com afinidade moderada por biometais, desenvolvidos com o intuito de restaurar a homeostase metálica e reduzir o estresse oxidativo presente nestas doenças. Neste contexto, o presente trabalho descreve o desenvolvimento de dois novos metalóforos cujas estruturas foram inspiradas em moléculas que se ligam a receptores celulares: **X1TMP** (1-metil-1H-imidazol-2-carboxaldeído 3,4,5-trimetoxibenzoil hidrazona), baseado na mescalina, que se liga seletivamente à receptores cerebrais, e **X1NIC** (1-metil-1H-imidazol-2-carboxaldeído nicotinoil hidrazona), pensado com base na estrutura da nicotina, que apresenta receptores funcionais nas ilhotas pancreáticas e em células β . Na primeira parte do trabalho, avaliou-se o potencial metalofórico do **X1TMP** frente a modelos biofísicos de DA, utilizando o peptídeo $A\beta_{1-40}$ e seu fragmento coordenante $A\beta_{1-16}$, comparando-o com seu derivado não-substituído **X1Benz** (1-metil-1H-imidazol-2-carboxaldeído benzoil hidrazona). Os valores de log P calculados e

experimentais foram semelhantes para ambos e dentro da faixa ideal e, de maneira geral, todos os parâmetros físico-químicos avaliados estão de acordo com as diretrizes para fármacos orais direcionados ao sistema nervoso central. A partir do método de Job, foi verificado que ambas hidrazonas apresentaram interação com cobre(II) com estequiometria do tipo ML. Os valores aparentes de log K foram de $5,74 \pm 0,15$ e $5,87 \pm 0,11$ para **X1TMP** e **X1Benz** respectivamente, indicando que a presença das metoxilas não influencia na estabilidade do complexo formado. Ambos os compostos foram capazes de diminuir a produção de espécies reativas de oxigênio pelo sistema Cu(A β) sob condições pseudo-fisiológicas, com o **X1TMP** sendo ligeiramente mais eficaz do que o **X1Benz**. Além disto, as hidrazonas foram capazes de inibir a agregação de A β em condições equimolares na presença e, surpreendentemente, na ausência de cobre(II). Utilizando a técnica ^1H - ^{15}N HSQC foi possível verificar que o **X1Benz** interage diretamente com o peptídeo, o que justifica o efeito observado. Por outro lado, a inibição da agregação mediada por cobre pode ocorrer através da formação de um complexo ternário, como evidenciado por experimentos de ^1H NMR. Na segunda parte do trabalho, estudou-se o efeito do **X1NIC** no modelo de DMT2. Entretanto, uma mistura de estereoisômeros geométricos foi obtida durante a síntese, o que direcionou o estudo para comparação desses isômeros, e como ambos interagem com o sistema Cu^{2+} -hIAPP. Uma vez purificados e caracterizados, determinou-se experimentalmente os valores de coeficiente de partição octanol-água respectivamente como $0,62 \pm 0,01$ e $0,87 \pm 0,02$ para **X1NIC-(E)** e **X1NIC-(Z)**. Mais uma vez a afinidade aparente ligante-metal foi determinada, com valores de log K = $5,82 \pm 0,16$ para o isômero tridentado (E) e $5,04 \pm 0,04$ para o isômero bidentado (Z). O fragmento coordenante hIAPP₁₈₋₂₂ foi utilizado para avaliar a interação do peptídeo com o cobre(II) e o efeito dos ligantes neste sistema. Através de experimentos de RMN de alto campo, a coordenação do tipo N₃O foi confirmada para o peptídeo, evidenciando a histidina como sítio de ancoragem do metal. Ambos os isômeros formaram complexos ternários, embora com estabilidades diferentes, conforme demonstrado tanto por RMN quanto por voltametria cíclica. Por outro lado, a adição de um excesso de **X1NIC-(E)** se mostrou eficaz na remoção de cobre ligado ao peptídeo, enquanto o mesmo não foi observado para **X1NIC-(Z)**, evidenciando a necessidade de um sítio tridentado para uma boa ação metalofórica por parte destes ligantes. Vale ressaltar que

provavelmente os próprios complexos ternários sejam capazes de parcialmente neutralizar os efeitos deletérios relacionados à química redox do metal. O presente trabalho complementa o conhecimento acerca da nova geração de metalóforos hidrazônicos contendo 1-metilimidazol, trazendo novas perspectivas para suas aplicações em futuros trabalhos direcionados tanto para DA quanto para o DMT2.

Palavras-chave

N-acil-hidrazonas; cobre(II); doença de Alzheimer; diabetes *mellitus* tipo 2.

Table of contents

List of Acronyms and Abbreviations.....	1
List of Figures.....	3
List of Tables.....	8
1. Introduction.....	10
1.1. Protein aggregation.....	10
1.2. Alzheimer's disease (AD).....	12
1.3. Type 2 diabetes <i>mellitus</i> (T2DM).....	17
1.4. Relationship between aggregopathies and metals.....	21
1.5. Metallophores.....	25
2. Work Proposal.....	29
3. Objectives.....	32
3.1. General objective.....	32
3.2. Specific objectives.....	32
4. Methodology.....	33
4.1. <i>In silico</i> pharmacological analyses.....	33
4.2. Syntheses of the ligands.....	33
4.3. Characterization.....	34
4.3.1. Infrared Vibrational Spectroscopy (IR).....	34
4.3.2. Thermogravimetry (TG).....	34
4.3.3. Melting Point (MP).....	34
4.3.4. Nuclear Magnetic Resonance (NMR).....	34
4.3.5. Electrospray Ionization Mass Spectrometry (ESI-MS).....	35
4.4. Stability assay in buffered solution.....	35
4.5. X1NIC-(<i>E</i>) / X1NIC-(<i>Z</i>) temperature stability.....	35
4.6. Octanol-water partition coefficient (log P).....	36
4.7. Method of continuous variations (Job Plot).....	36
4.8. Simultaneous Cu ²⁺ interactions with X1NIC-(<i>E</i>) and X1NIC-(<i>Z</i>).....	37
4.9. Ascorbate consumption assay.....	37
4.10. A β ₁₋₄₀ aggregation.....	38
4.11. Transmission Electron Microscopy (TEM).....	38
4.12. ¹ H and ¹ H- ¹⁵ N HSQC NMR of the Cu ²⁺ -A β ₁₋₄₀ -X1Benz system.....	39

4.13.	^1H NMR of the Cu^{2+}-hIAPP₁₈₋₂₂ and the Cu^{2+}-hIAPP₁₈₋₂₂-X1NIC system	
		39
4.14.	Cyclic Voltammetry (CV) of the Cu^{2+}-hIAPP₁₈₋₂₂ and the Cu^{2+}-hIAPP₁₈₋₂₂-X1NIC system	40
5.	Results and Discussion	41
5.1.	Part I – New mescaline-related <i>N</i>-acylhydrazone and its unsubstituted benzoyl derivative as metallophores towards copper-associated models of Alzheimer’s disease	41
5.1.1.	Syntheses and characterization	42
5.1.2.	Stability towards hydrolysis in buffered solution	48
5.1.3.	Pharmacological parameters	50
5.1.4.	Interactions with copper(II) in buffered pH 7.4, aqueous solution	51
5.1.5.	Interactions with the Cu^{2+}-Aβ system: effect on ROS production	53
5.1.6.	Inhibition of Aβ aggregation via turbidity assay	55
5.1.7.	Mechanistic insights through 1D- and 2D-NMR experiments	59
5.2.	Part II – Comparison between the (<i>E</i>) and (<i>Z</i>) isomers of a nicotinic-inspired <i>N</i>-acylhydrazone towards the Cu^{2+}-bound hIAPP₁₈₋₂₂ fragment in the context of type 2 diabetes <i>mellitus</i>	63
5.2.1.	Syntheses and characterization	63
5.2.2.	Stability towards hydrolysis in buffered solution	71
5.2.3.	Thermal stability of the isomers in solution	73
5.2.4.	Pharmacological parameters	76
5.2.5.	Interactions of both isomers with copper(II) ions in solution	78
5.2.6.	Interactions of X1NIC isomers with the Cu^{2+}-hIAPP₁₈₋₂₂ system through high-field NMR	82
5.2.7.	Cyclic voltammetry study of both binary (Cu^{2+}-hIAPP₁₈₋₂₂ and Cu^{2+}-X1NIC) and ternary (X1NIC-Cu^{2+}-hIAPP₁₈₋₂₂) systems	89
6.	Conclusions	97
7.	References	100

List of Acronyms and Abbreviations

- AD – Alzheimer’s disease
- APP – Amyloid Precursor Protein
- A β – β -amyloid peptide
- BBB – Blood-Brain Barrier
- CNS – Central Nervous System
- CT- Charge Transfer
- CV – Cyclic Voltammetry
- DM – diabetes *mellitus*
- DMSO – dimethylsulfoxide
- DMSO-*d*₆ – deuterated dimethylsulfoxide
- EDTA – ethylenediamine tetraacetic acid
- ESI-MS – Electrospray Ionization Mass Spectrometry
- FDA – Food and Drug Administration
- HBA – hydrogen bond acceptors
- HBD – hydrogen bond donors
- HEPES – 4-(2-hydroxyethyl)-1-piperazineethanesulfonic acid
- hIAPP – Human Islet Amyloid Polypeptide
- hIAPP₁₈₋₂₂ – fragment of the human islet amyloid polypeptide containing the amino acid residues 18 to 22
- HPCFur – piridine-2-carboxaldehyde 2-furoyl hydrazone
- HSQC – Heteronuclear Single Quantum Coherence
- HSSNN – amino acid sequence of hIAPP₁₈₋₂₂: H – histidine, S – serine;
N - asparagine
- IAPP – Islet Amyloid Polypeptide
- IDE – insulin-degrading enzyme
- IDF – International Diabetes Federation
- INH HQ – 8-hidroxyquinoline-2-carboxaldehyde isonicotinoyl hydrazone
- IR – Infrared Vibrational Spectroscopy
- ISA – International Society of Amyloidosis
- K_{app} – apparent affinity constant
- Log P – logarithm of the 1-octanol/water partition coefficient

Log S – logarithm of solubility in water
MPACs – Metal-Protein Attenuating Compounds
MP – melting point
MW – molecular weight
NMR – Nuclear Magnetic Resonance
NOESY – Nuclear Overhauser Effect Spectroscopy
PBT2 – 5,7-dichloro-2-[(dimethylamino)methyl]quinolin-8-ol
PSA – polar surface area
RNS – reactive nitrogen species
ROS – reactive oxygen species
SUS – Unified Health System, from Portuguese *Sistema Único de Saúde*
TEM – Transmission Electron Microscopy
TFA – trifluoroacetic acid
TG – Thermogravimetry
ThT – Thioflavin-T
T2DM – Type 2 diabetes *mellitus*
Tris – tris(hydroxymethyl)aminomethane
UNPD – United Nations Population Division
UV-Vis – Ultraviolet-Visible
X1Benz – 1-methyl-1H-imidazole-2-carboxaldehyde benzoyl hydrazone
X1FUR - 1-methyl-1H-imidazole-2-carboxaldehyde 2-furoyl hydrazone
X1INH - 1-methyl-1H-imidazole-2-carboxaldehyde isonicotinoyl hydrazone
X1NIC – 1-methyl-1H-imidazole-2-carboxaldehyde nicotinoyl hydrazone
X1NIC-(E) – (E) isomer of 1-methyl-1H-imidazole-2-carboxaldehyde nicotinoyl hydrazone
X1NIC-(Z) – (Z) isomer of 1-methyl-1H-imidazole-2-carboxaldehyde nicotinoyl hydrazone
X1Thio – 1-methyl-1H-imidazole-2-carboxaldehyde 2-thiophenyl hydrazone
X1TMP – 1-methyl-1H-imidazole-2-carboxaldehyde 3,4,5-trimethoxybenzoyl hydrazone

List of Figures

Figure 1. Protein aggregation mechanism. (A) Native structure. (B) Beginning of β -sheet formation. (C) Formation of nucleus. (D) Formation of oligomers. (E) Formation of mature fibers.	11
Figure 2. Hospitalizations due to AD in each region of Brazil in the period between 2013 and 2022.	13
Figure 3. Scheme of APP cleavage through non-amyloidogenic and amyloidogenic pathways.	14
Figure 4. (A) Healthy neuron representation. (B) Neuron affected by AD.	15
Figure 5. Scheme of the protein deposits in neurons affected by Alzheimer's disease: extracellular A β peptide and intracellular tau protein.	16
Figure 6. Diabetes cases globally and divided by continents in 2021, and predictions until 2045, considering individuals in the range of 20 to 79 years old.	18
Figure 7. Processing of PreProIAPP to form the mature human IAPP.	19
Figure 8. Comparison between the peptides hIAPP, rIAPP and Pramlintide. Blue: region with high affinity for copper(II) ions (18-22); Gray: amyloidogenic region (22-28); Red: substituted amino acid residues in IAPP analogues.	20
Figure 9. Coordination patterns of A β_{1-16} binding to Cu ²⁺ at (A) slightly acidic medium (pH ~ 6.3-6.9) and at (B) slightly basic medium (pH ~ 8).	23
Figure 10. Amino acid sequence of human and rat A β peptide.	23
Figure 11. N ₃ O coordination patterns of Cu ²⁺ -hIAPP complex binding to the carbonyl oxygen (left) and to a hydroxyl group (right).	24
Figure 12. Structures of clioquinol (5-chloro-7-iodo-quinolin-8-ol) and PBT2 {5,7-dichloro-2-[(dimethylamino)methyl]quinolin-8-ol}.	26
Figure 13. Structures of INHHQ (8-hydroxyquinoline-2-carboxaldehyde isonicotinoyl hydrazone), X1INH (1-methyl-1H-imidazole-2-carboxaldehyde isonicotinoyl hydrazone), X1Fur (1-methyl-1H-imidazole-2-carboxaldehyde 2-furoyl hydrazone) and X1Thio (1-methyl-1H-imidazole-2-carboxaldehyde 2-thiophenyl hydrazone).	28
Figure 14. Structures of the new <i>N</i> -acylhydrazones considered in this work. (A) X1TMP: 1-methyl-1H-imidazole-2-carboxaldehyde 3,4,5-trimethoxy-benzoyl hydrazone. Comparison with mescaline is highlighted in orange. (B) X1NIC: 1-methyl-1H-imidazole-2-carboxaldehyde nicotinoyl hydrazone. Comparison with nicotine is highlighted in blue.	31
Figure 15. Generic scheme for the synthesis of the <i>N</i> -acylhydrazones X1TMP and X1NIC.	31
Figure 16. ESI-MS spectra (positive mode) of (A) X1TMP and (B) X1Benz in methanol.	43
Figure 17. Mid-infrared of (A) X1TMP and (B) X1Benz. Samples were prepared as KBr pellets.	44
Figure 18. ¹ H NMR spectra (400 MHz) of the studied <i>N</i> -acylhydrazones in DMSO- <i>d</i> ₆ at 25 °C. (A) X1TMP and (B) X1Benz.	46
Figure 19. ¹³ C NMR spectra (100 MHz) of the studied <i>N</i> -acylhydrazones in DMSO- <i>d</i> ₆ at 25 °C. (A) δ_{X1TMP} : 35.73, 56.29, 60.16, 105.80, 120.35, 125.60, 127.18, 131.77, 139.09, 141.02, 152.78, 162.87 ppm. (B) δ_{X1Benz} : 35.85, 120.84, 125.71, 128.01, 128.64, 129.08, 132.28, 132.48, 139.07, 163.45 ppm.	48

Figure 20. UV-Vis absorption spectra of **X1TMP** and its precursors (5×10^{-5} mol L^{-1}) in 1% DMSO/Tris (10 mmol L^{-1} , pH 7.4), obtained over a period of 12 h, at room temperature..... 49

Figure 21. UV-Vis absorption spectra of **X1Benz** and its precursors (5×10^{-5} mol L^{-1}) in 1% DMSO/Tris (10 mmol L^{-1} , pH 7.4), obtained over a period of 12 h, at room temperature..... 49

Figure 22. Method of continuous variations to evaluate the binding affinity of the new hydrazones (A) **X1TMP** and (B) **X1Benz** towards copper (II) – representative electronic spectra of ligand molar fractions from 0.5 to 1.0. *Insets:* absorbance *versus* molar fraction plots ($R^2 = 0.998$ for A and B). HEPES buffer at pH 7.4, 50 mmol L^{-1} , 25 °C. 52

Figure 23. Cu(A β)-induced ascorbate consumption. (A) **Left:** Plots showing ascorbate consumption through absorbance decrease at 265 nm for Cu(A β) (black), Cu(A β) + 1 eq. **X1TMP** (red) and Cu(A β) + 3 eq. **X1TMP** (blue). The sharp increase observed after compound addition in excess is due to the intrinsic absorbance of the resulting Cu(**X1TMP**) interaction. *Inset:* Linear segment of the ascorbate consumption curve for $0.80 \leq A_{265} \leq 0.65$. Figures of merit: black line slope: -0.09018 ± 0.00009 , $R^2 = 0.999$; red line slope: -0.05430 ± 0.00009 , $R^2 = 0.996$; blue line slope: -0.036210 ± 0.000008 , $R^2 = 1.000$. **Right:** Bar graph representing the normalized mean slopes of the linear segment, which parallel ROS production, for each condition tested. Significant differences (*t*-tests) are characterized by (*) for $p < 0.05$. (B) **Right:** Representative plots showing ascorbate consumption through absorbance decrease at 265 nm for Cu(A β) (black), Cu(A β) + 1 eq. **X1Benz** (red) and Cu(A β) + 3 eq. **X1Benz** (blue). The sharp increase observed after compound addition in excess is due to the intrinsic absorbance of the resulting Cu(**X1Benz**) interaction. *Inset:* Linear segment of the ascorbate consumption curve for $0.70 \leq A_{265} \leq 0.55$. Figures of merit: black line slope: -0.08240 ± 0.00005 , $R^2 = 1.000$; red line slope: -0.05267 ± 0.00007 , $R^2 = 0.997$; blue line slope: -0.03997 ± 0.00004 , $R^2 = 0.997$. **Left:** Bar graph representing the normalized mean slopes of the linear segments..... 54

Figure 24. A β_{1-40} aggregation in the absence and presence of copper(II) and the compounds, in HEPES buffer at 20 mmol L^{-1} , containing NaCl 150 mmol L^{-1} , pH 6.6, 37 °C and 1100 rpm after 3 hours. (A) Aggregation as measured by turbidity at 405 nm. Data are reported as mean and standard deviation. (B-I) Transmission Electron Microscopy (TEM) of the different conditions of the assay: (B) A β (C) A β + 1 eq. **X1TMP** (D) A β + 1 eq. **X1Benz** (E) A β + Cu $^{2+}$, hereafter referred to as Cu(A β) (F) Cu(A β) + 1 eq. **X1TMP** (G) Cu(A β) + 1 eq. **X1Benz** (H) Cu(A β) + 3 eq. **X1TMP** (I) Cu(A β) + 3 eq. **X1Benz**..... 57

Figure 25. Effect of the synthesized *N*-acylhydrazones on A β_{1-40} aggregation in the presence of copper(II) ions in HEPES 20 mmol L^{-1} , NaCl 150 mmol L^{-1} , pH 6.6. Thioflavin-T fluorescence curves after 3 hours incubation at 37 °C and 1100 rpm. (A) A β , A β (Cu) and A β (Cu) + 1 eq. **X1TMP** or **X1Benz**. (B) A β , A β (Cu) and A β (Cu) + 3 eq. **X1TMP** or **X1Benz**..... 58

Figure 26. NMR analysis of **X1Benz** binding to A β_{1-40} . (A) Overlaid contour plots of 1H - ^{15}N HSQC spectra of A β in the absence (black) and presence of increasing **X1Benz** concentrations: 3 eq. (blue) and 5 eq. (red). Most affected residues are labelled (for the sake of simplicity, the one letter amino acid code was employed). (B) Differences in the mean weighted chemical shift (MW 1H - ^{15}N ACS) displacements between free and **X1Benz**-bound A β at molar ratios of

1:1 (gray), 2:1 (green), 3:1 (blue) and 5:1 (red). Experiments were recorded at 15 °C (80 μmol L ⁻¹ Aβ in Tris 20 mmol L ⁻¹ pH 7.3).....	60
Figure 27. ¹ H NMR of the aromatic side chains of Aβ ₁₋₄₀ in the presence of copper(II) and X1Benz . Spectra were registered at 15 °C in Tris buffer 20 mmol L ⁻¹ pH 7.3 of samples containing (A) Aβ (80 μmol L ⁻¹) (B) Aβ + 1 eq. Cu ²⁺ (C) Aβ + 1 eq. Cu ²⁺ + 5 eq. X1Benz (D) Aβ + 1 eq. Cu ²⁺ + 5 eq. X1Benz followed by addition of 10 mmol L ⁻¹ EDTA. Spectral region with the resonances of 400 μmol L ⁻¹ X1Benz are shown in (E) along with the signals' assignment. For the sake of simplicity, the one letter amino acid code was employed.	61
Figure 28. Intra-ligand and CT absorption bands of different equimolar Aβ ₁₋₁₆ , CuCl ₂ · H ₂ O and X1Benz mixtures in 20 mmol L ⁻¹ Tris buffer (pH 7.3) at 25 °C. [] = 5 x 10 ⁻⁵ mol L ⁻¹	62
Figure 29. ¹ H NMR spectrum (400 MHz) of the X1NIC mixture in DMSO- <i>d</i> ₆ at 25 °C.	64
Figure 30. Structural proposal of the (<i>Z</i>) isomer of X1NIC with an intramolecular H-bond (highlighted in yellow) that probably stabilizes the compound and causes deshielding of the -NH signal in the ¹ H NMR spectrum.	64
Figure 31. ¹ H NMR spectrum (400 MHz) of X1NIC-(E) in DMSO- <i>d</i> ₆ at 25 °C.	65
Figure 32. ¹ H- ¹ H NOESY NMR spectrum (400 MHz) of X1NIC-(E) in DMSO- <i>d</i> ₆ at 25 °C (top). The proposed structure of the (<i>E</i>) isomer in an anti-conformation and its spatial correlations are shown on the bottom. Blue arrows indicate relevant expected dipolar couplings.	66
Figure 33. ¹ H NMR spectrum (400 MHz) of X1NIC-(Z) in DMSO- <i>d</i> ₆ at 25 °C.	67
Figure 34. ¹ H- ¹ H NOESY NMR spectrum (400 MHz) of X1NIC-(Z) in DMSO- <i>d</i> ₆ at 25 °C (top). The proposed structure of the (<i>Z</i>) isomer in an anti-conformation and its spatial correlations are shown on the bottom. Blue arrows indicate relevant expected dipolar couplings.	68
Figure 35. Mid-infrared spectra of (A) X1NIC-(E) and (B) X1NIC-(Z) . Samples were prepared as KBr pellets.	71
Figure 36. UV-Vis absorption spectra of X1NIC-(E) and its precursors (5 x 10 ⁻⁵ mol L ⁻¹) in 1% DMSO/Tris (10 mmol L ⁻¹ , pH 7.4), obtained over a period of 12 h, at room temperature.	72
Figure 37. UV-Vis absorption spectra of X1NIC-(Z) and its precursors (5 x 10 ⁻⁵ mol L ⁻¹) in 1% DMSO/Tris (10 mmol L ⁻¹ , pH 7.4), obtained over a period of 12 h, at room temperature.	73
Figure 38. Thermal stability analysis of X1NIC-(E) assessed by ¹ H NMR, with spectra taken every 10 °C, from 25 to 65 °C. A final spectrum was collected after cooling the sample back to room temperature (25 °C). Selected spectral windows: (A) 2.0 – 5.0 ppm; (B) 7.0 – 9.5 ppm; (C) 12.0 – 15.0 ppm.	74
Figure 39. Thermal stability analysis of X1NIC-(Z) assessed by ¹ H NMR, with spectra taken every 10 °C, from 25 to 65 °C. A final spectrum was collected after cooling the sample back to room temperature (25 °C). Selected spectral windows: (A) 2.0 – 5.0 ppm; (B) 7.0 – 9.5 ppm; (C) 12.0 – 15.0 ppm.	75
Figure 40. Method of continuous variations to evaluate the copper(II) binding affinity of the two isomers of X1NIC : (A) X1NIC-(E) and (B) X1NIC-(Z) . Representative electronic spectra of ligand molar fractions from 0.5 to 1.0. <i>Insets</i> : absorbance <i>versus</i> molar fraction plots. Conditions: HEPES buffer (50 mmol L ⁻¹ , pH 7.4), 25 °C.	80
Figure 41. Simultaneous X1NIC-(E)/X1NIC-(Z) –copper(II) interactions studied through ¹ H NMR (400 MHz) spectroscopy, at 25 °C. Black: Mixture of both	

X1NIC isomers at *E/Z* ratio 1:1, in DMSO-*d*₆. Red: Same mixture after addition of 0.05 eq. copper(II) resulting in a solution of DMSO-*d*₆ containing 1% D₂O. ... 82

Figure 42. Structure of the hIAPP₁₈₋₂₂ peptide fragment (HSSNN) employed in this work. Side chains are marked in blue for H (histidine), red for S (serine) and green for N (asparagine). 83

Figure 43. ¹H NMR spectra (700 MHz) of (A) pure hIAPP₁₈₋₂₂ and (B) hIAPP₁₈₋₂₂ + 0.1 eq. Cu²⁺, both acquired at 25 °C. Samples were prepared in 20 mmol L⁻¹ Tris-*d*₁₁ at pH 7.4, with 8.5% D₂O and 4% DMSO-*d*₆. Histidine residues are highlighted in blue, while red was used for serine and green for asparagine. (**) indicates the most affected signals upon copper(II) addition, while (*) is showing signals moderately modified in this context. 84

Figure 44. Proposed coordination sphere for the Cu²⁺-hIAPP₁₈₋₂₂ complex. The peptide's main chain is highlighted in bold gray, while the side chains are marked in blue for H (histidine), red for S (serine) and green for N (asparagine). 85

Figure 45. Interactions of (A) **X1NIC-(E)** and (B) **X1NIC-(Z)** with the Cu²⁺-hIAPP₁₈₋₂₂ system. For each compound, from bottom to top: ¹H NMR spectra (700 MHz) of hIAPP₁₈₋₂₂, hIAPP₁₈₋₂₂ + 0.1 eq. Cu²⁺, hIAPP₁₈₋₂₂ + 0.1 eq. Cu²⁺ + 0.1 eq. compound, hIAPP₁₈₋₂₂ + 0.1 eq. Cu²⁺ + 1.0 eq. compound, and pure compound spectrum for comparison purposes. All spectra were acquired at 25 °C. Samples were prepared in 20 mmol L⁻¹ Tris-*d*₁₁ pH 7.4, with 8.5% D₂O and 4% DMSO-*d*₆. Arrows point to relevant spectral changes: red is used for changes in serine-related signals while blue refers to histidine. Red dotted lines highlight compound signals that remained unchanged. Black dotted lines, on the other hand, were used to point out unaffected peptide signals. 88

Figure 46. Cyclic voltammetry of the binary system involving Cu²⁺ and the human IAPP coordinating fragment hIAPP₁₈₋₂₂ (HSSNN). **Top:** CVs of Cu²⁺ at 0.1 mmol L⁻¹ (black), hIAPP₁₈₋₂₂ at 0.1 mmol L⁻¹ (red) and a 1:1 molar mixture of hIAPP₁₈₋₂₂ and Cu²⁺ (blue). Conditions: 5% DMSO / buffer (50 mmol L⁻¹ HEPES pH 7.4, 100 mmol L⁻¹ NaCl) solution, at room temperature. **Bottom:** CV of Cu²⁺ (0.1 mmol L⁻¹) in the absence of DMSO (50 mmol L⁻¹ HEPES pH 7.4, containing 100 mmol L⁻¹ NaCl), at room temperature. 90

Figure 47. Cyclic voltammetry of the binary system involving Cu²⁺ and **X1NIC-(E)**. Conditions: 5% DMSO / buffer (50 mmol L⁻¹ HEPES pH 7.4, 100 mmol L⁻¹ NaCl) solution, at room temperature. [Cu²⁺] = 0.1 mmol L⁻¹. [**X1NIC-(E)**] = 0.1-0.5 mmol L⁻¹. “Free” copper (at concentration of 0.1 mmol L⁻¹) voltammogram included for the sake of comparison (gray line). 91

Figure 48. Cyclic voltammetry of the binary system involving Cu²⁺ and **X1NIC-(Z)**. Conditions: 5% DMSO / buffer (50 mmol L⁻¹ HEPES pH 7.4, 100 mmol L⁻¹ NaCl) solution, at room temperature. [Cu²⁺] = 0.1 mmol L⁻¹. [**X1NIC-(Z)**] = 0.1-0.5 mmol L⁻¹. “Free” copper (at concentration of 0.1 mmol L⁻¹) voltammogram included for the sake of comparison (gray line). 93

Figure 49. Titration of the Cu²⁺-hIAPP₁₈₋₂₂ system with increasing amounts of **X1NIC-(E)**. Conditions: 5% DMSO / buffer (50 mmol L⁻¹ HEPES pH 7.4, 100 mmol L⁻¹ NaCl) solution, at room temperature. Red: free hIAPP₁₈₋₂₂ (0.1 mmol L⁻¹). Dark gray: “free” Cu²⁺ (0.1 mmol L⁻¹). Blue: Cu²⁺-hIAPP₁₈₋₂₂ at 1:1 stoichiometry. From yellow to dark orange: additions of 0.1 eq. **X1NIC-(E)** (concentration range: 0.01-0.09 mmol L⁻¹). Pink: [**X1NIC-(E)**] = 0.1 mmol L⁻¹. Purple: [**X1NIC-(E)**] = 0.2 mmol L⁻¹. “Free” copper (at concentration of 0.1 mmol L⁻¹) voltammogram included for the sake of comparison (gray line). 94

Figure 50. Titration of the Cu^{2+} -hIAPP₁₈₋₂₂ system with increasing amounts of **X1NIC-(Z)**. Conditions: 5% DMSO / buffer (50 mmol L⁻¹ HEPES pH 7.4, 100 mmol L⁻¹ NaCl) solution, at room temperature. Red: free hIAPP₁₈₋₂₂ (0.1 mmol L⁻¹). Dark gray: “free” Cu^{2+} (0.1 mmol L⁻¹). Blue: Cu^{2+} -hIAPP₁₈₋₂₂ at 1:1 stoichiometry. From light to dark green: additions of 0.1 eq. **X1NIC-(Z)** (concentration range: 0.01-0.09 mmol L⁻¹). Pink: [**X1NIC-(Z)**] = 0.1 mmol L⁻¹. Purple: [**X1NIC-(Z)**] = 0.2 mmol L⁻¹. 95

List of Tables

Table 1. Selected infrared frequencies of the <i>N</i> -acylhydrazones X1TMP and X1Benz , along with their assignments. Samples were prepared as KBr pellets... 45	45
Table 2. ¹ H (400 MHz) signal attribution for X1TMP and X1Benz (DMSO- <i>d</i> ₆ at 25 °C)..... 47	47
Table 3. Calculated (OSIRIS Property Explorer: DataWarrior™) descriptors of pharmacological relevance for X1TMP and X1Benz . MW: molecular weight, cLog P: calculated partition coefficient, cLog S: calculated water solubility, PSA: polar surface area..... 50	50
Table 4. ¹ H (400 MHz) signal attribution for X1NIC-(E) and X1NIC-(Z) (DMSO- <i>d</i> ₆ at 25 °C). 69	69
Table 5. Selected infrared frequencies of the <i>N</i> -acylhydrazones X1NIC-(E) and X1NIC-(Z) , along with their assignments. Samples were prepared as KBr pellets. 70	70
Table 6. Calculated (OSIRIS Property Explorer: DataWarrior™) descriptors of pharmacological relevance for X1NIC . MW: molecular weight, cLog P: calculated partition coefficient, cLog S: calculated water solubility, PSA: polar surface area. 76	76

" A scientist is not a person who gives the right answers;
they are one who asks the right questions." (Claude Lévi-Strauss)

1. Introduction

1.1. Protein aggregation

Proteins are composed of amino acids that are linked together through peptide bonds and are responsible for numerous essential functions in the organism. In a physiological environment, they participate in the construction of cellular architecture, in defense and signaling systems, in the transport of molecules, among other functions (Contessoto *et al.*, 2018).

Under pathological conditions, the native structure of proteins may undergo alterations such as aberrant folding, which has been associated with the development of diseases often referred to as aggregopathies (Hartl, 2017). Protein misfolding leads to the formation of different types of aggregates that, in turn, may induce cellular death and, consequently, organ malfunction. Examples of such pathologies are Alzheimer's (AD) and Parkinson's diseases, as well as type 2 diabetes *mellitus* (T2DM), certain forms of heart disease and cancer, among others (Almeida *et al.*, 2010).

Changes in the native conformation of a protein can occur from different factors, which impair its stability. The loss of the conformational stability of a protein results in partial unfolding and transformation of the α -helix structure into a β -sheet, due to hydrophobic interactions and hydrogen bonds between amino acids (Kopito, 2000).

The resulting structures can usually be characterized as amyloid or non-amyloid aggregates. The first exhibits a structure organized into parallel or anti-parallel β -sheet-rich fibers and can be distinguished from other types of aggregates based on colorimetric tests using Congo red dye, in which amyloid aggregates show a green birefringence under polarized light (Chiti & Dobson, 2017; Yakupova *et al.*, 2019). The term "amyloid" was first used by the botanist Matthias Schleiden, who described plant starch. This nomenclature was later used to describe abnormal macroscopic deposits in the mid-19th century by Rudolf Virchow, who used a combination of iodine and sulfuric acid to stain these aggregates in the diseased organs of his patients. Virchow discovered that, like

starch, the tissues of the organs he analyzed showed a blue color, and were therefore called amyloid (Makowski, 2009).

According to the guidelines of the International Society of Amyloidosis (ISA), it was established that the term amyloid is used to define, in general, any fibrillar structure formed by β -sheets. In addition, the ISA introduced the new expression “functional amyloid” to better specify the use of the term (Buxbaum *et al.*, 2022).

The formation of aggregates (Figure 1) is a type of polymerization reaction, which starts from a nucleation phase, followed by a growth step (Falcão, 2015), in which the formed nucleus associates with monomers until the formation of soluble and toxic oligomeric species (Chiti & Dobson, 2006). Finally, there is the formation of mature, insoluble fibers after all the monomeric protein in the medium is consumed (Zapadka *et al.*, 2017). It is currently well accepted that the oligomeric species that are formed at the beginning of the aggregation process cause more severe cellular deterioration when compared to insoluble fibers and aggregates (Huang & Liu, 2020; Lee *et al.*, 2016; Wang *et al.*, 2019).

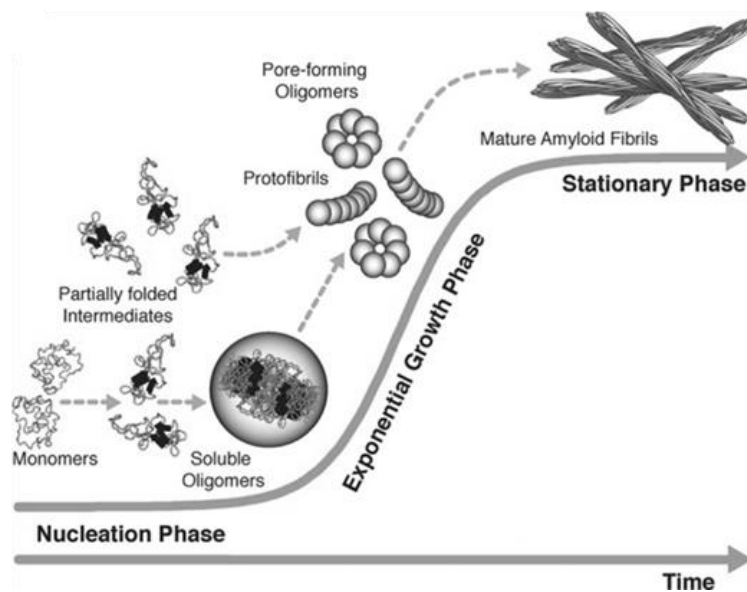


Figure 1. Protein aggregation mechanism. (A) Native structure. (B) Beginning of β -sheet formation. (C) Formation of nucleus. (D) Formation of oligomers. (E) Formation of mature fibers. Adapted from (Theillet *et al.*, 2014).

The protein aggregation mechanism may result from chemical or physical alterations, in a process highly dependent on certain conditions, such as protein

concentration, pH, temperature, and also the presence of metal ions (Chiti & Dobson, 2006; Mahler *et al.*, 2009; Wang *et al.*, 2010).

Depending on the protein involved and the region of the body affected, there are different symptomatic manifestations and respective progressions associated with each disease (Hull *et al.*, 2004; Vilar *et al.*, 2008).

1.2. Alzheimer's disease (AD)

Alzheimer's disease (AD) is a neurodegenerative condition most often related to advanced age, which represents the major cause of dementia in the world. It is considered an aggregopathy since it is characterized by the misfolding of the β -amyloid peptide ($A\beta$), which leads to the formation of soluble and toxic oligomers that disrupt synaptic function, leading to neuronal death (Lee *et al.*, 2017; Wang *et al.*, 2020).

Recent studies have shown that approximately 50 million people suffer from AD worldwide (Xiong *et al.*, 2021), and the World Health Organization estimates that the number of cases is expected to triple within 30 years (Mitchell *et al.*, 2020). In the United States alone, about 6.7 million elderly Americans are currently living with AD, and the number of cases is projected to double by 2060, as reported by Alzheimer's Association, 2023.

In Brazil, epidemiological data on AD were collected from 2013 to 2022 and, as a result, it was observed that the highest incidence of cases is in the Southeast region of the country, which may be related to the greater population number in this region. As shown in Figure 2, the SUS (Unified Health System, from Portuguese *Sistema Único de Saúde*) reported that the Southeastern region of Brazil had more than 7 thousand hospitalizations due to AD during the studied period, which is much more than other regions of the country (Araújo *et al.*, 2023).

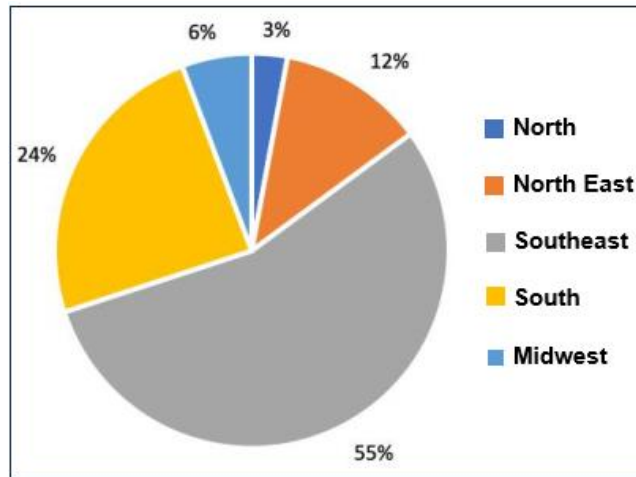


Figure 2. Hospitalizations due to AD in each region of Brazil in the period between 2013 and 2022.

Adapted from (Araújo *et al.*, 2023).

Alzheimer's disease was described for the first time by the German physician and neuropathologist Alois Alzheimer who, in 1901, received Auguste Deter, aged 50, at the hospital where he worked in Frankfurt, presented symptoms such as memory loss, confusion, paranoia and disorientation (Stelzmann *et al.*, 1995). In 1906, Auguste died and, during the autopsy, Alzheimer observed the presence of two types of lesions in the brain, currently known as senile or neuritic plaques and neurofibrillary tangles. Studies performed by the physician demonstrated that such lesions were related to the deposition of proteins that are found in the brain (Maurer *et al.*, 1997). Neuritic plaques are formed by the accumulation of $A\beta$, which is deposited in the extracellular environment of neuronal tissues. In contrast, neurofibrillary tangles result from the intracellular deposition of hyperphosphorylated tau protein (Selkoe & Hardy, 2016).

The $A\beta$ peptide is a fragment derived from the proteolysis of the amyloid precursor protein (APP). APP can be cleaved *via* 3 secretases: the action of the α -secretase enzyme produces a non-amyloidogenic peptide that has neuroprotective activity. However, through γ and β -secretases, there is the production of $A\beta$, which is an amyloidogenic peptide (Figure 3) (Cavalcanti & Engelhardt, 2012). The breakage, at different positions, of APP by the γ and β -secretase enzymes give rise to fragments of different sizes, with 40 and 42 amino acid residues, respectively, also referred to as $A\beta_{1-40}$ and $A\beta_{1-42}$. The first is the most abundant and soluble, while the latter presents greater neurotoxic potential and is more

susceptible to aggregation, being found in high concentration in senile plaques (Chang & Chen, 2014; Chiang *et al.*, 2008; Soreghan *et al.*, 1994; Zhang *et al.*, 2002).

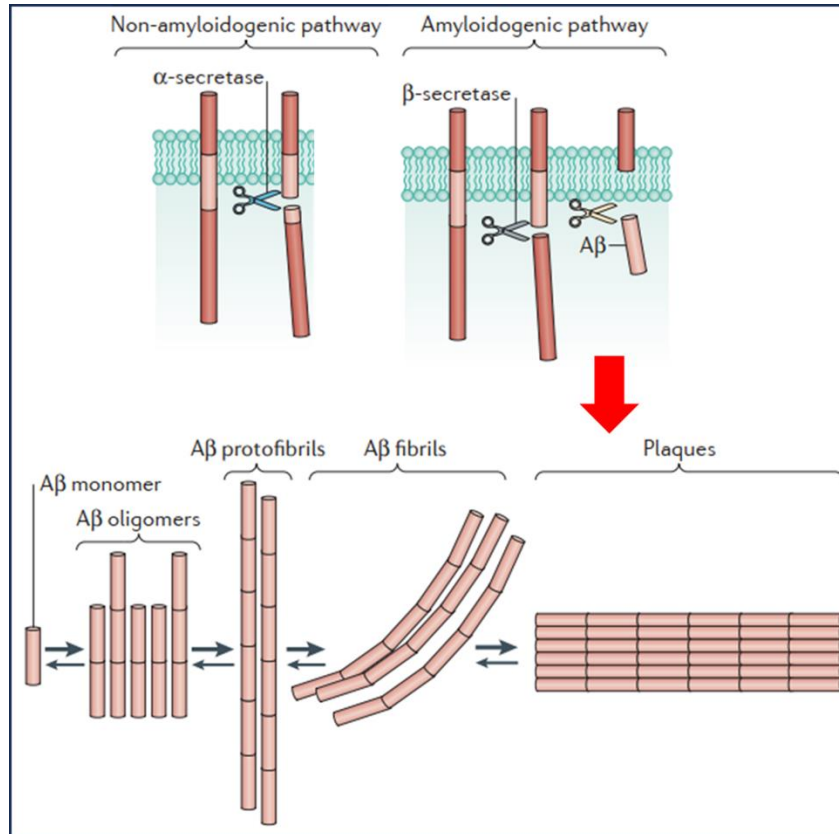


Figure 3. Scheme of APP cleavage through non-amyloidogenic and amyloidogenic pathways. Adapted from (Heppner *et al.*, 2015).

For a long time, the mature fibers were considered the root cause of the pathogenesis of Alzheimer’s disease. These aggregates, that form the senile plaques, were considered responsible for blocking the reception of nervous stimuli to cholinergic neurons, associated with the construction of memories and cognition (Lacor *et al.*, 2004). However, more recent studies point to the oligomeric hypothesis, in which the soluble oligomeric intermediates generated during protein aggregation are more toxic (Ochiishi *et al.*, 2019; Vadukul *et al.*, 2020). Currently, it is well-accepted that Aβ oligomers can seriously damage neuronal synapses (Gulisano *et al.*, 2018; Li *et al.*, 2018; Marcatti *et al.*, 2022; Verma *et al.*, 2015).

On the other hand, the tau protein has the function of facilitating the polymerization of tubulin in the cell, for the maintenance of neuronal microtubules' structure (Figure 4A). Microtubules are formed by tubulin units and the tau protein acts as the “glue” that provides stability (Cavalcanti & Engelhardt, 2012). In AD patients, tau protein accumulates in a non-physiological, twisted and hyperphosphorylated form, and this implies a loss of stability and impairs its ability to bind to microtubules (Figure 4B). Consequently, the disintegration of the neuronal cytoskeleton occurs, as well as the formation of neurofibrillary tangles, formed intracellularly by tau protein aggregates, in the region of the temporal lobe and hippocampus (Figure 5). This leads to the loss of the ability of neurons to transmit electrical signals and also to transport nutrients, leading to irreversible neurodegeneration (Morales *et al.*, 2010).

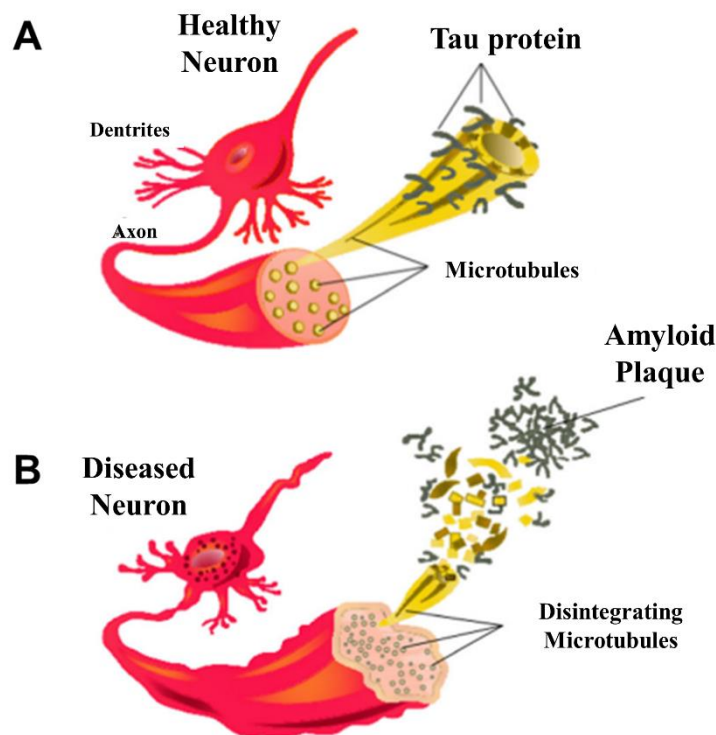


Figure 4. (A) Healthy neuron representation. (B) Neuron affected by AD. Adapted from (Alirezaei *et al.*, 2020).

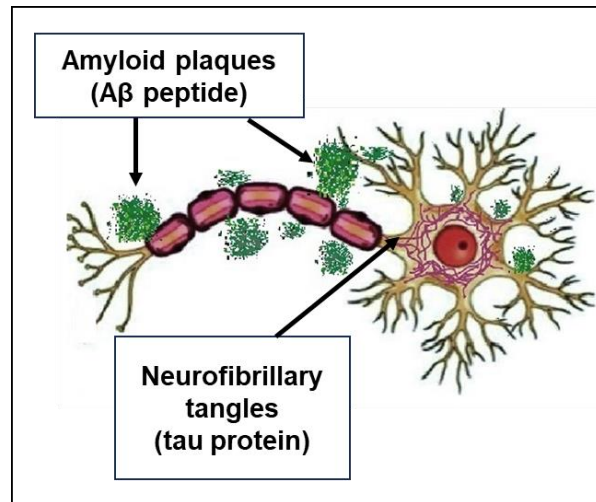


Figure 5. Scheme of the protein deposits in neurons affected by Alzheimer’s disease: extracellular A β peptide and intracellular tau protein.
Adapted from (De Falco *et al.*, 2016).

An etiological hypothesis regarding the pathogenesis of AD considers this disease as a neuroendocrine condition, presenting a link with diabetes, and therefore receiving the terminology “type 3 diabetes” (De La Monte & Wands, 2008; Steen *et al.*, 2005). More recently, in the literature, AD has been correlated with insulin resistance and its dysregulation at the neuronal level (Kellar & Craft, 2020), which have been described as anomalies that precede or occur together with the prodromal phase of the disease, in which there are the first signs of cognition impairment. This is due to the fact that the hormone insulin binds to specific receptors in the brain that are associated with cognition (De La Monte & Wands, 2008; Steen *et al.*, 2005). This hypothesis gained strength from epidemiological studies that correlated diabetes with AD, and that damage to insulin signaling in the brain would be the main reason, in which the deficiency in the response of this hormone to its receptors in the brain causes neurotoxic problems (Nguyen *et al.*, 2020).

Insulin in the brain has an important function, which is to activate the extracellular secretion of the A β peptide. However, it is also responsible for preventing its accumulation intracellularly, through the activation of the insulin-degrading enzyme (IDE) (Gasparini *et al.*, 2001; Nguyen *et al.*, 2020). A failure in this process increases the neurotoxic effects of A β on neurons, ultimately leading to memory and learning deficits, which are linked with AD (Freude *et al.*, 2009; Gasparini *et al.*, 2001; Nguyen *et al.*, 2020).

As evidence, De Felice *et al.* (2022) report assays carried out on mice using intracerebroventricular injection of insulin, which showed an improvement in the animals' memory through a passive avoidance task, which is based on the association formed between a specific environmental context in which the animal learns to avoid doing something through nerve impulses such as small shock (Chang & Chen, 2014; Park *et al.*, 2000).

1.3. Type 2 diabetes mellitus (T2DM)

Another disease that affects a great number of people is type 2 diabetes mellitus (T2DM), which is characterized by hyperglycemia (increased blood glucose), and may result from defects in the secretion or action of the hormone insulin, produced by β -cells of the pancreatic islets (Del Prato *et al.*, 2017; Tripathy & Chavez, 2010). T2DM is strongly associated with a sedentary lifestyle and obesity. This can lead to the body's inability to respond to insulin stimulation, generating resistance to this hormone, which is one of the main characteristics of this pathology (Lyssenko *et al.*, 2008; Schwartz & Porte, 2005; Tuomi *et al.*, 2014).

The International Diabetes Federation (IDF) published, in its 10th edition magazine (IDF Diabetes Atlas 10th Edition, 2021), a study in which they reveal the number of people, between the ages of 20 and 79, affected by diabetes (types 1 and 2), along with a forecast until the year 2045. The IDF used 2021 population data from the United Nations Population Division to estimate the number of people with diabetes in a global panorama, as well as separated in continental regions. As shown in Figure 6, it is possible to conclude that developing countries, that usually present bad healthcare systems, are expected to present a much higher increase in the number of DM cases. It is worth noting that 90% of the cases in the study are related to T2DM.

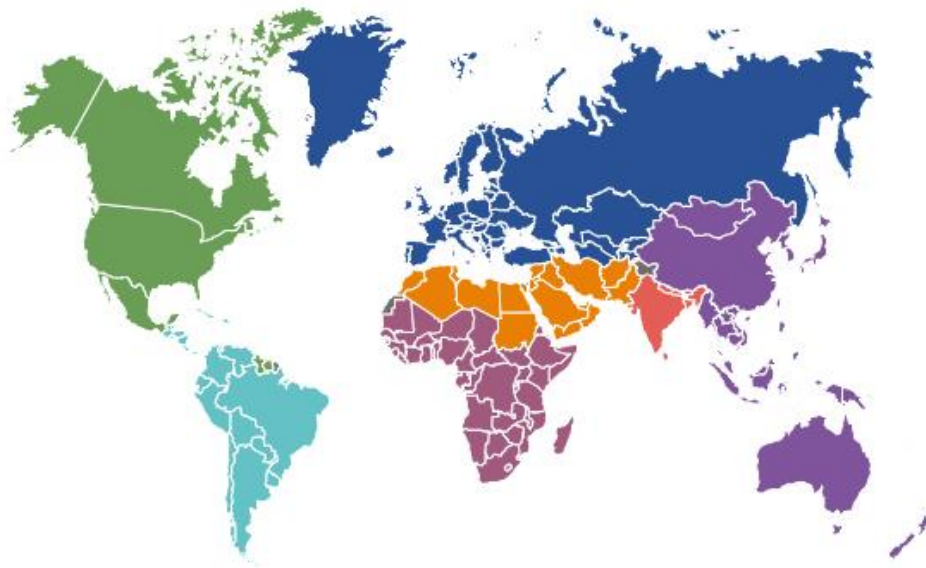


Figure 6. Diabetes cases globally and divided by continents in 2021, and predictions until 2045, considering individuals in the range of 20 to 79 years old. (IDF Diabetes Atlas 10th Edition, 2021).

Interestingly, T2DM can also be considered an aggregopathy, as it is also characterized by the presence of aggregated pancreatic islet amyloid polypeptide (IAPP), responsible for both the regulation of food intake and the transmission of signals to the central nervous system (CNS) (Patel & Jhamandas, 2012). IAPP, also known as amylin, was first observed by Eugene Opie in 1901, and was described as hyaline deposits found in the pancreatic islets of *postmortem* T2DM

patients (Opie, 1901). Only in 1986 was IAPP structurally characterized as an amyloidogenic peptide associated with this disease (Paulsson *et al.*, 2006; Westermark *et al.*, 1986).

This peptide is derived from the PreProIAPP precursor, consisting of 89 amino acid residues, in which the signal sequence (22 amino acid residues) is hydrolyzed in the endoplasmic reticulum, originating ProIAPP, which has 67 amino acid residues. ProIAPP then undergoes enzymatic cleavage, resulting in the mature peptide IAPP, with 37 amino acid residues (Figure 7), which is secreted by the β -cells of the pancreatic islets (Meng *et al.*, 2007; Raimundo *et al.*, 2020). IAPP is prone to structural misfolding, forming plaques that are deposited in the extracellular space of islets. The aggregation process, which is similar to that of the AD-related A β peptide, also generates toxic and soluble oligomeric species (Pilkington *et al.*, 2016; Rowles *et al.*, 2020).

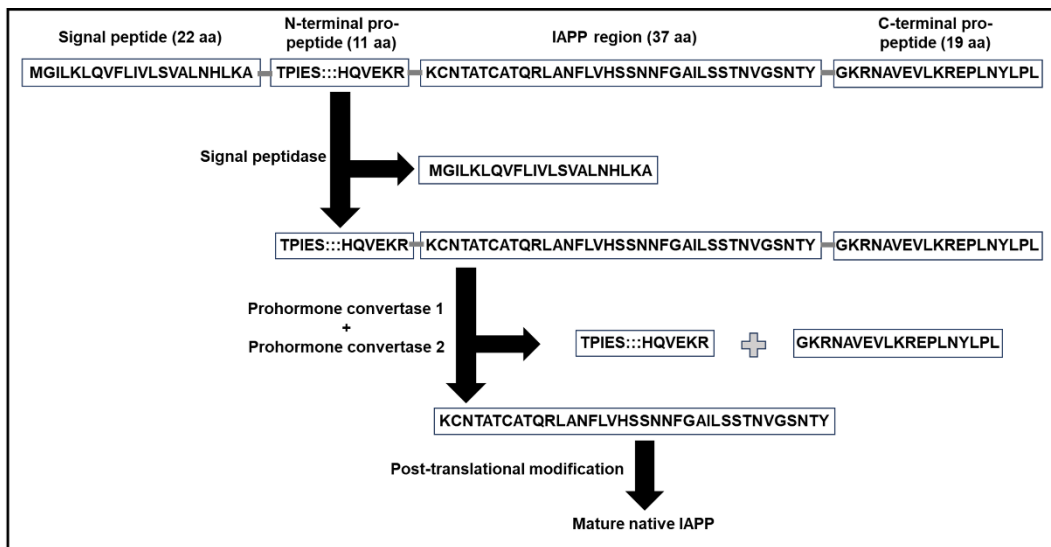


Figure 7. Processing of PreProIAPP to form the mature human IAPP. Adapted from (Ahmad *et al.*, 2011).

The IAPP family of peptides presents some differences in the sequencing of amino acid residues (Figure 8), which can be correlated with the peptide's ability to form amyloid aggregates or not. These differences are mainly located in the region of residues 20 to 29 (Ahmad *et al.*, 2011; Asthana *et al.*, 2018).

Unlike in mammals, this peptide in rodents (rIAPP) is not amyloidogenic due to the presence of the amino acid proline in positions 25, 28 and 29, which is responsible for breaking the pattern of β -sheet formation (Ahmad *et al.*, 2011;

Westermarck *et al.*, 2011). Based on this knowledge, a peptide called Pramlintide was synthesized and showed the ability to maintain the hormonal activity of hIAPP in combination with the low propensity to form amyloidogenic fibers (Ryan *et al.*, 2008). In 2004, the American Food and Drug Administration (FDA) approved Pramlintide for use in diabetic patients (Ryan *et al.*, 2008) as a treatment in conjunction with the use of insulin, aiming the decrease postprandial glucagon secretion, delaying gastric emptying and inducing satiety (Kommera *et al.*, 2024). Pramlintide was well accepted clinically, as it can replace IAPP, since the latter is an insoluble hormone prone to aggregation, different from its soluble and non-aggregating analog (Alrefai *et al.*, 2010).

	1	18	28	37
Human	KCNTATCATQRLANFLVHSSNNFGAILSSTNVGSNTY(C=O)NH ₂			
Rat	KCNTATCATQRLANFLCRSSNNLGPVLPPTNVGSNTY(C=O)NH ₂			
Pramlintide	KCNTATCATQRLANFLVHSSNNFGPILPPTNVGSNTY(C=O)NH ₂			

Figure 8. Comparison between the peptides hIAPP, rIAPP and Pramlintide. Blue: region with high affinity for copper(II) ions (18-22); Gray: amyloidogenic region (22-28); Red: substituted amino acid residues in IAPP analogues.
Adapted from (Alghrably *et al.*, 2019).

Besides protein aggregation, widespread oxidative stress caused by cellular redox imbalance is another feature common to T2DM and AD, in addition to impaired insulin signaling in the CNS, which is associated with memory formation and learning (Patel & Jhamandas, 2012). Recently, studies have shown that IAPP can cross the blood-brain barrier (BBB) and deposit together with A β plaques in the brain, thus forming more complex aggregates that can lead to increased neuronal death when compared to the non-associated peptides (Rowles *et al.*, 2020).

1.4. Relationship between aggregopathies and metals

Metal ions play a vital role in the correct functioning of the human body, in which they perform several roles. An example is iron, which forms a complex called oxyhemoglobin when O₂ molecules bind to it in hemoglobin, thus making it possible to transport oxygen in the blood (Radović-Janošević *et al.*, 2020; Yiannikourides & Latunde-Dada, 2019). Copper plays, among other, an important role in glucose metabolism and its deficiency can lead to growth disorders in children for example (Avram *et al.*, 2021), while zinc proves to be important in cell transport, protein and collagen synthesis, aiding in the cicatrization of skin wounds, and is also an important neurotransmitter (Chasapis *et al.*, 2020). Furthermore, these and other metals constitute the active site of several metalloenzymes.

High levels of copper not only increase oxidative stress in T2DM, but it can also lead to β -cell death, in addition to upholding insulin resistance and hyperglycemia (Park *et al.*, 2009). As a consequence, it promotes the glycosylation of proteins, with the formation of free radicals, which contribute to greater complications related to the disease (Eaton & Qian, 2002). It is worth mentioning that copper has a high affinity for these glycosylated substances. A study developed by Hasanato (2020), which assessed the metal levels, such as copper, in the blood of diabetic patients, concluded that there was dyshomeostasis of these metals with variation in glycemic control.

Iron, zinc, and copper also play important roles in the brain, including neurotransmitter synthesis and neuronal transmission. The deficit of these metals can generate disorders related to learning and memory (Kawahara *et al.*, 2020). These metals are considered essential to the functioning of the body, so deficiency or excess can lead to harmful effects on health. Therefore, it is fundamental to maintain their homeostasis, that is, the concentration and distribution of these metals must be well-regulated in the body (Wood *et al.*, 2012).

Work carried out in recent years has progressively evidenced the collaborative role of dyshomeostasis of endogenous metals, such as zinc, copper and iron, in neurodegenerative diseases (Hane & Leonenko, 2014; Kabir *et al.*, 2021; Karpenko *et al.*, 2018; Lopes de Andrade *et al.*, 2021; Metaxas, 2021). Due to the rich redox chemistry of these last two biometals, their deregulation leads to

oxidative stress in the brain, as a consequence of the production of reactive oxygen species (ROS) and reactive nitrogen species (RNS).

In Alzheimer's disease, the A β peptide and its fragments are of particular interest because they bind to biometals with high affinity, especially in the *N*-terminal region. It has been shown that metal homeostasis is disturbed in the brains of AD patients (Wang *et al.*, 2020). Metal ion binding leads to conformational changes in the peptide (Rana & Sharma, 2019). Specifically, A β -Cu interactions lead to the formation of toxic oligomeric species (Sharma *et al.*, 2013; Smith *et al.*, 2006), besides the catalytic production of ROS (Parthasarathy *et al.*, 2014), which are responsible for the widespread oxidative damage observed in this pathology. In the specific case of copper(II), a distorted square-planar geometry is observed, involving, at lower pH values (Figure 9A), the amine of Asp1, the carbonyl from Asp1-Ala2 amide bond and imidazole nitrogen atoms from two histidine residues, His6 and His13 or His14 (Dorlet *et al.*, 2009; Kowalik-Jankowska *et al.*, 2003). At a more basic medium (Figure 9B), the nitrogen from Asp1-Ala2 amide bond is deprotonated, and binds copper, along with the terminal Asp1 amine, the carbonyl from the Ala2-Glu3 peptide bond and an imidazole nitrogen from one of the His residues (Syme *et al.*, 2004). Unlike the human A β peptide, the rodent peptide is not amyloidogenic, resulting in no A β deposition in the brain of these animals. This is probably due to substitutions of certain amino acid residues (Arg5, Tyr10 and His13) as shown in Figure 10 (Kowalik-Jankowska *et al.*, 2003), which may also affect its binding properties towards copper(II).

serum copper levels in diabetic patients constitute another indication of the role of metal dyshomeostasis in T2DM (Naka *et al.*, 2013).

The slightly acidic environment (pH 5.5-6) inside the β -cells prevents the formation of aggregates within the pancreas, that is, before the secretion of the peptide into the extracellular environment, which is at a physiological pH, a medium in which hIAPP is prone to aggregation (Tomasello *et al.*, 2015). Rivillas-Acevedo and collaborators used different spectroscopic techniques and hIAPP fragments to elucidate the structural basis of the interaction between Cu^{2+} and this peptide (Rivillas-Acevedo *et al.*, 2015). Their studies showed that this metal ion binds to the imidazole nitrogen of the His18 residue and to the amide groups of subsequent amino acids, thus forming a N_3O -type complex at physiological pH. Later, it was demonstrated that the O-binding may be to the hydroxyl or the carbonyl oxygen (Figure 11), both through the Ser20 residue (Sánchez-López *et al.*, 2016).

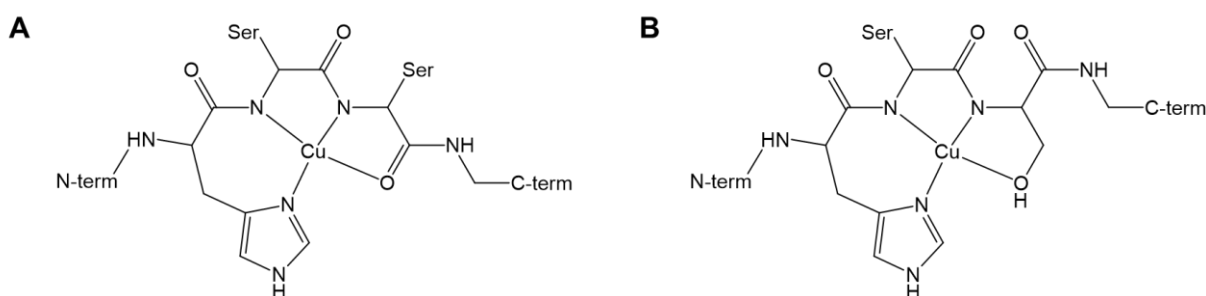


Figure 11. N_3O coordination patterns of Cu^{2+} -hIAPP complex binding to the carbonyl oxygen (**left**) and to a hydroxyl group (**right**). Adapted from (Rivillas-Acevedo *et al.*, 2015).

Sánchez-López *et al.* used several models of the Cu^{2+} -hIAPP₁₈₋₂₂ complex to better understand the metal-hIAPP interaction through theoretical calculations (Sánchez-López *et al.*, 2016). Their studies showed that the binding of Cu^{2+} with the hydroxyl group of Ser20 is more favorable due to its stronger character. This was also demonstrated by its shorter distance of 2.12 Å, compared to the binding to the carbonyl group which is 2.40 Å and constitutes a weaker and more distorted connection.

Due to the relationship between these diseases and metal-enhanced protein aggregation, the use of a therapy based on the mechanism of specific and selective metal sequestration has been proposed (Scott & Orvig, 2009). However, since

these metals play an intrinsic physiological role in human health, this approach is directed to their redistribution and not to their elimination from the organism, that is, to the restoration and maintenance of their homeostasis.

1.5. Metallophores

To avoid the accumulation of metal-enhanced toxic oligomeric species, a new therapeutic strategy has been proposed, that aims to properly redistribute the metal ions essential to the functioning of the body. The class of compounds usually called Metal-Protein Attenuating Compounds (MPACs), or metallophores, have been proposed to potentially delay or even prevent the progression of neurodegenerative diseases. The proposition is based on their activity as chelators with moderate affinity and selectivity for certain metal ions (Scott & Orvig, 2009). In other words, these compounds can compete with the protein or peptide for the binding of the metal ion, thus lessening the oligomerization process, restoring metal homeostasis, and reducing oxidative stress (Cukierman & Rey, 2022).

An example of the use of chelators as a therapeutic strategy was the case of clioquinol, a compound that was initially considered a promising drug candidate for AD. This compound has the ability to coordinate copper and zinc, in addition to being able to cross the blood-brain barrier. Clioquinol has been shown to decrease the amount of A β peptide deposits in clinical trials and would have the advantage of its possible oral administration (Adlard *et al.*, 2008; Bareggi & Cornelli, 2012). However, after certain serious side effects were observed still in the clinical phase, the development of this compound was finally suspended (Budimir, 2011). Therefore, a new generation derivative, PBT2 {5,7-dichloro-2-[(dimethylamino)methyl]quinolin-8-ol}, with a better toxicological profile, in addition to greater penetration of the blood-brain barrier was proposed (Adlard *et al.*, 2008). Regardless of having shown promising preliminary clinical results, its development as a drug for AD was also suspended, as the company communicated that PBT2 had not achieved its purpose of considerably reducing amyloid plaques in the brains of patients affected by the disease (Lannfelt *et al.*, 2008; Villemagne *et al.*, 2017).

The structures of the aforementioned compounds, clioquinol and PBT2, are shown in Figure 12 below.

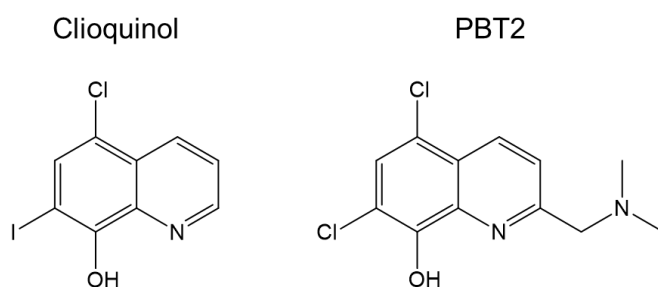


Figure 12. Structures of clioquinol (5-chloro-7-iodo-quinolin-8-ol) and PBT2 {5,7-dichloro-2-[(dimethylamino)methyl]quinolin-8-ol}.

It is important to note that both clioquinol and PBT2 are strong chelators, designed to eliminate metal ions instead of aiming at their redistribution. Moreover, the clinical trials focused on the clearance of amyloid plaques rather than on the toxic oligomeric species. These factors could be, among others, behind the observed failures.

In this sense, and given the importance of developing metallophores as moderate chelating agents for the potential treatment of diseases related to the formation of protein aggregates, our research group has been, since 2012, studying, developing and testing a versatile class of compounds that have shown promising *in vitro*, *in cell* and *in vivo* activity within the scope of these aggregopathies: the *N*-acylhydrazones (Cukierman *et al.*, 2017, 2018, 2019, 2020, 2022; De Falco *et al.*, 2020; Hauser-Davis *et al.*, 2015; Pedrozo-Peñafiel *et al.*, 2020).

The first compound described by our group in the context of AD was the hybrid 8-hydroxyquinoline/hydrazone named INHHQ (8-hydroxyquinoline-2-carboxaldehyde isonicotinoil hydrazone) (De Freitas *et al.*, 2013), which has the ability to compete *in vitro* with the A β peptide for binding copper(II) and zinc(II) (Hauser-Davis *et al.*, 2015). The same capacity was proven for the α -synuclein protein, with the compound competing for copper(I) and copper(II), in the context of Parkinson's disease. INHHQ was detected in the brain of Wistar rats after intraperitoneal injection and is non-toxic for these animals at high concentrations. Moreover, the ligand does not act as an unspecific chelator in healthy rats

(Cukierman *et al.*, 2017). It was also demonstrated that this compound is able to prevent A β oligomer-induced memory deficit in Swiss mice, as well as to decrease *in vitro* copper-mediated ROS production (De Falco *et al.*, 2020). For all these reasons, the synthesis and application of INHHQ in the context of neurodegenerative diseases was the subject of patent applications in Brazil and Europe and is already patented in the United States (US 10.189.811 B2 and US 10.316.019 B2).

Although INHHQ has, in its structure, the 8-hydroxyquinoline group in common with clioquinol and PBT2, it has been demonstrated that the ligand coordinates metal ions through the *N*-acylhydrazonic moiety (Cukierman *et al.*, 2018). This observation led to the prospect of expanding the research and developing new and even improved metallophores. Since the aqueous solubility of INHHQ was not ideal, a new generation of *N*-acylhydrazones containing the 1-methylimidazole moiety was described by our research group, showing a better pharmacological profile than the parent ligand (Cukierman, 2021). From this new family, X1INH, which has in common with INHHQ the isoniazid-derived portion of the structure, demonstrated the ability to modulate protein aggregation in a cellular model of synucleinopathy, with implications to Parkinson's disease (Cukierman *et al.*, 2020). Other imidazolic analogues, containing the 2-furan and the 2-thiophene rings, were evaluated regarding their propensity to prevent the Cu-catalyzed oxidation of a prion protein fragment, which is relevant in the context of transmissible spongiform encephalopathies (Cukierman *et al.*, 2022).

Figure 13 shows the structure of the parent *N*-acylhydrazone INHHQ, along with those of the members of the 1-methylimidazole family mentioned above, X1INH, X1Fur and X1Thio.

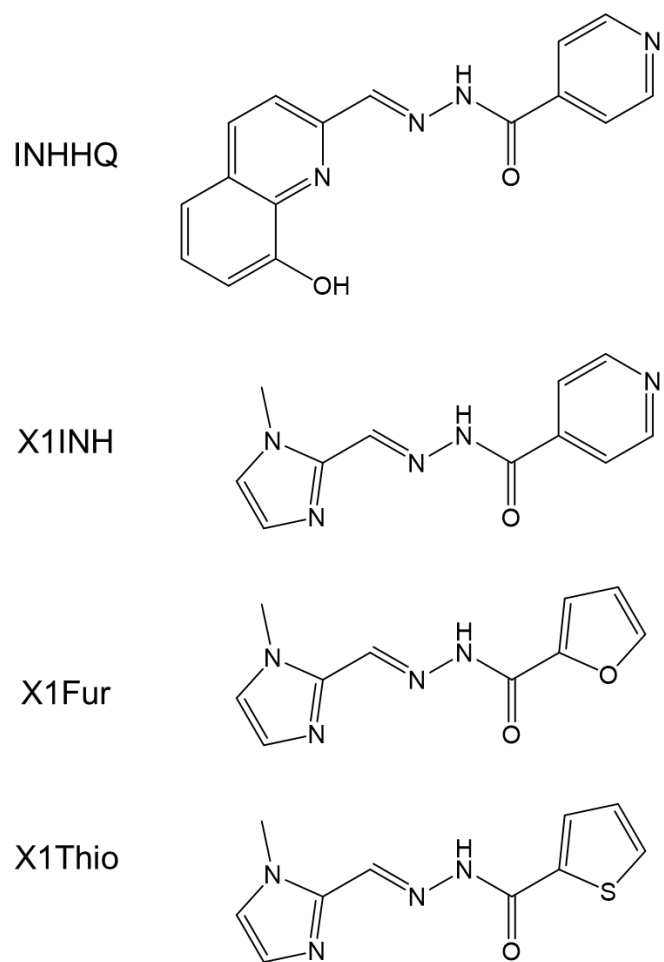


Figure 13. Structures of INHHQ (8-hydroxyquinoline-2-carboxaldehyde isonicotinoyl hydrazone), X1INH (1-methyl-1H-imidazole-2-carboxaldehyde isonicotinoyl hydrazone), X1Fur (1-methyl-1H-imidazole-2-carboxaldehyde 2-furoyl hydrazone) and X1Thio (1-methyl-1H-imidazole-2-carboxaldehyde 2-thiophenyl hydrazone).

2. Work Proposal

Currently, 16 million people live with diabetes *mellitus* in Brazil, being 90% of these diagnoses are related to T2DM (Almeida-Pititto *et al.*, 2022), while around 1.2 million people suffer from Alzheimer's disease in the country (Júnior *et al.*, 2024; Silva *et al.*, 2023). Both pathologies constitute public health problems, especially for years to come, due to the progressive increase in life expectancy of the Brazilian and world population. Despite this, the medications currently available are not effective (Matthews *et al.*, 2019; Yiannopoulou & Papageorgiou, 2020). Although treatments are prescribed, there is currently no disease-modifying therapy for such conditions.

For the people affected by T2DM to achieve an ideal long-term metabolic control, they must combine lifestyle changes, such as healthy eating and physical activity, with the use of pharmacological treatment (Schnurr *et al.*, 2020). The therapeutical approach focuses on the maintenance of glycemic control, for example by the use of metformin, which has an anti-hyperglycemic effect (Lv & Guo, 2020) and can be administered in combination with sulfonylureas as an oral medication that acts stimulating β -cells to assist in the endogenous release of insulin in the body (Marín-Peñalver *et al.*, 2016).

With respect to Alzheimer's disease, some small molecule-based drugs, such as donepezil, galantamine and rivastigmine, help control cognitive and behavioral symptoms in cases considered mild to moderate, while memantine is prescribed for moderate to severe cases, and is recommended for use in the most advanced stages of the disease (Barthold *et al.*, 2020). These treatments, in spite of not reversing or stopping the progression of the disease, can alleviate symptoms and thus contribute to a better quality of life for the patients.

In this context, this work represents an effort to explore new treatment perspectives for these pathologies, through the development of efficient metallophores that can modulate the deleterious copper-related effects in models of Alzheimer's disease and type 2 diabetes *mellitus*, and which are also active in reducing the oxidative stress to which patients with these diseases are subjected.

Thus, the present work comprises the synthesis, characterization and evaluation of the metallophoric potential of two new hydrazones derived from 1-methyl-1H-imidazole-2-carboxaldehyde, which will compose the new generation

of the 1-methylimidazolic *N*-acylhydrazone family. The aim is to explore the activity of these new compounds in different biophysical models of neuroendocrine and endocrine copper-enhanced aggregopathies.

AD and T2DM can both be considered aggregopathies, that is, both present amyloidogenic aggregation of certain peptides. The oligomerization of these peptides can be catalyzed by their interactions with physiological metal ions such as copper(II) that, in addition to accelerating the formation of oligomers, increases their toxicity and the production of ROS (Quintanar & Lim, 2019; Rana & Sharma, 2019; Yu *et al.*, 2010).

As *in vitro* models for the pathologies, we decided to employ not only the peptide itself (such as the A β ₁₋₄₀ peptide in the case of AD), but also the peptide fragments related to the main coordinating portion of the complete protein: A β ₁₋₁₆ for AD and IAPP₁₈₋₂₂ for T2DM.

The new hydrazones have been proposed based on the structure of molecules that have known receptors in the human body, with the aim of obtaining compounds with greater biocompatibility and, consequently, a better pharmacological profile. The trimethoxy-containing derivative, **X1TMP**, is structurally similar to mescaline, a natural hallucinogenic protoalkaloid, which occurs in some species of cacti, particularly the one known by the name peyote (*Lophophora williamsii*) (Cassels & Sáez-Briones, 2018). This compound, 3,4,5-trimethoxyphenethylamine, selectively binds and activates brain serotonin receptor 5-HT_{2A} with high affinity (Stork *et al.*, 2014), acting as a partial agonist. **X1NIC**, on the other hand, is derived from the nicotinic acid hydrazide, based on the structure of nicotine. Nicotinic receptors are present, in addition to the brain, also in β -cells (Yoshikawa *et al.*, 2005), which is the reason why this compound was directed to the study of T2DM. Moreover, **X1NIC** is an isomer of the most promising compound from the original series of 1-methylimidazolic hydrazones from our research group, X1INH, which makes it an even more interesting compound to study and develop.

Figure 14 shows the structures of the two proposed new compounds, compared with those of their original inspirations.

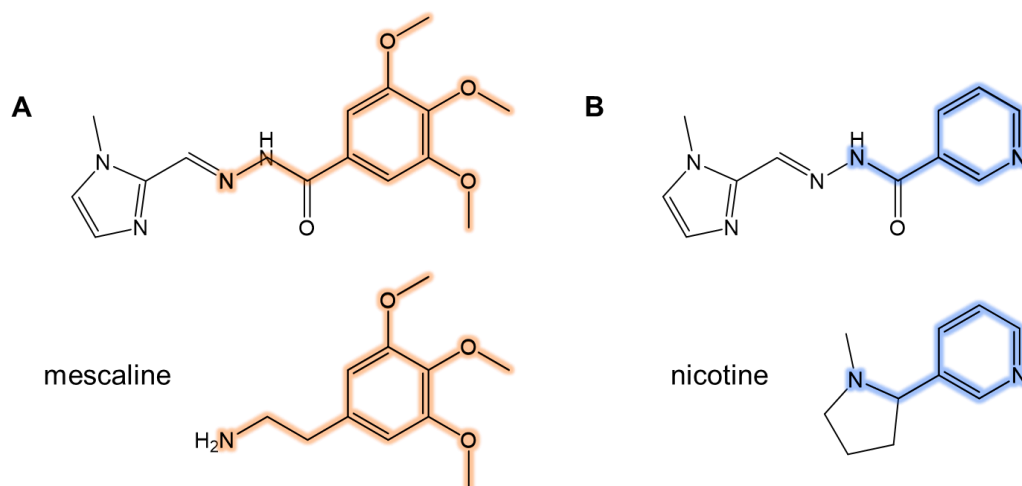


Figure 14. Structures of the new *N*-acylhydrazones considered in this work. (A) **X1TMP**: 1-methyl-1H-imidazole-2-carboxaldehyde 3,4,5-trimethoxy-benzoyl hydrazone. Comparison with mescaline is highlighted in orange. (B) **X1NIC**: 1-methyl-1H-imidazole-2-carboxaldehyde nicotinoyl hydrazone. Comparison with nicotine is highlighted in blue.

These compounds can be easily synthesized through a Schiff base condensation reaction between 1-methylimidazole-2-carboxaldehyde and the respective hydrazide, that occurs in a single step and is depicted in Figure 15.

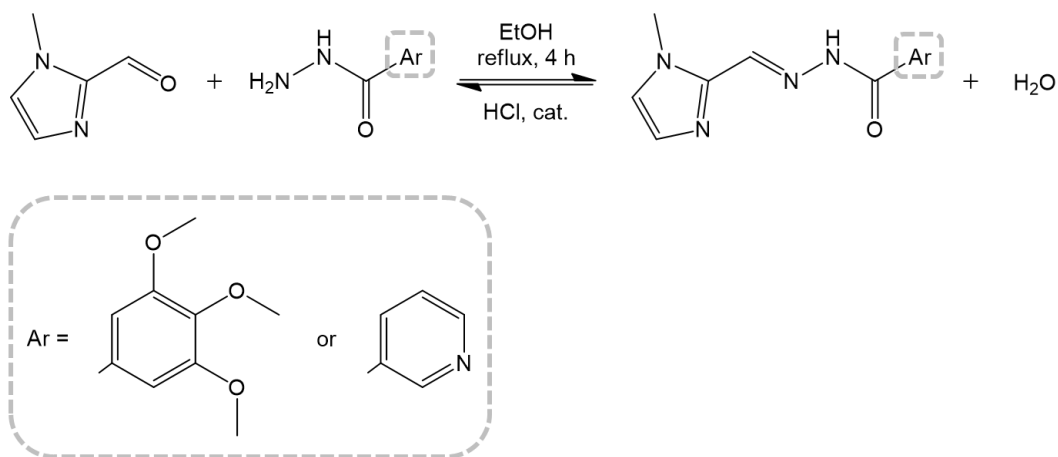


Figure 15. Generic scheme for the synthesis of the *N*-acylhydrazones **X1TMP** and **X1NIC**.

3. Objectives

3.1. General objective

To expand and develop the new generation of bioactive *N*-acylhydrazones derived from 1-methylimidazole-2-carboxaldehyde, and to evaluate the potential of these new compounds in biophysical models of copper-enhanced neuroendocrine and endocrine aggregopathies.

3.2. Specific objectives

- To synthesize the proposed *N*-acylhydrazones;
- To structurally characterize the new hydrazonic ligands in solution and in the solid state through nuclear magnetic resonance, infrared spectroscopy, thermogravimetry and melting point determination;
- To evaluate the stability of the ligands in buffered solution;
- To determine the experimental values of the octanol-water partition coefficients of the considered *N*-acylhydrazones;
- To verify the preferred stoichiometry of the copper(II) complexes involving the synthesized compounds in solution and estimate their apparent affinity constants through calculations based on the Job method;
- To study the effect of the trimethoxy-containing compound (**X1TMP**) in the Cu^{2+} - $\text{A}\beta$ system using ^1H - ^{15}N HSQC NMR experiments;
- To carry out aggregation assays with the full-length $\text{A}\beta_{1-40}$ peptide and **X1TMP** in the presence and absence of Cu^{2+} , and to characterize the final state of aggregation using transmission electron microscopy;
- To evaluate, through the ascorbate consumption assay (UV-Vis), the ability of **X1TMP** to inhibit the copper-catalyzed production of ROS in the presence of the $\text{A}\beta_{1-16}$ peptide fragment;
- To confirm the interaction between IAPP and Cu^{2+} using the hIAPP₁₈₋₂₂ peptide fragment, and to evaluate the impact of **X1NIC** in this system, using 1D ^1H NMR (700 MHz) experiments;
- To study the IAPP-Cu-**X1NIC** system through cyclic voltammetry.

4. Methodology

All reagents and solvents used in this work were purchased from commercial sources in the highest purity available and employed without any additional purification. All solutions were prepared using ultra-pure water.

4.1. *In silico* pharmacological analyses

The descriptor parameters molecular weight, cLog P, cLog S, HBA, HBD, PSA and Druglikeness were calculated using the program Osiris Property Explorer: DataWarrior™, software freely available for download at <http://www.organic-chemistry.org/prog/peo/>, last accessed on February 1st, 2024.

4.2. Syntheses of the ligands

The hydrazone ligands were obtained through Schiff base condensation reactions between 1-methylimidazole-2-carboxaldehyde and its respective *N*-acylhydrazide. The aldehyde was weighed into a round bottom reaction flask and dissolved in ethanol. The hydrazide (3,4,5-trimethoxybenzoic acid hydrazide for **X1TMP** and nicotinic acid hydrazide for **X1NIC**) was weighed in order to attain the 1:1 molar ratio and solubilized in the same solvent. Syntheses were performed in the 0.5 to 3.0 mmol range, using the least volume of solvent necessary for the dissolution of each reagent. The hydrazide was then dropwise added to the aldehyde, under constant stirring and gentle heating (up to 50 °C). Concentrated HCl was added as a catalyst to the mixture, which was then kept under constant stirring and reflux for 4 hours. The precipitates were isolated through filtration after cooling (**X1NIC**) or slow evaporation of the solvent (**X1TMP**), washed with cold ethanol and dried at room temperature.

The unsubstituted analogue of **X1TMP**, namely 1-methyl-1H-imidazole-2-carboxaldehyde benzoyl hydrazone (**X1Benz**), was employed as a comparative ligand in the studies involving the A β system. This ligand was prepared as described in (Cukierman, 2021).

For the specific synthesis of the (*Z*)-isomer of the nicotinic-inspired ligand, **X1NIC-(Z)**, after the addition of nicotinic acid hydrazide onto 1-methylimidazole-2-carboxaldehyde, no acid was added, and the reaction mixture

was kept under constant stirring and reflux for 24 hours. Precipitate was isolated through filtration after cooling of the solution, washed with cold ethanol and dried at room temperature.

4.3. Characterization

New ligands were characterized in the solid state by mid-infrared vibrational spectroscopy (IR), thermogravimetry (TG) and melting point (MP) determinations, and in solution through nuclear magnetic resonance (NMR).

4.3.1. Infrared Vibrational Spectroscopy (IR)

The analyses were carried out in an absorption spectrophotometer in the mid-infrared region, either in the 100 FT-IR or 400 FT-IR models, Perkin-Elmer™, and the data were collected in the range of 4000-400 cm^{-1} . Pellets of the samples were prepared in potassium bromide.

4.3.2. Thermogravimetry (TG)

These studies were conducted in a Perkin-Elmer™ analyzer, model Pyris 1 TGA, under nitrogen atmosphere, in the range of 25-900 °C, using a heating rate of 10 °C min^{-1} .

4.3.3. Melting Point (MP)

The determinations of the melting points of the organic ligands were performed in a Fisatom™ model 431 apparatus, in triplicate.

4.3.4. Nuclear Magnetic Resonance (NMR)

Nuclear magnetic resonance spectra of hydrogen and carbon, as well as NOESY correlation maps were obtained on a Bruker™ Avance III HD-400 spectrometer (operating at 400 MHz for ^1H and 100 MHz for ^{13}C) at 298 K. Samples were dissolved in 0.5 mL of deuterated dimethylsulfoxide ($\text{DMSO-}d_6$) and the spectra were calibrated based on the residual solvent signal (quintet at 2.50 ppm for the ^1H nucleus and septet at 39.52 for the ^{13}C nucleus). These

analyses were performed at the Analytical Facilities “Pe. Leopoldo Hainberger”, from the Department of Chemistry at PUC-Rio.

4.3.5. Electrospray Ionization Mass Spectrometry (ESI-MS)

ESI-MS(+) spectra were collected on a Perkin-Elmer™ SQ-300 mass spectrometer. Stock solutions of the samples were prepared by dissolving 1.0 mg of the compounds in 1.0 mL of methanol. Aliquots of 20 μL of these solutions were diluted in 980 μL of methanol and analyzed by direct infusion. Standard configuration parameters were used. These analyses were performed at the Multiuser Mass Spectrometry Laboratory of the Federal Fluminense University (LAMEM – UFF, Niterói, Brazil).

4.4. Stability assay in buffered solution

The compounds were initially prepared in 100% DMSO (stock solutions of $5 \times 10^{-3} \text{ mol L}^{-1}$) and were then diluted to $5 \times 10^{-5} \text{ mol L}^{-1}$ in solutions containing 1% DMSO/Tris 10 mmol L^{-1} (pH 7.4). The spectra of the *N*-acylhydrazones were acquired at regular intervals for 12 hours. A single spectrum of the precursor aldehyde and each hydrazide was registered under the same solvent and concentration conditions for comparison purposes. All spectra were acquired between the wavelengths of 200 and 800 nm at room temperature, in an Agilent™ Cary 100 spectrophotometer.

4.5. X1NIC-(E) / X1NIC-(Z) temperature stability

Both isomers were prepared at 0.018 mol L^{-1} [0.0025 g for X1NIC-(E) and 0.0020 g for X1NIC-(Z)] in 500 μL DMSO- d_6 and transferred to 5 mm NMR tubes. ^1H NMR spectra (Bruker™ Avance III HD-400) were acquired, for each isomer, at different, increasing temperatures (25, 35, 45, 55 and 65 °C). A final spectrum was then obtained, after cooling the sample from 65 to 25 °C. This assay was performed at the Analytical Facilities “Pe. Leopoldo Hainberger”, from the Department of Chemistry at PUC-Rio.

4.6. Octanol-water partition coefficient (log P)

The partition coefficient (log P) in the 1-octanol/water system was calculated using the shake-flask method. Tris buffer 10^{-2} mol L⁻¹ pH 7.4 was used as the aqueous phase. Both phases, organic and aqueous, were prepared separately with the hydrazone at low concentrations (5×10^{-5} mol L⁻¹) from 2×10^{-4} mol L⁻¹ stock solutions. Then, the UV-Vis spectrum (Agilent™ Cary 100 spectrophotometer) was recorded for each phase before mixing them. The flask containing the mixture was shaken vigorously at 37 °C, protected from light, for 3 hours (ThermoShaker, KASVI™). At the end of the incubation, the mixture was centrifuged for 10 min at 3000 rpm, and the layers separated with Pasteur pipettes. Concentrations in both phases were measured at the wavelength of higher absorption for each hydrazone, through a calibration curve. Each compound was analyzed in triplicate, and log P was calculated as the logarithm of the mean Co/Cw concentration ratio, in which Co is the final concentration in the organic phase and Cw is the final concentration in the aqueous phase.

4.7. Method of continuous variations (Job Plot)

The apparent affinity of the ligands for copper(II) ions and the stoichiometry of the reactions were evaluated, in solution, using the Method of Continuous Variations (Job's method) monitored through UV-Vis (Agilent™ Cary 100 spectrophotometer), in triplicates. While this method is mainly used for determining complex stoichiometries, under some specific conditions, such as the formation of only one complex species, little or no overlapping of free and complexed ligand bands, and strong metal-ligand affinity, an apparent constant (K_{app}) can be obtained from the data. To do so, initially, the molar absorptivity of the ligand was determined through a calibration curve in HEPES buffer (50 mmol L⁻¹, pH 7.4). Then, mixtures of different ligand to metal molar fractions were prepared as usual, from stock solutions of each ligand and $\text{CuCl}_2 \cdot 2 \text{H}_2\text{O}$, also in HEPES, at a concentration of 5×10^{-5} mol L⁻¹. The mixtures were stirred at 25 °C and 500 rpm until the moment of analysis. A “theoretical” molar absorptivity for the formed complex is calculated at the point of intersection of the lines using the Lambert-Beer equation. The complex concentration at the equilibrium is then

estimated from this ϵ value according to the maximum experimental absorbance of its band. The free ligand concentration at the equilibrium, on the other hand, is determined from the remaining absorbance of the hydrazone band in the sample of molar fraction related to the observed stoichiometry. Finally, an apparent affinity constant can be characterized considering the equilibrium concentrations of complex, ligand, and metal (calculated considering the reaction stoichiometry) by the fundamental equation $K_{app} = \frac{[ML]}{[L][M]}$, valid for a 1:1 complex.

4.8. Simultaneous Cu²⁺ interactions with X1NIC-(E) and X1NIC-(Z)

Stock solutions of the ligands were prepared at 0.025 mol L⁻¹ [0.0021 g for X1NIC-(E) and 0.0017 g for X1NIC-(Z)] in 300 μ L DMSO-*d*₆ each. 0.0021 g of CuCl₂ · 2 H₂O was dissolved in 200 μ L D₂O, attaining a stock concentration of 0.0617 mol L⁻¹. In the same 5 mm NMR tube, 250 μ L of each isomer were added, and a ¹H spectrum (Bruker™ Avance III HD-400) of this mixture was acquired for comparison purposes. Then, 5 μ L (0.05 eq) of the metal solution was added and another ¹H spectrum was recorded. Measurements were performed at 298 K.

4.9. Ascorbate consumption assay

The ascorbate consumption assay was performed by measuring the absorbance of ascorbate at 265 nm ($\epsilon = 14,500$ L mol⁻¹ cm⁻¹) as a function of time, using an Agilent™ Cary 100 spectrophotometer. A kinetic method was employed, with measurements being registered every 0.1s. The A β ₁₋₁₆ peptide fragment (GenScript™, amino acid sequence DAEFRHDSGYEVHHQK) was employed since it constitutes the coordinating portion of the A β peptide.

Stock solutions of the *N*-acylhydrazones (5 mmol L⁻¹), copper(II) chloride (2.25 mmol L⁻¹) and peptide (2.50 mmol L⁻¹) were prepared in ultrapure water, while ascorbate (5 mmol L⁻¹) was prepared in HEPES buffer (50 mmol L⁻¹, pH 7.4), before each measurement. For every experiment, to a 1.0 cm pathlength 3 mL quartz cuvette, 2450 μ L of buffer was added, followed by the addition of 50 μ L of ascorbate stock solution and, after two minutes, 10 μ L of A β ₁₋₁₆ peptide. 10 μ L from Cu²⁺ stock solution was added two minutes later. When the compounds

were involved, when absorbance reached ~ 1 A.U., either 5, 15 or 25 μL were added for 1, 3 and 5 eq. respectively. Thus, final concentrations in the cuvette were: [ascorbate] = 100 $\mu\text{mol L}^{-1}$, $[\text{Cu}^{2+}] = 9 \mu\text{mol L}^{-1}$, $[\text{A}\beta_{1-16}] = 10 \mu\text{mol L}^{-1}$, [ligand] = 0, 10, 30 or 50 $\mu\text{mol L}^{-1}$ and [HEPES] = 50 mmol L^{-1} . Measurements were performed in triplicate. Statistics (t -tests with a significance level of $p < 0.05$) were performed in GraphPad™ Prism software.

4.10. $\text{A}\beta_{1-40}$ aggregation

The peptide stock solution (577.39 $\mu\text{mol L}^{-1}$) was prepared by dissolving 1 mg of lyophilized synthetic human $\text{A}\beta_{1-40}$ peptide (GenScript™) in 400 μL of NaOH (10 mmol L^{-1}), divided into 20 μL aliquots and stored at $-20 \text{ }^\circ\text{C}$ until analyses. $\text{CuCl}_2 \cdot 2 \text{H}_2\text{O}$ stock solution (500 $\mu\text{mol L}^{-1}$) was prepared in ultrapure water, while stock solutions of ligands (500 $\mu\text{mol L}^{-1}$) were prepared in HEPES buffer (20 mmol L^{-1} , pH 6.6) containing 150 mmol L^{-1} NaCl.

The turbidity assay was conducted in flat-bottomed 96-well assay plates, in triplicate, in which the final volume of each well was 100 μL . The final plate concentration was: $[\text{A}\beta_{1-40}] = 25 \mu\text{mol L}^{-1}$, $[\text{Cu}^{2+}] = 25 \mu\text{mol L}^{-1}$, [ligand] = 25 or 75 $\mu\text{mol L}^{-1}$. To prevent biological contamination of the samples, sodium azide (7.7 mmol L^{-1}) was added to all wells. The solutions were incubated for 3 hours at 37 $^\circ\text{C}$ under constant agitation at 1100 rpm (ThermoShaker, KASVI™) and absorbance was measured at 405 nm using a Varioskan™ LUX Thermo Scientific plate reader. Ligands, metal and buffer were subtracted correspondingly.

Alternatively, for the copper-containing samples, the same preparation was assembled in black 96-well plates, with the addition of 10 $\mu\text{mol L}^{-1}$ thioflavin-T (ThT), and measured with excitation at 450 nm and emission spectra recorded between 460 and 600 nm after 3 hours of incubation at 37 $^\circ\text{C}$ and 1100 rpm.

4.11. Transmission Electron Microscopy (TEM)

Transmission electron microscopy (TEM) images were performed with pooled samples obtained at the end of the aggregation assay. Samples were adhered to a formvar/carbon coated grid and then stained with 2% uranyl acetate solution. A FEI Tecnai™ T20 electron microscope was used to obtain the images,

at the National Center for Structural Biology and Bioimaging (CENABIO – UFRJ, Rio de Janeiro, Brazil).

4.12. ^1H and ^1H - ^{15}N HSQC NMR of the Cu^{2+} - $\text{A}\beta_{1-40}$ -X1Benz system

Non-labeled and ^{15}N isotopically enriched $\text{A}\beta_{1-40}$ peptide samples were purchased from EZBiolabTM (Carmel, IN) and AlexotechTM (Oslo, Norway), respectively. NMR spectra were acquired on a 600 MHz Avance III (BrukerTM, Billerica, MA) equipped with a cryogenically cooled triple-resonance $^1\text{H}(^{13}\text{C}/^{15}\text{N})$ TCl probe. Heteronuclear NMR experiments were performed with pulsed-field-gradient-enhanced sequences on $80 \mu\text{mol L}^{-1}$ ^{15}N -labeled peptide samples in 20 mmol L^{-1} Tris buffer (pH 7.3) at $15 \text{ }^\circ\text{C}$ containing 1% of DMSO. 1D ^1H NMR experiments, on the other hand, were acquired on unlabeled $\text{A}\beta_{1-40}$ samples under the same experimental conditions. Aggregation did not occur at such low temperature and in the absence of stirring.

For the mapping experiments, ^1H - ^{15}N heteronuclear single quantum correlation (HSQC) amide cross-peaks affected during hydrazone titration were identified by comparing their chemical shifts with those of the same cross-peaks in the data set of samples lacking the compound. Mean weighted chemical shift displacements (^1H - ^{15}N MWCS) were calculated as $[(\Delta\delta \text{ } ^1\text{H})^2 + (\Delta\delta \text{ } ^{15}\text{N})^2/25]^{1/2}$ (Cavanagh *et al.*, 2007). Acquisition and processing of NMR spectra were performed using TOPSPIN 7.0 (BrukerTM Biospin). 2D spectra analysis and visualization were performed with CCPNTM.

These studies were carried out in collaboration with the research group of Prof. Dr. Claudio O. Fernández (IBR-CONICET), Max Planck Laboratory, Rosario, Argentina.

4.13. ^1H NMR of the Cu^{2+} -hIAPP₁₈₋₂₂ and the Cu^{2+} -hIAPP₁₈₋₂₂-X1NIC system

All NMR spectra of the hIAPP₁₈₋₂₂ fragment peptide (GenScriptTM, amino acid sequence HSSNN · 2 TFA, molecular weight $785.56 \text{ g mol}^{-1}$) were collected at $25 \text{ }^\circ\text{C}$ on a BrukerTM Avance III 700 MHz spectrometer using a TXI inverse detection triple resonance probe (^{15}N , ^{13}C , ^1H). This equipment is located in the

Jiri Jonas National Nuclear Magnetic Resonance Center from the National Center for Structural Biology and Bioimaging (CENABIO), UFRJ, Rio de Janeiro, Brazil. A 20 mmol L⁻¹ Tris-*d*₁₁ buffer was prepared in ultrapure water, adjusted to pH 7.4, and filtered with the help of a 0.22 μm syringe filter. Then, 0.5 mg of the peptide was dissolved in 520 μL of this buffer, with the addition 50 μL D₂O and 25 μL DMSO-*d*₆, resulting in a 1.0 mmol L⁻¹ peptide solution, which was transferred to a 5 mm NMR tube. A ¹H spectrum was initially acquired for the free hIAPP₁₈₋₂₂, then with the addition of 0.1 equivalent of Cu²⁺, from a stock solution of 0.0318 mmol L⁻¹ CuCl₂ · 2 H₂O in D₂O. After that, 0.1 and 1.0 equivalents of either **X1NIC-(E)** or **X1NIC-(Z)** were successively added and new spectra acquired for each condition. Ligands were prepared as 0.0636 mol L⁻¹ DMSO-*d*₆ stock solutions. All spectra were acquired and processed using TopSpin 3.5 software (Bruker™).

4.14. Cyclic Voltammetry (CV) of the Cu²⁺-hIAPP₁₈₋₂₂ and the Cu²⁺-hIAPP₁₈₋₂₂-X1NIC system

Electrochemical analyses were performed on a Basi™ Epsilon potentiostat with a C3 cell holder. A three-electrode system was used that was composed of a glassy carbon working electrode, an Ag/AgCl reference electrode, and a platinum auxiliary electrode. The hIAPP₁₈₋₂₂ peptide (GenScript™, amino acid sequence HSSNN · 2 TFA, molecular weight 785.56 g mol⁻¹) stock solution (0.5 mmol L⁻¹) was prepared in 50 mmol L⁻¹ HEPES pH 7.4, with 100 mmol L⁻¹ NaCl. The CuCl₂ · 2 H₂O stock solution was prepared at a concentration of 5 mmol L⁻¹ in ultrapure water. Stock solutions of the ligands were also made at a concentration of 5 mmol L⁻¹, but in anhydrous DMSO, due to the low solubility of the (Z) isomer. The analyses were made with 3 mL of buffer containing 5% anhydrous DMSO in the cell. The peptide was diluted to a final concentration of 0.1 mmol L⁻¹. Then, 1 equivalent of Cu²⁺ was added, followed by the titration of the ligands from 0.1 to 2 equivalents. CVs were collected at a scan rate of 100 mV s⁻¹ over a potential range of 500 mV to -500 mV, under nitrogen atmosphere.

5. Results and Discussion

The main goal of this work was to continue developing, in order to expand our knowledge, the new family of *N*-acylhydrazones derived from the 1-methylimidazole-2-carboxaldehyde, which was the subject of patent applications by our research group in 2020 (BR1020200054236 and PCT/BR2021/050107), as well as to evaluate such compounds in different biophysical models of neuroendocrine and endocrine copper-enhanced aggregopathies. In this context, two new bioinspired ligands were designed: **X1TMP**, based on the structure of the natural psycho-active agent mescaline, and **X1NIC**, considering its similarity to nicotine. The first compound was evaluated in the context of Alzheimer's disease, since mescaline can easily reach the brain and selectively bind and activate serotonin receptors (Stork *et al.*, 2014). On the other hand, **X1NIC** was tested in models of type II diabetes *mellitus*, in view of the existence of nicotinic receptors in pancreatic islets and β -cells (Yoshikawa *et al.*, 2005). Thus, for the sake of simplicity, the Results and Discussion section was divided into two parts, one for each compound/disease.

5.1. Part I – New mescaline-related *N*-acylhydrazone and its unsubstituted benzoyl derivative as metallophores towards copper-associated models of Alzheimer's disease

The results described in this section were the subject of a publication in the Journal of Inorganic Biochemistry (Carvalho *et al.*, 2023).

In order to evaluate whether the presence of the three methoxyl substituents in **X1TMP** would impact some pharmacologically relevant parameters such as the partition coefficient, the coordinating ability towards Cu^{2+} , and, consequently, the metallophore potential of this *N*-acylhydrazone, we decided to include in the study its unsubstituted benzoyl derivative, **X1Benz**, as a related model. The synthesis, characterization, and evaluation of this compound in a cell model of Parkinson's disease was already reported in a previous doctoral thesis developed in our research group (Cukierman, 2021). However, its preparation was only now published, together with the promising anti-Alzheimer's activity that was assessed in this project.

Since **X1Benz** was synthesized again by the author of the present work, some of its structural characterizations will also be discussed within this section.

5.1.1. Syntheses and characterization

Both hydrazones were isolated as white, polycrystalline solids in good yields (83% and 72%, respectively for **X1TMP** and **X1Benz**). The latter was also obtained as single crystals, which confirmed its (*E*)-configuration around the C=N bond, with no intramolecular H bonds (Carvalho *et al.*, 2023; Cukierman, 2021). X-ray diffraction measurements also demonstrated the presence of three water molecules in the structure, and that the compound is in its hydrochloride form (**HX1Benz**⁺Cl⁻ · 3H₂O, C₁₂H₁₉N₄O₄Cl, 318.71 g mol⁻¹, M. P. = 128 ± 1 °C), since the imidazole nitrogen is protonated in the synthesis due to the acidic conditions employed.

In order to confirm the state of hydration and protonation of **X1TMP**, for which it was not possible to obtain single crystals, a thermogravimetric curve was recorded. Two mass losses, between 150 and 290 °C, were observed, corresponding to the release of a hydration water molecule, followed by the loss of HCl, thus yielding the formula **HX1TMP**⁺Cl⁻ · H₂O (C₁₅H₂₁N₄O₅Cl, 372.80 g mol⁻¹, M. P. = 205 °C – dec.).

Obtention of the compounds was also confirmed through ESI-MS, with a peak at *m/z*⁺ 319.30 for **HX1TMP**⁺ and at *m/z*⁺ 229.16 for **HX1Benz**⁺ (Figure 16A and B).

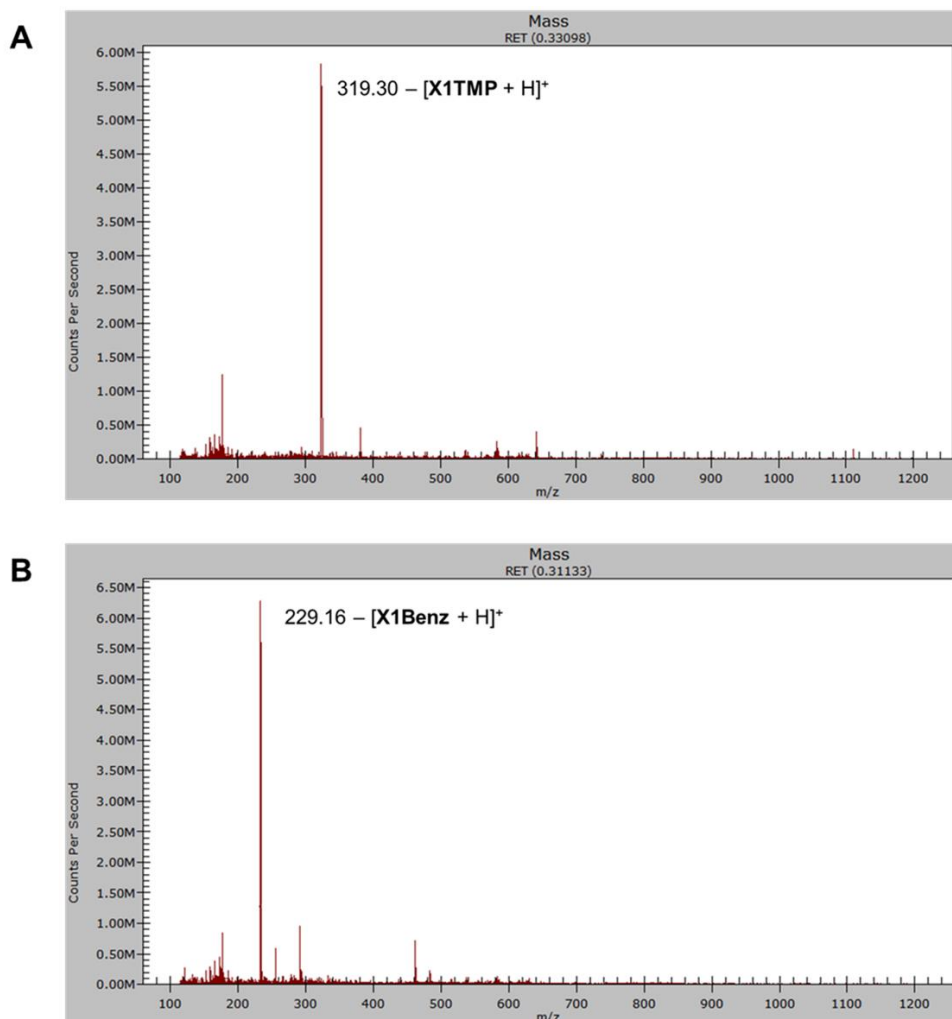


Figure 16. ESI-MS spectra (positive mode) of (A) **X1TMP** and (B) **X1Benz** in methanol.

Solid state characterization of the two compounds was also performed through mid-infrared spectroscopy, as shown in Figure 17A and B, respectively for **X1TMP** and **X1Benz**. Both compounds show typical *N*-acylhydrazonic bands, such as $\nu(N-H)$, $\nu(C=O)$, $\nu(C=N)$ and $\nu(N-N)$, as well as specific bands related to the presence of water molecules and the imidazole ring. Main absorptions and their assignments are detailed in Table 1. The existence of distinct bands, resulting from the presence of the substituents in the aromatic ring derived from the 3,4,5-trimethoxybenzoic acid hydrazide, was verified, which constitutes the main difference between the ligands: the methoxyl $\nu(C-H)$ absorption, occurring at 2965 and 2944 cm^{-1} , and its $\nu(C-O)$ at 1226 and 1130 cm^{-1} .

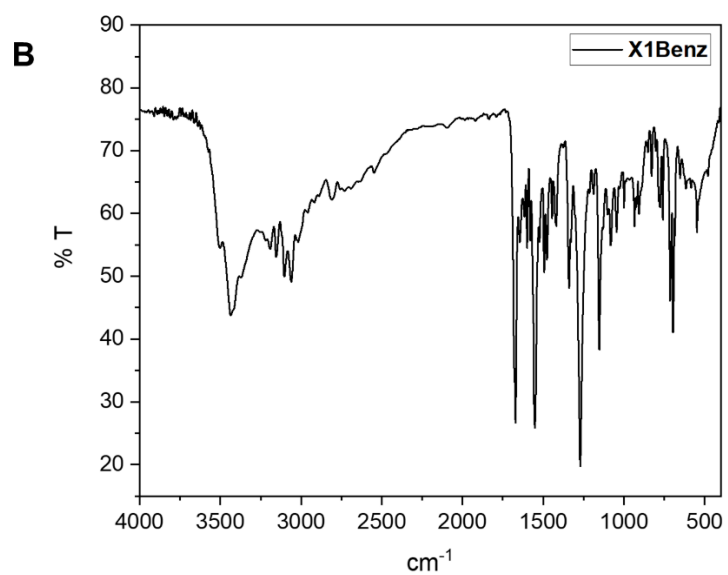
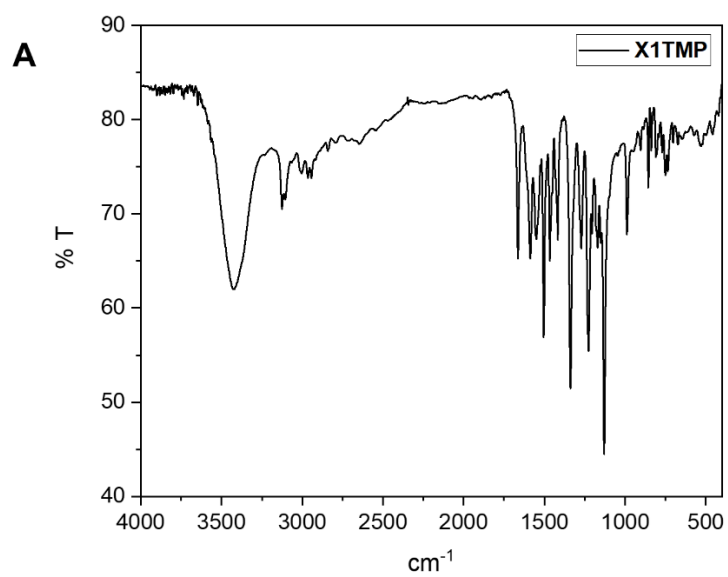


Figure 17. Mid-infrared of (A) **X1TMP** and (B) **X1Benz**. Samples were prepared as KBr pellets.

Table 1. Selected infrared frequencies of the *N*-acylhydrazones **X1TMP** and **X1Benz**, along with their assignments. Samples were prepared as KBr pellets.

Assignment	X1TMP	X1Benz
	IR (cm ⁻¹)	IR (cm ⁻¹)
$\nu(\text{O-H})_{\text{water}}$	3426	3508, 3438 and 3422
$\nu(\text{N}^+-\text{H})_{\text{imidazole}}$	3125	3153
$\nu(\text{N-H})_{\text{hydrazone}}$	3105	3102
$\nu(\text{C-H})_{\text{methoxyl}}$	2965 and 2944	-
$\nu(\text{C=O})_{\text{amide}}$	1664	1680
$\nu(\text{C=N})_{\text{azomethine}}$	1605	1619
Skeletal modes, imidazolium cation	1552	1562 and 1557
$\nu(\text{C-C})_{\text{benzene}}$	1504, 1466 and 1452	1602, 1494 and 1446
Coupled $\nu(\text{C-N})$ / $\nu(\text{C-C})_{\text{imidazole}}$	1524 and 1418	1525, 1481 and 1419
$\nu(\text{N-N})$	1100	1131
$\nu(\text{C-O})_{\text{methoxyl}}$	1226 and 1130	-
$\delta(\text{H}_2\text{O})$	-	1648

Typically, hydrazones have a rich solution chemistry involving (*E*)/(*Z*) isomers, *anti/syn* conformations and amido/iminol tautomers, that can be studied through ¹H NMR spectroscopy (Cukierman *et al.*, 2018). However, the great experience of our research group indicates that the hydrochloride forms of *N*-acylhydrazones containing 1-methylimidazole usually display only one set of signals in DMSO-*d*₆, suggesting the presence of only one major constituent in solution. This is also the case for both studied ligands herein, **X1TMP** and **X1Benz**, as can be seen in Figure 18A and B, respectively. The main difference between the spectra is related to the signals at 3.74 (3H) and 3.88 (6H) ppm, which were attributed to the three methoxyl substituents in **X1TMP**. This also implies a lesser number of aromatic signals for this compound. NMR spectroscopy shows that both compounds were obtained at a high purity level. Chemical shifts and signal assignments are described in Table 2, and carbon NMR spectra are shown in Figure 19A and B.

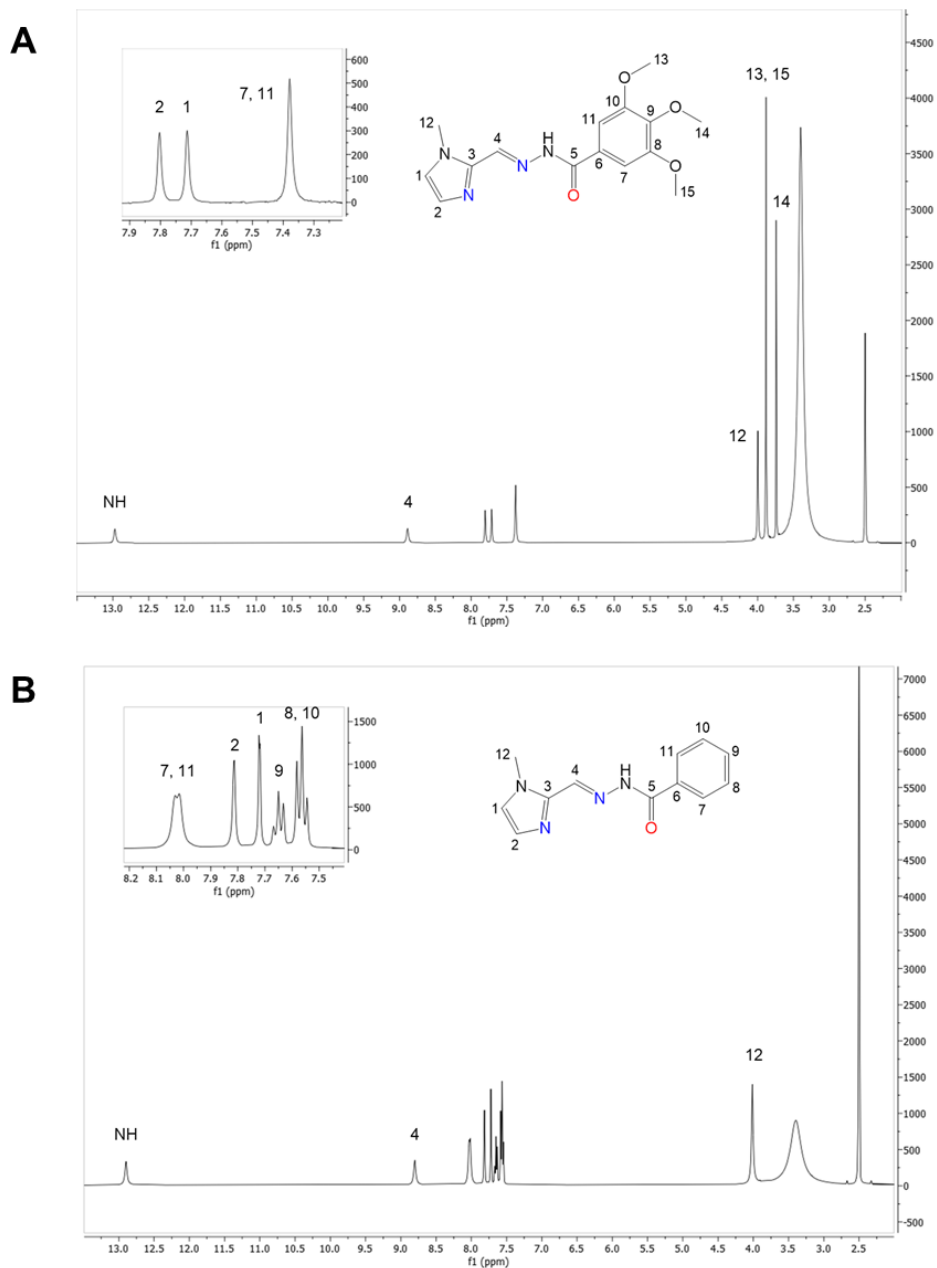


Figure 18. ^1H NMR spectra (400 MHz) of the studied *N*-acylhydrazones in $\text{DMSO-}d_6$ at 25°C .
(A) X1TMP and **(B) X1Benz**.

Table 2. ¹H (400 MHz) signal attribution for **X1TMP** and **X1Benz** (DMSO-*d*₆ at 25 °C).

	X1TMP	X1Benz
H	δ (ppm)	δ (ppm)
1	7.71 (s, 1H)	7.72 (s, 1H)
2	7.80 (s, 1H)	7.81 (s, 1H)
4	8.89 (s, 1H)	8.80 (s, 1H)
7	7.38 (s, 2H)*	8.02 (d, 2H, ³ J _{HH} = 5.92 Hz)*
8	-	7.56 (t, 2H, ³ J _{HH} = 7.48 Hz)**
9	-	7.65 (t, 1H, ³ J _{HH} = 7.76 Hz)
10	-	7.56 (t, 2H, ³ J _{HH} = 7.48 Hz)**
11	7.38 (s, 2H)*	8.02 (d, 2H, ³ J _{HH} = 5.92 Hz)*
12	4.00 (s, 3H)	4.01 (s, 3H)
13	3.88 (s, 6H)**	-
14	3.74 (s, 3H)	-
15	3.88 (s, 6H)**	-
NH	12.97 (s, 1H)	12.90 (s, 1H)

Signal multiplicity: (s: singlet; d: doublet; t: triplet). (*) and (**) stands for equivalences.

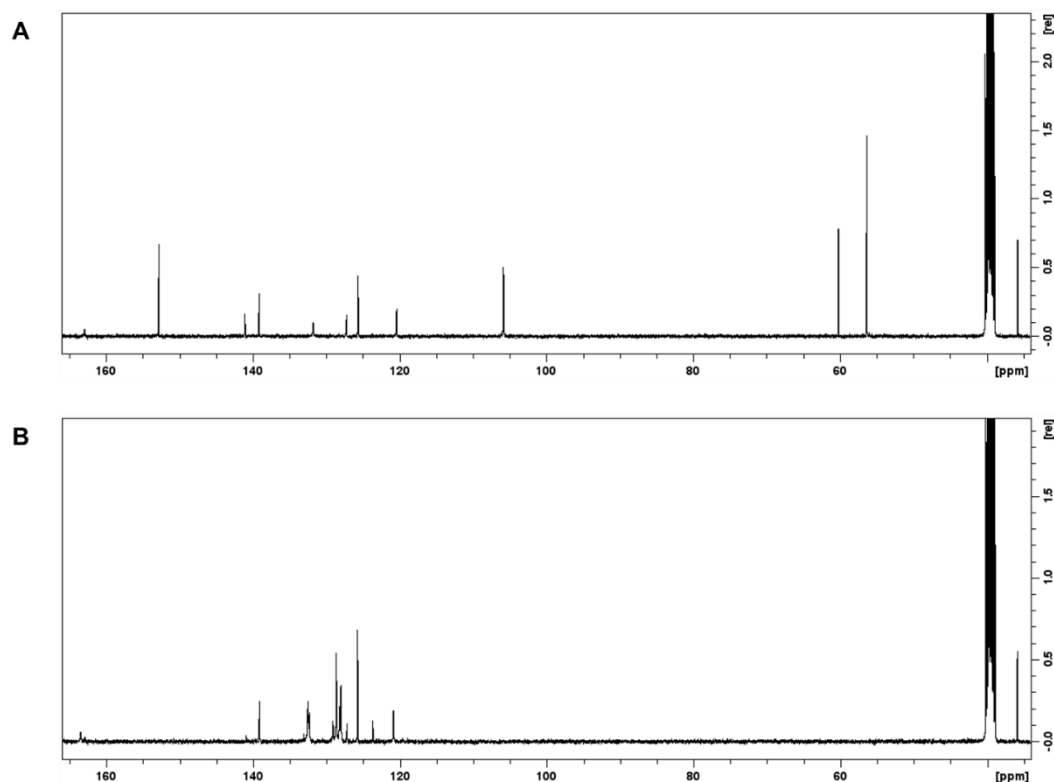


Figure 19. ^{13}C NMR spectra (100 MHz) of the studied *N*-acylhydrazones in $\text{DMSO-}d_6$ at 25 °C. (A) δ_{X1TMP} : 35.73, 56.29, 60.16, 105.80, 120.35, 125.60, 127.18, 131.77, 139.09, 141.02, 152.78, 162.87 ppm. (B) δ_{X1Benz} : 35.85, 120.84, 125.71, 128.01, 128.64, 129.08, 132.28, 132.48, 139.07, 163.45 ppm.

5.1.2. Stability towards hydrolysis in buffered solution

Since *N*-acylhydrazones are usually prone to hydrolysis in water, we assessed the compounds' stability in a buffered medium (10 mmol L⁻¹ Tris pH 7.4) containing 1% DMSO, at a ligand concentration of 5 x 10⁻⁵ mol L⁻¹.

The UV-Vis absorption spectrum of **X1TMP** showed only one band, centered at 317 nm, which loses less than 1% of absorbance during the 12 hours of experiment (Figure 20), demonstrating that the compound is very stable under the studied conditions.

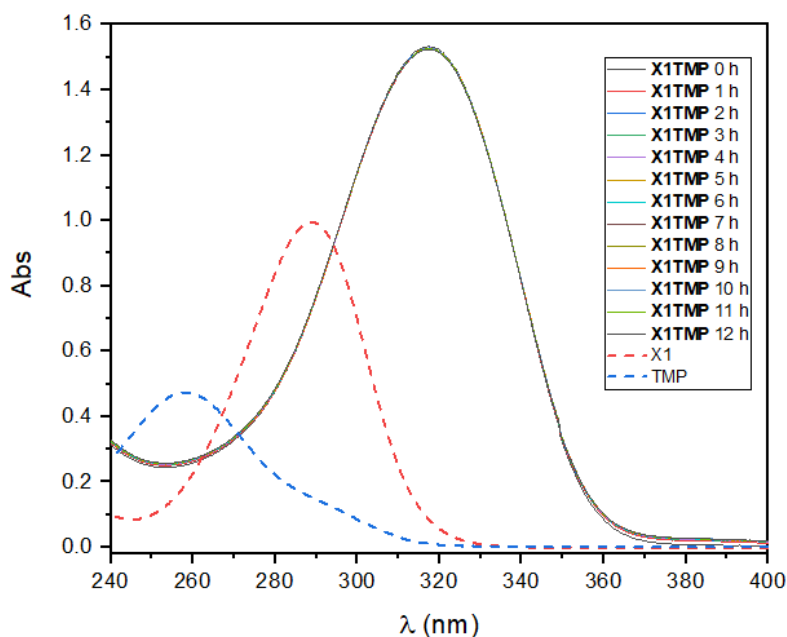


Figure 20. UV-Vis absorption spectra of **X1TMP** and its precursors ($5 \times 10^{-5} \text{ mol L}^{-1}$) in 1% DMSO/Tris (10 mmol L^{-1} , pH 7.4), obtained over a period of 12 h, at room temperature.

The **X1Benz** ligand presents a very similar absorption spectrum, with a single apparent band in this region, centered at 315 nm. Just like the trimethoxy-substituted analogue, **X1Benz** is highly stable in an aqueous medium, with practically insignificant hydrolysis, well below 1% (Figure 21).

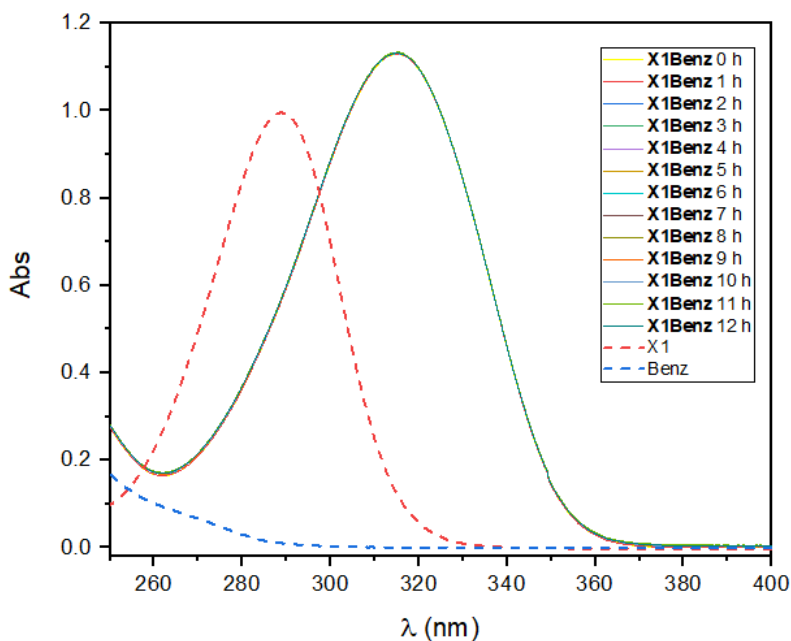


Figure 21. UV-Vis absorption spectra of **X1Benz** and its precursors ($5 \times 10^{-5} \text{ mol L}^{-1}$) in 1% DMSO/Tris (10 mmol L^{-1} , pH 7.4), obtained over a period of 12 h, at room temperature.

5.1.3. Pharmacological parameters

For the theoretical prediction of the oral bioavailability profile and permeability of compounds through cellular membranes and the blood-brain barrier, a preliminary *in silico* analysis was performed. Lipinski's Rule of Five has been widely employed as a guideline to assess if the studied compound has ideal physicochemical properties for the development as a drug candidate for oral administration (Lipinski *et al.*, 2001). In this context, both compounds are in accordance to Lipinski's Rule of Five, *i.e.*, $\log P \leq 5$ (partition coefficient), $MW \leq 500 \text{ g mol}^{-1}$ (molecular weight), $HBA \leq 10$ (hydrogen bond acceptors) and $HBD \leq 5$ (hydrogen bond donors) (Lipinski *et al.*, 2001). Calculated values for $\log P$ and other important descriptors are shown in Table 3.

Table 3. Calculated (OSIRIS Property Explorer: DataWarrior™) descriptors of pharmacological relevance for **X1TMP** and **X1Benz**. MW: molecular weight, cLog P: calculated partition coefficient, cLog S: calculated water solubility, PSA: polar surface area.

	MW (g mol ⁻¹)	cLog P	cLog S	PSA (Å ²)	Druglikeness	DrugScore
X1TMP	318.00	1.17	-1.54	86.97	12.08	93%
X1Benz	228.00	1.38	-1.48	59.28	6.03	95%

A smaller MW is related to easier cellular membrane crossing. In this sense, the majority of drugs orally administered currently in the market present MW in the range of 200-450 g mol⁻¹ (Leeson & Young, 2015), like the synthesized *N*-acylhydrazones **X1TMP** and **X1Benz**. Log P represents the hydrophilic-lipophilic balance of the molecule that, combined with the solubility of the compound in aqueous solution (log S), is of extreme importance in the context of cellular permeability. A compromise between them must be reached in order for the potential drug to cross the lipid bilayer of the membranes (Van de Waterbeemd *et al.*, 1998). Finally, PSA is the polar surface area, which evaluates the degree of polarity of the molecule. Regarding blood-brain barrier crossing, it has been reported that compounds should exhibit a PSA of < 90 Å² (Van de Waterbeemd *et al.*, 1998). In this sense, both metallophores are in agreement with such guidelines.

Other parameters that can be taken into account in the analysis of a drug candidate are the Druglikeness and the DrugScore. The first is determined from the comparison of compound fragments with databases of both commercially available drugs and non-drug compounds. The latter, on the other hand, is a combination of the previously mentioned properties and expected toxicity risks in one value that is used to estimate the compound's overall potential to qualify for a drug. No indication of mutagenicity or tumorigenicity was found for the *N*-acylhydrazones **X1TMP** and **X1Benz**, nor any warnings for irritating or reproductive effects. For this reason, DrugScore values obtained were above 90%.

Apart from the calculated log P parameter, we determined its experimental values for both synthesized *N*-acylhydrazones through the shake flask method. A Tris buffer pH 7.40 was employed as the aqueous phase and 1-octanol was used as the organic phase. Nowadays, the optimal range of log P values for blood–brain barrier crossing is considered between 0 and 3 (Pajouhesh & Lenz, 2005). The values obtained for **X1TMP** and **X1Benz** are, respectively, 1.55 ± 0.17 and 1.49 ± 0.13 , close to the predicted values and inside the ideal range. It is important to note that, from the calculations, a lower log P was expected for the mescaline derivative **X1TMP**, which was not experimentally observed, since both hydrazones presented virtually the same value for this parameter. Moreover, despite the similarity of the calculated log S, a lower water solubility was experimentally observed for **X1TMP**, indicating that the presence of the methoxyl substituents somewhat impairs its solubility in the biological fluid. This trend is contrary to what would be expected from the theoretical relative PSA values. Nevertheless, **X1TMP** still presents enough solubility that allowed us to work in physiological-like conditions for most of the experiments.

5.1.4. Interactions with copper(II) in buffered pH 7.4, aqueous solution

The Method of Continuous Variations (Job Method), using UV-Vis spectroscopy as a suitable monitoring technique, was applied to estimate the apparent affinity of both ligands towards copper(II) ions. As shown above, the electronic spectra of **X1TMP** and **X1Benz** display only one main intra-ligand band each, centered at 318 nm ($\epsilon = 23,950 \pm 110 \text{ L mol}^{-1} \text{ cm}^{-1}$) and 315 nm ($\epsilon = 25,660 \pm 125 \text{ L mol}^{-1} \text{ cm}^{-1}$), respectively. Upon complexation those absorptions

undergo strong bathochromic shifts to 380 and 372 nm, correspondingly (Figure 22A and B). On the other hand, no copper(II) characteristic *d-d* band was observed due to the low concentration employed in this assay.

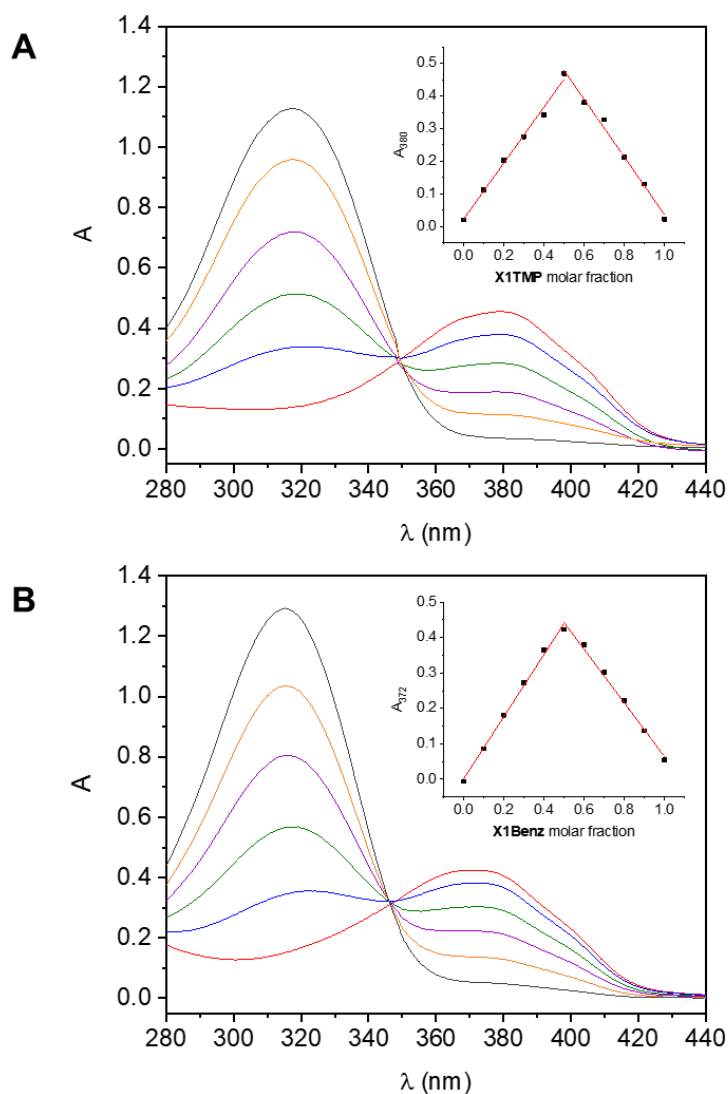


Figure 22. Method of continuous variations to evaluate the binding affinity of the new hydrazones (A) **X1TMP** and (B) **X1Benz** towards copper (II) – representative electronic spectra of ligand molar fractions from 0.5 to 1.0. *Insets:* absorbance versus molar fraction plots ($R^2 = 0.998$ for A and B). HEPES buffer at pH 7.4, 50 mmol L⁻¹, 25 °C.

In both cases, the maximum absorbance was achieved at the molar fraction of 0.5 (Figure 22A and B, *insets*), suggesting the formation of ML stoichiometry complexes. **X1TMP** and **X1Benz** seem to interact with copper(II) ions in a similar manner and with analogous affinities. While **X1TMP** showed an apparent log *K* of 5.74 ± 0.15 , **X1Benz** presented a slightly higher apparent log *K* value,

equal to 5.87 ± 0.11 . The fact that both constants were obtained under exactly the same experimental conditions make a direct comparison between them perfectly reliable. Thus, we can conclude that the electronic effects derived from the inclusion of methoxyl substituents in the phenyl group do not appear to cause major changes in the affinity of the ligands for copper(II) ions, which, for both hydrazones, is in the moderate range expected for a functional metallophore.

The group's previous works involving 1-methylimidazole-containing *N*-acylhydrazones have shown that these compounds exhibit a higher water solubility and remarkable resistance towards hydrolysis (Cukierman *et al.*, 2020; Cukierman *et al.*, 2022). This allowed us to work in buffered 100% aqueous media for ROS production and A β aggregation assays, a more physiological condition.

5.1.5. Interactions with the Cu²⁺-A β system: effect on ROS production

Free copper is highly effective in the generation of ROS through the cycling between its two physiologically available oxidation states (White *et al.*, 1999). Although certainly less than free copper, the Cu(A β) complex is still quite competent in catalyzing the production of ROS in the presence of dioxygen and ascorbate. In fact, ascorbate consumption mirrors ROS production and can be employed as a useful assay to determine the efficacy of copper-targeted metallophores in reducing oxidative stress (Atrián-Blasco *et al.*, 2018; Conte-Daban *et al.*, 2016). *N*-acylhydrazones **X1TMP** and **X1Benz** showed the ability to reduce copper-mediated ROS production in the preliminary study performed in the presence of A β ₁₋₁₆ (Figure 23). This fragment was used as a model for copper coordination with respect to the full-length peptide, since it comprises the binding region for the oxidized form of this metal (Faller & Hureau, 2009).

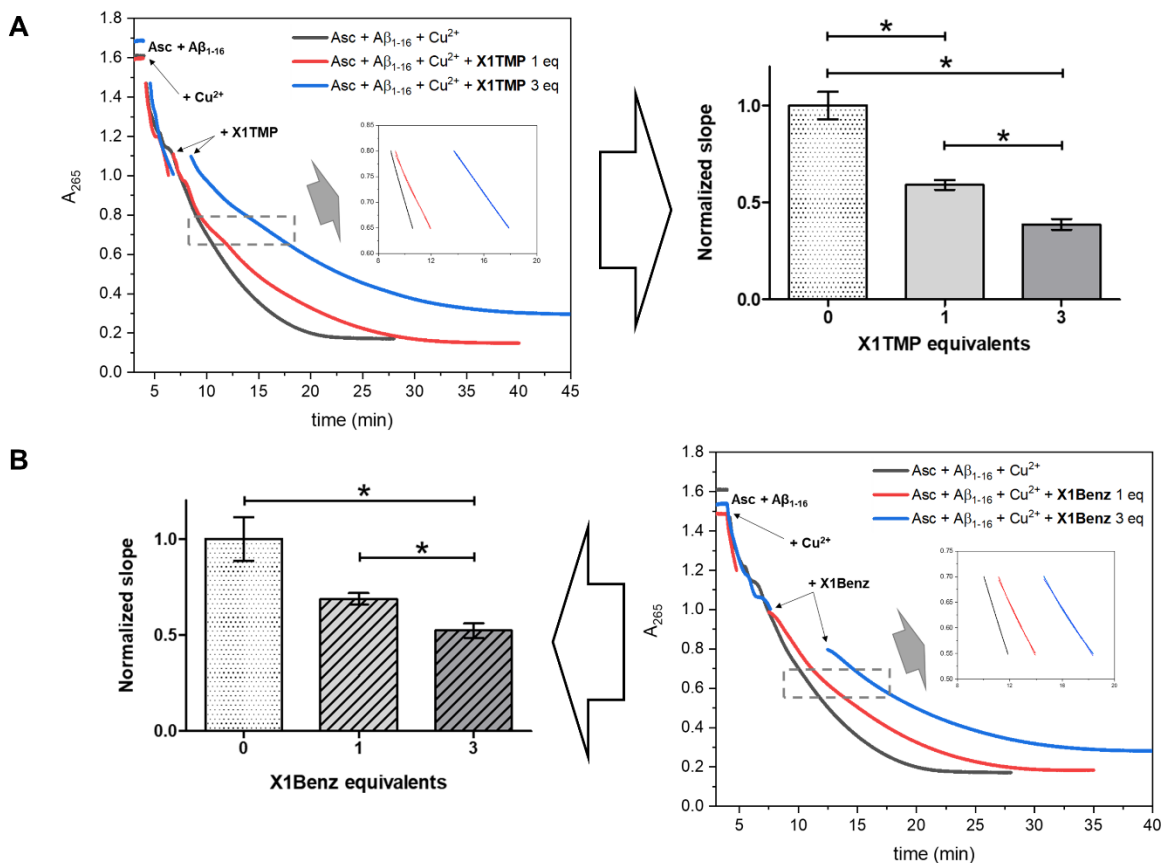


Figure 23. Cu(A β)-induced ascorbate consumption. **(A) Left:** Plots showing ascorbate consumption through absorbance decrease at 265 nm for Cu(A β) (black), Cu(A β) + 1 eq. X1TMP (red) and Cu(A β) + 3 eq. X1TMP (blue). The sharp increase observed after compound addition in excess is due to the intrinsic absorbance of the resulting Cu(X1TMP) interaction. *Inset:* Linear segment of the ascorbate consumption curve for $0.80 \leq A_{265} \leq 0.65$. Figures of merit: black line slope: -0.09018 ± 0.00009 , $R^2 = 0.999$; red line slope: -0.05430 ± 0.00009 , $R^2 = 0.996$; blue line slope: -0.036210 ± 0.000008 , $R^2 = 1.000$. **Right:** Bar graph representing the normalized mean slopes of the linear segment, which parallel ROS production, for each condition tested. Significant differences (*t*-tests) are characterized by (*) for $p < 0.05$. **(B) Right:** Representative plots showing ascorbate consumption through absorbance decrease at 265 nm for Cu(A β) (black), Cu(A β) + 1 eq. X1Benz (red) and Cu(A β) + 3 eq. X1Benz (blue). The sharp increase observed after compound addition in excess is due to the intrinsic absorbance of the resulting Cu(X1Benz) interaction. *Inset:* Linear segment of the ascorbate consumption curve for $0.70 \leq A_{265} \leq 0.55$. Figures of merit: black line slope: -0.08240 ± 0.00005 , $R^2 = 1.000$; red line slope: -0.05267 ± 0.00007 , $R^2 = 0.997$; blue line slope: -0.03997 ± 0.00004 , $R^2 = 0.997$. **Left:** Bar graph representing the normalized mean slopes of the linear segments.

The addition of copper(II) to a solution containing ascorbate and A β_{1-16} at pH 7.4 triggers an intensity reduction of the ascorbate absorption band centered at 265 nm. The initial consumption rate was estimated as $37.9 \pm 4.1 \mu\text{mol L}^{-1} \text{min}^{-1}$. After addition of 1 eq. of each hydrazone, it was observed that the consumption profile does not change appreciably until the ascorbate concentration reaches 50% of its original value. From that moment on, a clear divergence can be noticed

(gray box in Figure 23). The slope of the consumption curves (*inset*), normalized with respect to the Cu(A β) control condition, was employed as a measurement of the ascorbate oxidation rate at 25 °C. The bar graphs indicate that both compounds are able to reduce the ROS production by around 30-40%, being **X1TMP** slightly more active. The addition of a hydrazone excess (3 eq.) further prevents ascorbate oxidation. At this ratio, **X1TMP** is able to inhibit up to 60% of the reaction, against the 50% of hampering related to **X1Benz**. Another indication of the protective effect of the compounds can be assessed by the time needed to reach the equilibrium (when a variation in absorbance is no longer noticeable). While the Cu(A β) system stabilizes after 20 min, addition of **X1TMP** delays stabilization to around 30 min (1 eq.) and 35 min (3 eq.). Concerning the unsubstituted **X1Benz**, the values are around 25 min (1 eq.) and 35 min (3 eq.). Taken together, and in spite of the inherent limitations of the method, these data indicate that the presence of the studied *N*-acylhydrazones hinders ascorbate oxidation and, therefore, Cu(A β)-mediated ROS production.

5.1.6. Inhibition of A β aggregation via turbidity assay

Besides catalyzing the production of ROS, copper binding to A β also accelerates its amyloidogenic aggregation, as well as increases neuronal toxicity (Hane & Leonenko, 2014). Therefore, the next step in our investigation was to evaluate whether the synthesized *N*-acylhydrazonic metallophores would be able to interfere with this essential process as well. Since protein aggregates are known to scatter light in the visible region, we carried out a turbidity assay to determine the impact of the ligands in copper-mediated A β_{1-40} aggregation (Hall *et al.*, 2016). The pH of the medium was adjusted to slightly acidic (buffer solution at pH 6.6), since it has been described that optimal metal-binding leading to aggregation occurs under these specific conditions (Atwood *et al.*, 1998; Syme *et al.*, 2004). TEM and thioflavin-T fluorescence spectroscopy were used as supporting techniques in order to characterize the aggregates formed.

First, the effects of the compounds in the absence of copper(II) ions were evaluated. Interestingly, equimolar amounts of both *N*-acylhydrazones were able to radically prevent aggregation, as can be observed in Figure 24A (bars 1-3). This was confirmed through TEM images, which show the characteristic fibril

formation in the untreated A β sample (panel 24B) and its absence upon treatment with 1 eq. of **X1TMP** (24C) or **X1Benz** (24D).

Regarding the metal-induced process, it is important to note that copper is known to preferably stabilize intermediate oligomeric species over the well-structured, insoluble amyloid fibrils (Przygońska *et al.*, 2019; Sharma *et al.*, 2013; Stefaniak *et al.*, 2021). Thus, the presence of this physiological metal slightly increases solution turbidity in comparison to free A β , being the precipitate clearly characterized as mainly amorphous by TEM (dotted bar on Figure 24A and image in panel 24E) and confirmed through thioflavin-T assay, which indicates a fibrillization lessening of > 50% (Figure 25). The addition of 1 eq. of *N*-acylhydrazones **X1TMP** or **X1Benz** significantly reduces absorbance at 405 nm ($p < 0.05$), indicating a hampering of the aggregation process (light gray bars in Figure 24A). Representative microscopy images of the aggregates formed can be observed in panels 24F-G, which seem to present a similar nature to those generated in the absence of the metallophores, although in fewer amounts. Once again, thioflavin-T tests confirm a further reduction in fibrils' development (Figure 25A).

Finally, when an excess (3 eq.) of ligand is present, there is an *a priori* unexpected increase in the media turbidity for both metallophores, in comparison to the samples treated with only 1 eq. of the compounds (dark gray bars in Figure 24A), probably due to precipitation of the uncharged, poorly water soluble bis(hydrazone)copper(II) species, as described recently by our group for the related system Cu²⁺-HPCFur, in the presence of a decapeptide at pH around 7 (Cukierman *et al.*, 2023). In fact, this can also be observed in TEM, through the presence of regions with material accumulation consisting of crystals of the putative neutral [Cu(**X1TMP**)₂] (needle-like) or [Cu(**X1Benz**)₂] (sheet-like) complexes associated with mostly amorphous protein precipitation (panels 24H-I, respectively). Thioflavin-T fluorescence assays (Figure 25B) show a slight fibrillization increase in these samples, close to that observed for the Cu(A β) sample itself.

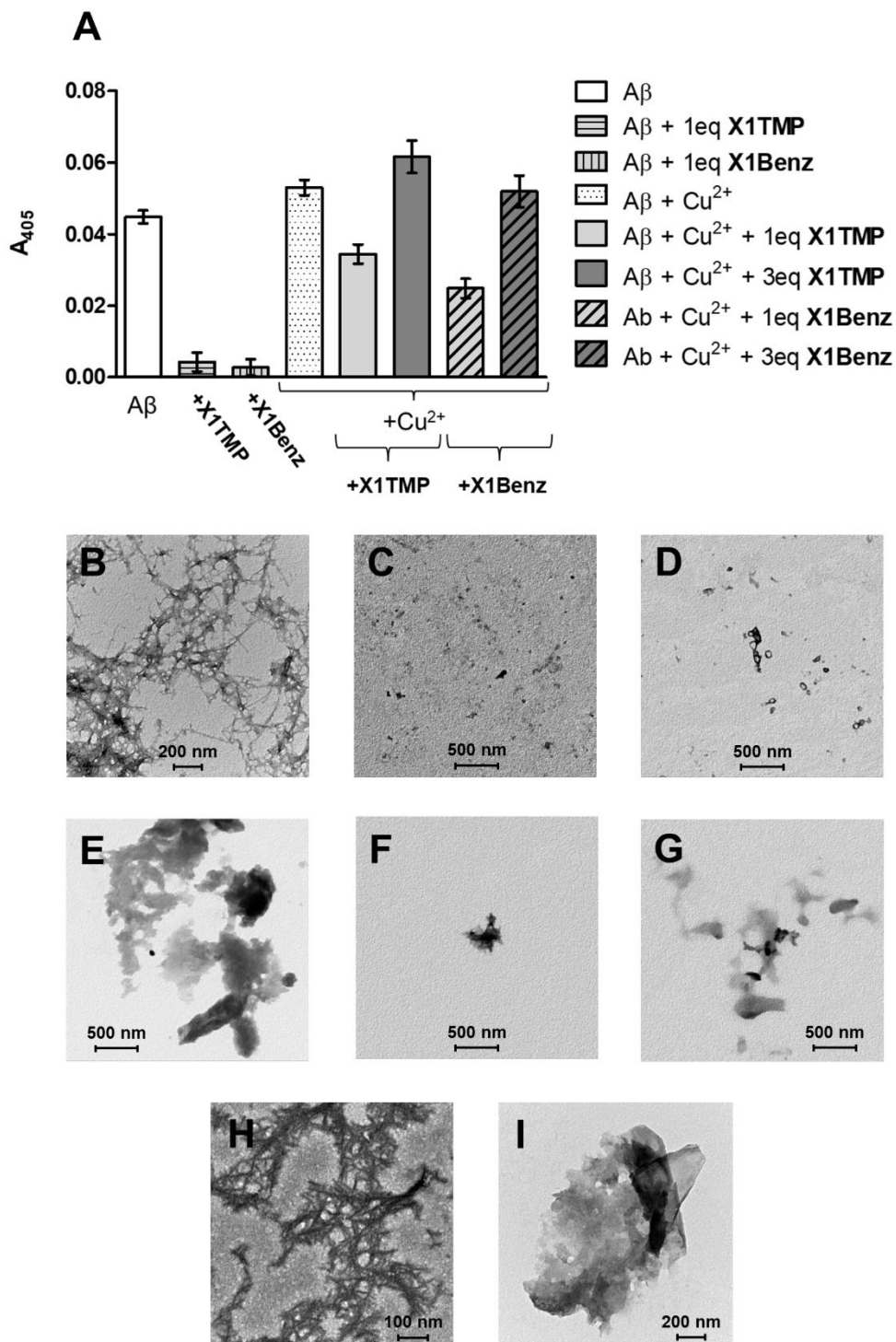


Figure 24. A β_{1-40} aggregation in the absence and presence of copper(II) and the compounds, in HEPES buffer at 20 mmol L⁻¹, containing NaCl 150 mmol L⁻¹, pH 6.6, 37 °C and 1100 rpm after 3 hours. (A) Aggregation as measured by turbidity at 405 nm. Data are reported as mean and standard deviation. (B-I) Transmission Electron Microscopy (TEM) of the different conditions of the assay: (B) A β (C) A β + 1 eq. X1TMP (D) A β + 1 eq. X1Benz (E) A β + Cu²⁺, hereafter referred to as Cu(A β) (F) Cu(A β) + 1 eq. X1TMP (G) Cu(A β) + 1 eq. X1Benz (H) Cu(A β) + 3 eq. X1TMP (I) Cu(A β) + 3 eq. X1Benz.

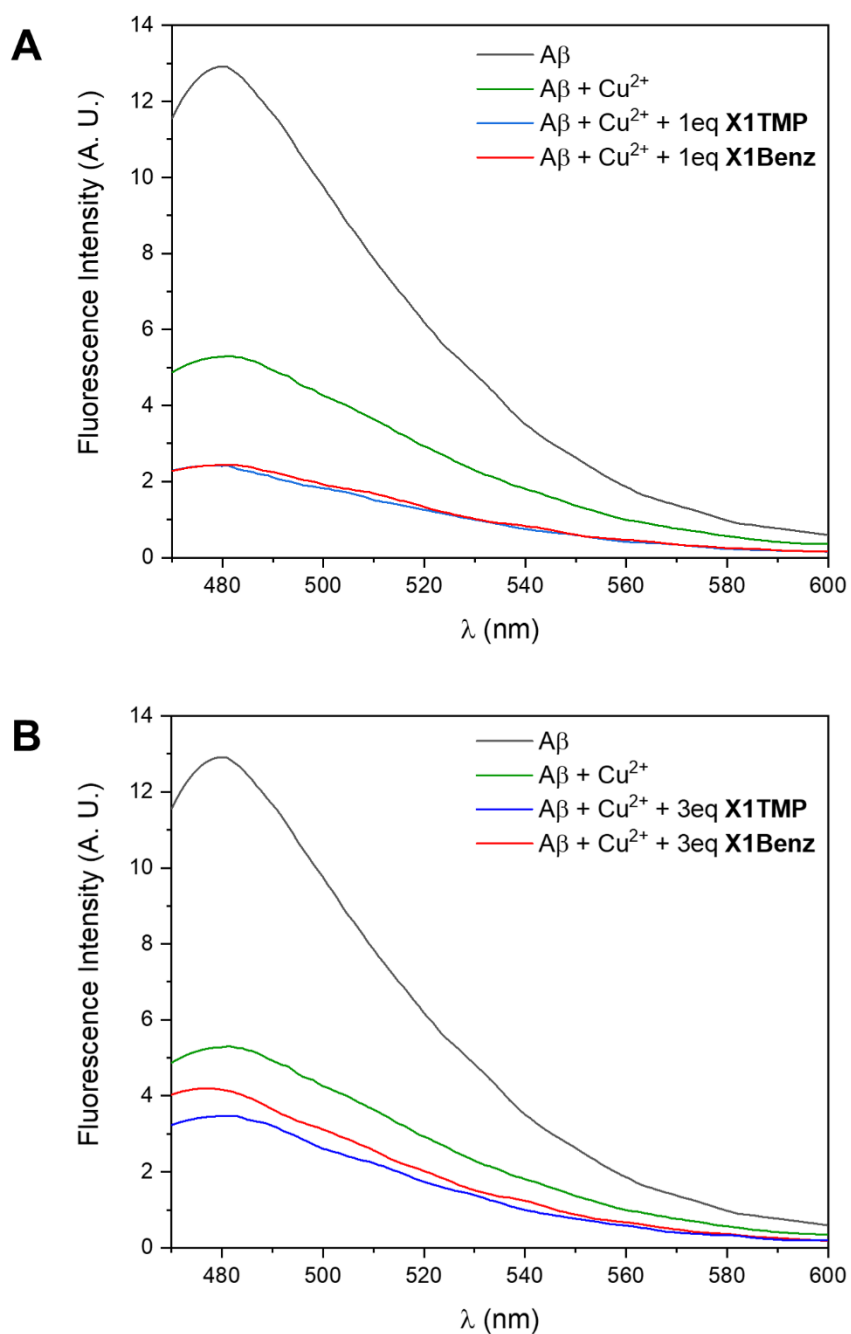


Figure 25. Effect of the synthesized *N*-acylhydrazones on $A\beta_{1-40}$ aggregation in the presence of copper(II) ions in HEPES 20 mmol L⁻¹, NaCl 150 mmol L⁻¹, pH 6.6. Thioflavin-T fluorescence curves after 3 hours incubation at 37 °C and 1100 rpm. **(A)** $A\beta$, $A\beta(Cu)$ and $A\beta(Cu) + 1$ eq. **X1TMP** or **X1Benz**. **(B)** $A\beta$, $A\beta(Cu)$ and $A\beta(Cu) + 3$ eq. **X1TMP** or **X1Benz**.

5.1.7. Mechanistic insights through 1D- and 2D-NMR experiments

As NMR spectroscopy requires higher compound concentrations, experiments were performed only with **X1Benz**, the most water soluble hydrazone.

Since both metallophores seem to impair A β aggregation, even in the absence of copper(II), we decided to investigate this system by firstly analyzing the interactions of **X1Benz** directly with A β ₁₋₄₀, using ¹H-¹⁵N heteronuclear single quantum correlation (HSQC) spectroscopy. The central region of the spectrum of an 80 μ mol L⁻¹ sample of uniformly ¹⁵N-labeled A β is shown in Figure 26A (black contours). Resonances are well resolved and sharp, with a limited dispersion of chemical shifts, reflecting the disordered nature and the high degree of mobility of the backbone. Upon titration with increasing concentration of **X1Benz**, the ¹H-¹⁵N HSQC spectra retained the excellent resolution of the free peptide but presented measurable chemical shift changes in a discrete number of residues distributed throughout its amino acid sequence (Figure 26A -blue/red contours- and 26B). Close analysis of the backbone amide signals exhibiting chemical shift changes upon interaction with **X1Benz** revealed that they correspond to amino acids located in the proximity of aromatic residues, namely: a Phe residue in position 4, a Tyr residue in 10, as well as two Phe residues (positions 19 and 20). Altogether, these results unequivocally demonstrate that **X1Benz** binds to the monomeric form of A β ₁₋₄₀, with aromatic residues possibly playing a very important role as anchoring moieties for binding of this compound to the peptide. It is worth noting that such a behavior was quite unexpected, not observed for other *N*-acylhydrazones previously described by our research group (Cukierman *et al.*, 2018; Hauser-Davis *et al.*, 2015).

Additional experiments are clearly needed to determine if the identified **X1Benz** binding sites at positions F4, Y10, and F19-20 constitute independent, non-interactive motifs, consistent with the binding of at least three **X1Benz** molecules per peptide unit, and to fully characterize the interaction modes and binding strengths.

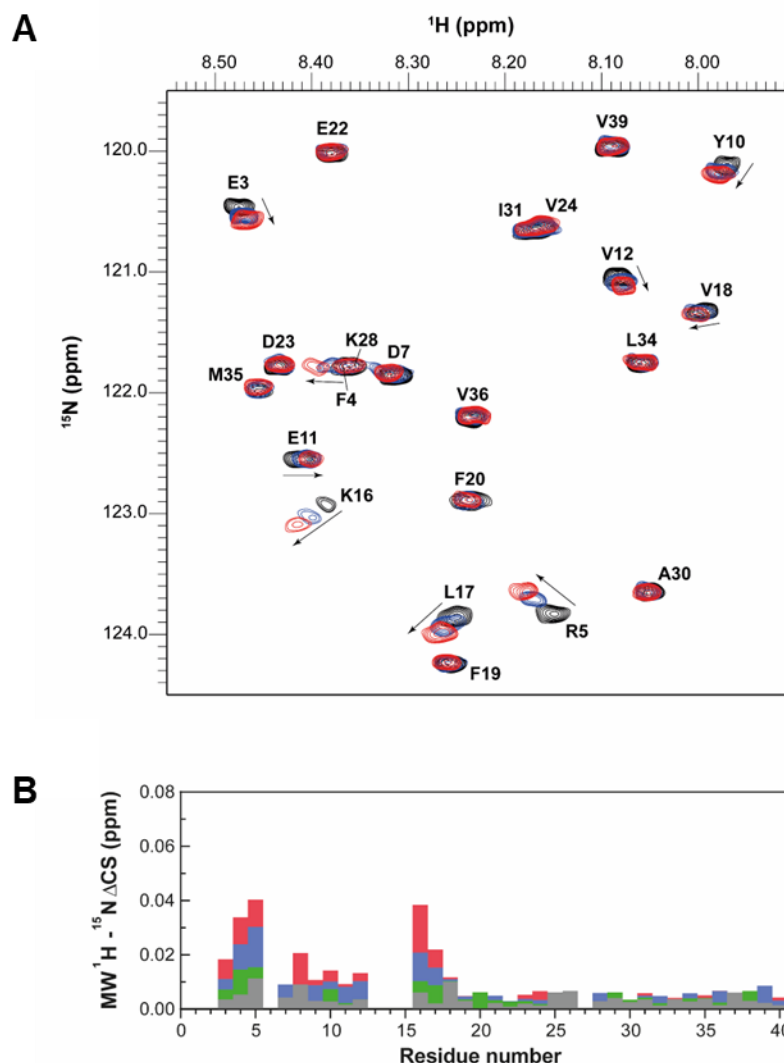


Figure 26. NMR analysis of **X1Benz** binding to $A\beta_{1-40}$. **(A)** Overlaid contour plots of 1H - ^{15}N HSQC spectra of $A\beta$ in the absence (black) and presence of increasing **X1Benz** concentrations: 3 eq. (blue) and 5 eq. (red). Most affected residues are labelled (for the sake of simplicity, the one letter amino acid code was employed). **(B)** Differences in the mean weighted chemical shift ($MW^1H-^{15}N\Delta CS$) displacements between free and **X1Benz**-bound $A\beta$ at molar ratios of 1:1 (gray), 2:1 (green), 3:1 (blue) and 5:1 (red). Experiments were recorded at 15 °C ($80 \mu\text{mol L}^{-1}$ $A\beta$ in Tris 20mmol L^{-1} pH 7.3).

The copper(II) sequestering potential of **X1Benz** towards $A\beta_{1-40}$ was explored at single residue resolution by 1D 1H NMR spectroscopy. As reported earlier (Hauser-Davis *et al.*, 2015), addition up to 1 eq. of Cu^{2+} to $A\beta_{1-40}$ samples caused the severe broadening of specific resonances, clearly indicating their involvement as metal coordinating sites for this physiological ion (Figure 27A and B). Interestingly, increasing amounts of **X1Benz** were not efficient at removing the metal-induced perturbations in $A\beta$ backbone amides, even upon the addition of 5 eq. of the compound (Figure 27C). However, the broadening effects observed

on the signals belonging to **X1Benz** might be an indicative of copper(II) coordination by this compound, probably generating a ternary A β -copper-**X1Benz** species. Such a result is in perfect agreement with previously reported findings by the group regarding the formation of ternary complexes involving *N*-acylhydrazones, Cu²⁺ and small prion protein fragments (Cukierman *et al.*, 2019; Cukierman *et al.*, 2022). In the context of the present work, it seems that this ternary species is the one responsible for impairing ROS production and preventing A β aggregation.

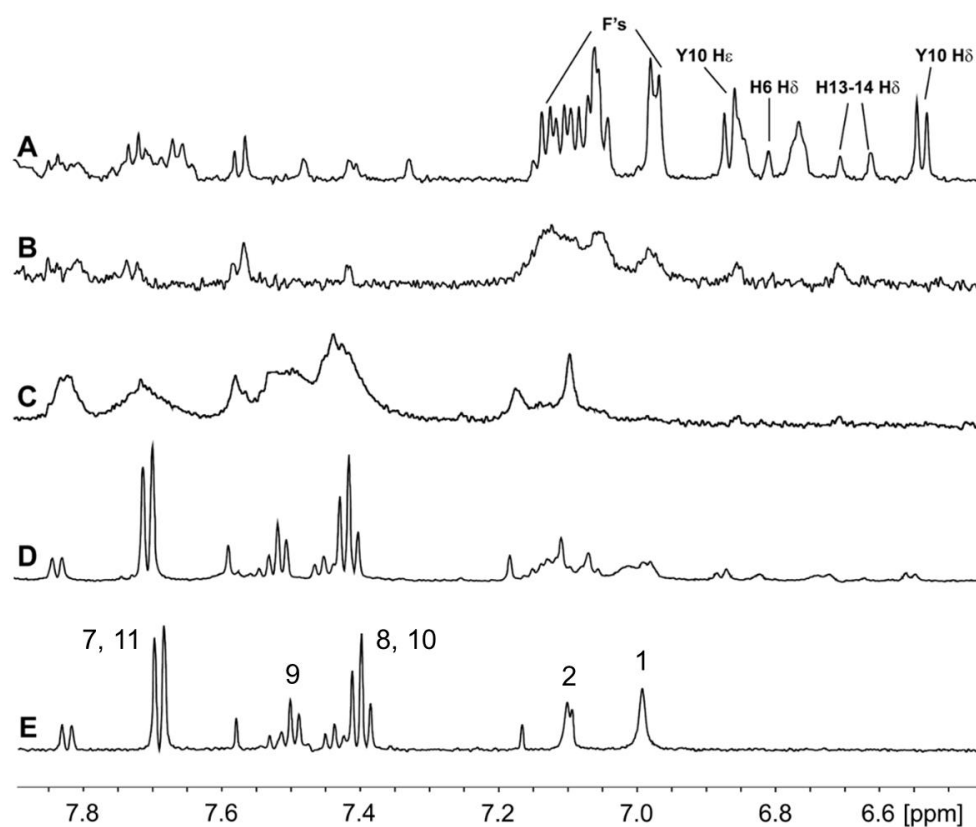


Figure 27. ¹H NMR of the aromatic side chains of A β ₁₋₄₀ in the presence of copper(II) and **X1Benz**. Spectra were registered at 15 °C in Tris buffer 20 mmol L⁻¹ pH 7.3 of samples containing (A) A β (80 μ mol L⁻¹) (B) A β + 1 eq. Cu²⁺ (C) A β + 1 eq. Cu²⁺ + 5 eq. **X1Benz** (D) A β + 1 eq. Cu²⁺ + 5 eq. **X1Benz** followed by addition of 10 mmol L⁻¹ EDTA. Spectral region with the resonances of 400 μ mol L⁻¹ **X1Benz** are shown in (E) along with the signals' assignment. For the sake of simplicity, the one letter amino acid code was employed.

In order to verify the formation of a ternary A β -copper-**X1Benz** complex through a different experimental technique, we obtained UV-Vis spectra of freshly prepared 1:1 (Cu:A β ₁₋₁₆), 1:1 (Cu:**X1Benz**) and 1:1:1 (Cu:A β ₁₋₁₆:**X1Benz**) mixtures in 20 mmol L⁻¹, pH 7.3 Tris buffer solution (Figure 28). While the binary

Cu(A β) species virtually does not absorb light in the studied region, the Cu(**X1Benz**) system showed an overlapped multi-band absorption pattern centered at 360 nm. The ternary A β -copper-**X1Benz** mixture, instead, exhibited a different spectral profile, with the most prominent band centered at 320 nm. Very similar results were obtained by May, Jancsó & Enyedy (May *et al.*, 2021) for a ternary complex involving copper(II), the tetrapeptide DAHK and the thiosemicarbazone Triapine.

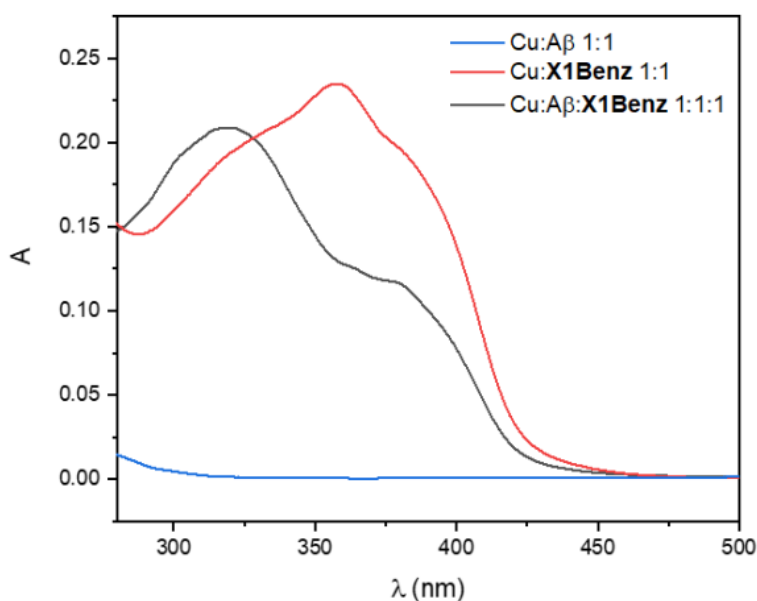


Figure 28. Intra-ligand and CT absorption bands of different equimolar A β_{1-16} , CuCl $_2$ · H $_2$ O and **X1Benz** mixtures in 20 mmol L $^{-1}$ Tris buffer (pH 7.3) at 25 °C. [] = 5 x 10 $^{-5}$ mol L $^{-1}$.

On the other hand, addition of EDTA completely abolishes metal-interactions with both A β and **X1Benz** (Figure 27D). Nevertheless, some signals of the free peptide (Figure 27A) and the hydrazone (Figure 27E) cannot be recovered, especially, in the latter, those related to the imidazole moiety. In fact, the spectrum in Figure 27D is exactly the same obtained for a sample containing only A β + 5 eq. **X1Benz**, suggesting that A β -**X1Benz** interactions are preserved. Thus, the general broadening observed on A β resonances upon addition of EDTA is consistent with the occurrence of a peptide's self-association process, probably mediated by **X1Benz**.

5.2. Part II – Comparison between the (*E*) and (*Z*) isomers of a nicotinic-inspired *N*-acylhydrazone towards the Cu²⁺-bound hIAPP₁₈₋₂₂ fragment in the context of type 2 diabetes *mellitus*

The original goal of the second part of this work was to evaluate the effect of a new *N*-acylhydrazone that was inspired by the structure of nicotine, using a fragment of the human IAPP bound to copper(II) as a model of the endocrine metal-enhanced aggregopathy type-2 diabetes *mellitus*. Nicotine is a naturally occurring alkaloid that is best known for its use as an insecticide and a recreational drug. This exogenous molecule acts as an agonist of many nicotinic acetylcholine receptors found in the central and peripheral nervous system (Fagerström, 2013; Tomizawa & Casida, 2005; Weiland S. *et al.*, 2000). Moreover, pancreatic β -cells also present functional nicotinic receptors, which impact insulin secretion (Eliasson *et al.*, 1996). Therefore, **X1NIC** was designed to present greater biocompatibility and a good pharmacological potential. However, when performing the synthesis of the proposed compound, the ¹H NMR spectrum of the resulting solid revealed the existence of a mixture of geometric stereoisomers, which redirected the study to compare these isomers and how they both interact with the Cu²⁺-hIAPP system.

5.2.1. Syntheses and characterization

When synthesizing **X1NIC** starting from 3.0 mmol of the reagents, although still in the presence of HCl and at reflux for 4 hours, the white solid obtained corresponded to a mixture of two species, evidenced by the existence of two sets of signals in the ¹H NMR spectrum, shown in Figure 29. Two deshielded singlets can be seen for the two hydrazoneic -NH protons, at 12.98 and at 14.84 ppm. The first is in agreement with the usual chemical shift region for the -NH group of hydrochlorides of 1-methylimidazole-containing *N*-acylhydrazones (Cukierman, 2021). The second, in turn, is in consonance with the position of -NH groups involved in intramolecular hydrogen bonding, a feature that was already described by our research group in an *ortho*-pyridine-containing ligand

(Cukierman *et al.*, 2018), but can easily occur with 1-methyl-1H-imidazole-2-carboxaldehyde-derived hydrazones (Figure 30).

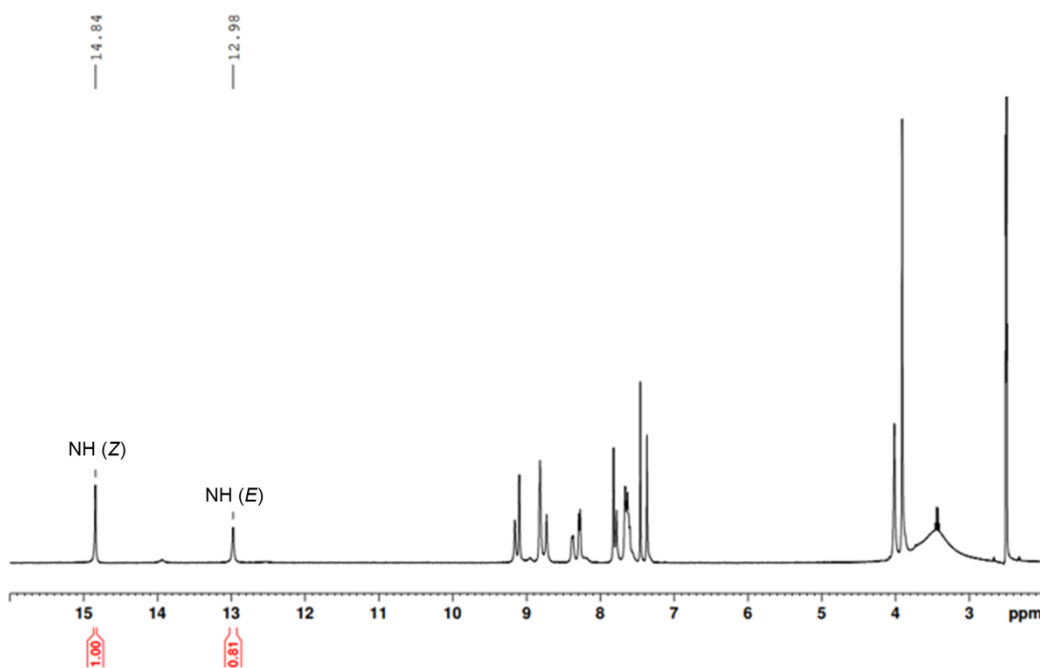


Figure 29. ^1H NMR spectrum (400 MHz) of the **X1NIC** mixture in $\text{DMSO-}d_6$ at 25 °C.

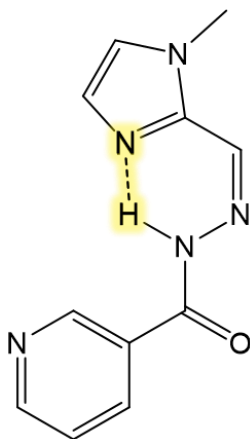


Figure 30. Structural proposal of the (*Z*) isomer of **X1NIC** with an intramolecular H-bond (highlighted in yellow) that probably stabilizes the compound and causes deshielding of the -NH signal in the ^1H NMR spectrum.

The two isomers were then synthesized separately: **X1NIC-(E)** was obtained as a white and elongated solid (60% yield), after reflux for 4 hours in the presence of HCl, while **X1NIC-(Z)** was isolated also as a white, thin solid (30% yield), in the absence of acid and after reflux for 24 hours.

The ^1H NMR spectrum of **X1NIC-(E)** in $\text{DMSO-}d_6$ (Figure 31) shows only one set of signals, indicating the obtention of a pure sample. The characteristic proton resonance of the hydrazonic $-\text{NH}$ group was attributed at 13.19 ppm, a strong indication that the compound is in its hydrochloride form (Cukierman, 2021). The complete signal assignment is summarized in Table 4.

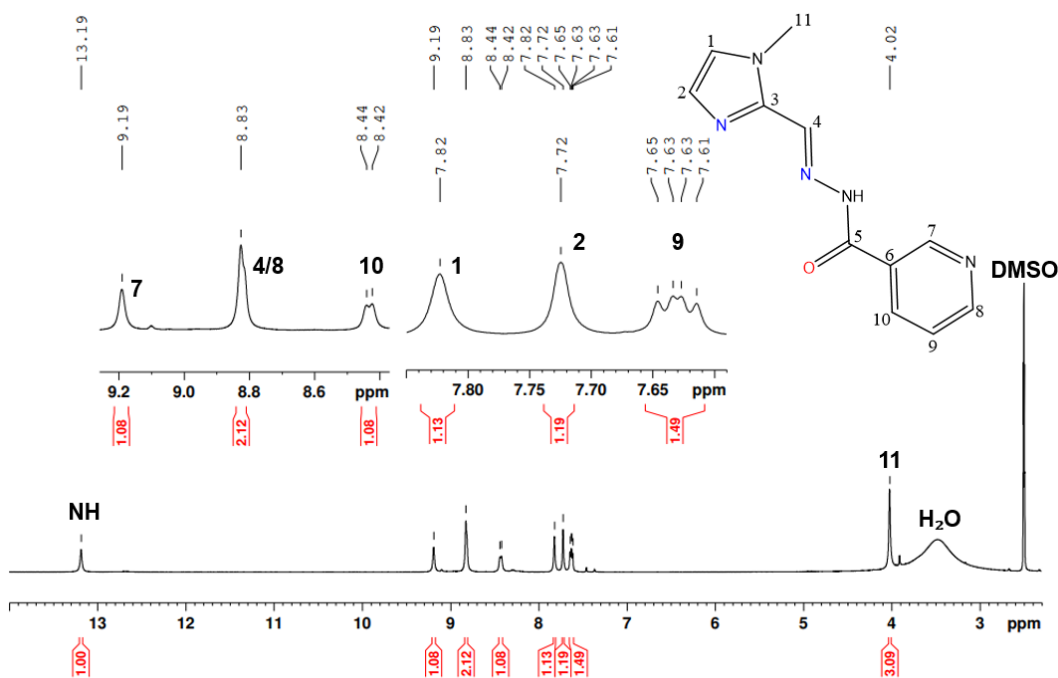


Figure 31. ^1H NMR spectrum (400 MHz) of **X1NIC-(E)** in $\text{DMSO-}d_6$ at 25 °C.

The $^1\text{H-}^1\text{H}$ NOESY experiment (Nuclear Overhauser Effect Spectroscopy) is a powerful tool to identify isomers and determine the conformation of compounds in solution, since it relies on dipolar couplings, *i.e.*, the transfer of magnetization among the spins occurs through space. The 2D spectrum of **X1NIC-(E)** is shown in Figure 32 (top). The $-\text{NH}$ proton showed a correlation with H4, as expected for the (*E*) isomer, but also with H7 and H10, which proves that the compound is present in its *antiperiplanar* conformation, as shown in the bottom part of the figure. Moreover, the interaction between H1 and CH_3 allowed for the unequivocal assignment of the imidazolic signals.

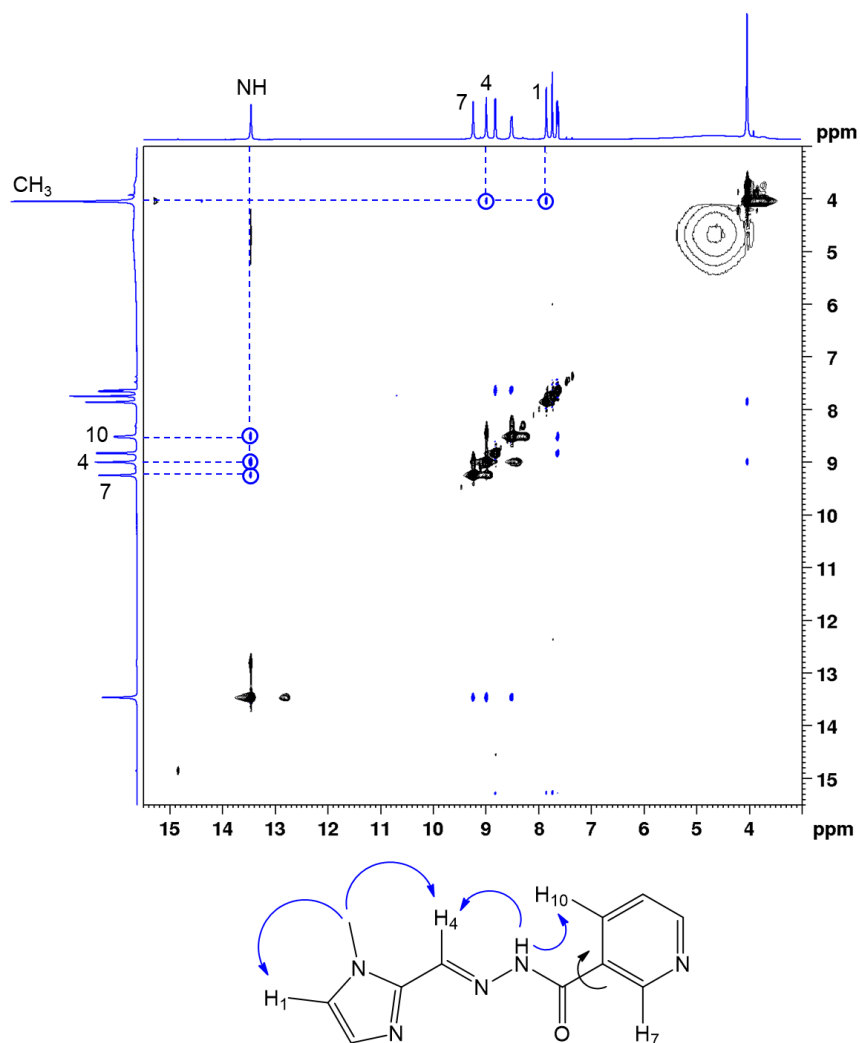


Figure 32. ^1H - ^1H NOESY NMR spectrum (400 MHz) of **X1NIC-(E)** in $\text{DMSO-}d_6$ at 25 °C (top). The proposed structure of the (*E*) isomer in an anti-conformation and its spatial correlations are shown on the bottom. Blue arrows indicate relevant expected dipolar couplings.

The ^1H NMR spectrum of **X1NIC-(Z)**, in turn, shows the highly deshielded (14.84 ppm) -NH signal (Figure 33), indicating that this proton is involved in an intramolecular H-bond with the nitrogen of the imidazole ring, as mentioned before. The chemical shift value of the -NH hydrogen signal observed in our ^1H NMR spectra is similar to those found in the literature, which report that (*E*) isomers of hydrazones usually present δ values for the -NH proton at a higher field than the respective (*Z*) isomers (Cukierman *et al.*, 2018; Palla *et al.*, 1986; Tisovský *et al.*, 2020).

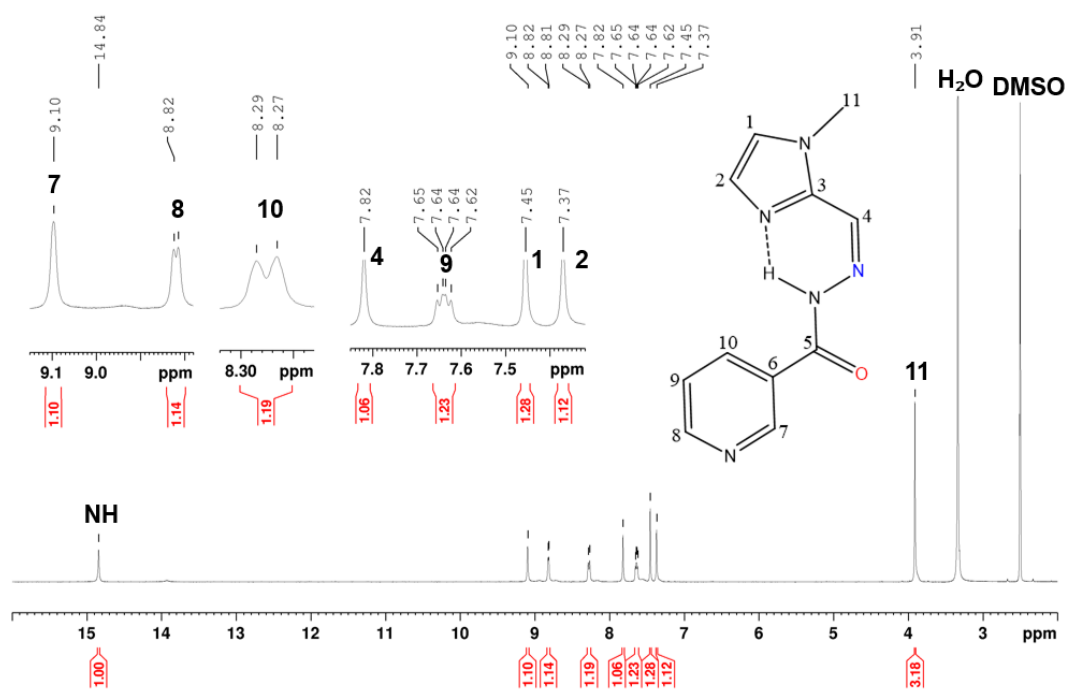


Figure 33. ^1H NMR spectrum (400 MHz) of **X1NIC-(Z)** in $\text{DMSO-}d_6$ at $25\text{ }^\circ\text{C}$.

Once again, we used $^1\text{H-}^1\text{H}$ NOESY (Figure 34) to confirm that the solution was indeed related to the (Z) isomer of **X1NIC**, since the -NH proton only showed correlations with H7 and H10 (due to the rotation of the ring), but not with H4.

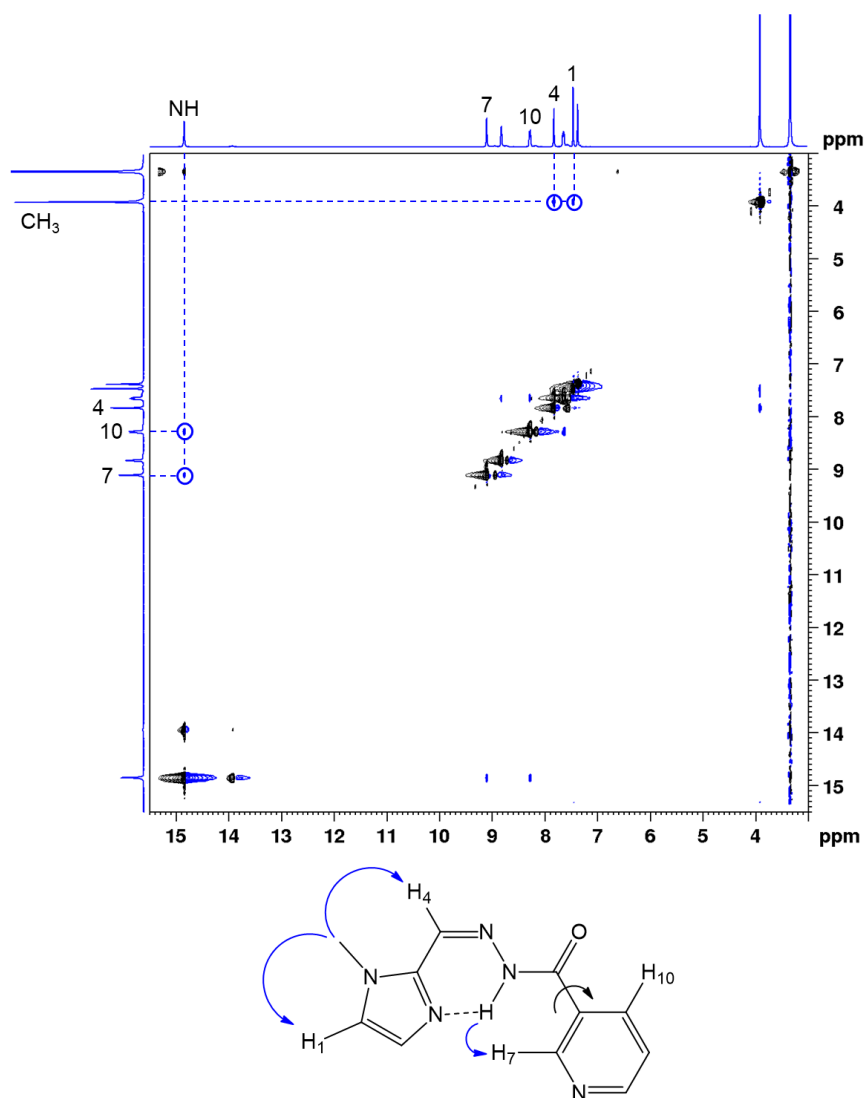


Figure 34. ¹H-¹H NOESY NMR spectrum (400 MHz) of **X1NIC-(Z)** in DMSO-*d*₆ at 25 °C (top). The proposed structure of the (Z) isomer in an anti-conformation and its spatial correlations are shown on the bottom. Blue arrows indicate relevant expected dipolar couplings.

Table 4. ¹H (400 MHz) signal attribution for **X1NIC-(E)** and **X1NIC-(Z)** (DMSO-*d*₆ at 25 °C).

	X1NIC-(E)	X1NIC-(Z)
H	δ (ppm)	δ (ppm)
1	7.82 (s, 1H)	7.45 (s, 1H)
2	7.72 (s, 1H)	7.37 (s, 1H)
4	8.83 (s, 1H)	7.82 (s, 1H)
7	9.19 (s, 1H)	9.10 (s, 1H)
8	8.83 (d, 1H)*	8.82 (d, 1H, ³ J _{HH} = 4.50 Hz)
9	7.63 (dd, 1H ³ J _{HH} = 4.96 Hz, ³ J _{HH} = 7.16 Hz)	7.64 (dd, 1H, ³ J _{HH} = 4.50 Hz, ³ J _{HH} = 7.48 Hz)
10	8.43 (d, 1H, ³ J _{HH} = 7.16 Hz)	8.28 (d, 1H, ³ J _{HH} = 7.48 Hz)
11	4.02 (s, 3H)	3.91 (s, 3H)
NH	13.19 (s, 1H)	14.84 (s, 1H)

Signal multiplicity: (s: singlet; d: doublet; dd: doublet of doublets).
(*): doublet is overlap with H4.

To confirm the hydration state of the compounds, thermogravimetric analyses were conducted. For the (*E*) isomer, an intricate process related to the release of 0.5 hydration water molecules and HCl derived from its hydrochloride condition was observed until 215 °C. After this, organic degradation takes place. Therefore, the proposed chemical formula for this compound is **HX1NIC-(E)⁺Cl⁻** · ½ H₂O (C₁₁H₁₃N₅O_{1.5}Cl, 274.71 g mol⁻¹, M. P. = 164 ± 5 °C). **X1NIC-(Z)**, on the other hand, is completely stable until 210 °C, temperature in which organic degradation begins (C₁₁H₁₁N₅O, 229.24 g mol⁻¹, M. P. = 202 ± 2 °C).

Solid state characterization of both hydrazones was also carried out using mid-infrared spectroscopy, as shown in Figure 35A and B, respectively for **X1NIC-(E)** and (*Z*). The broad bands observed at high frequencies in both spectra are probably related to humidity in the highly hygroscopic KBr pellets. Nevertheless, the band in the spectrum of **X1NIC-(E)** is clearly more intense, and this can be due to the presence of hydration water in this isomer, which spectrum also shows a band at 3185 cm⁻¹ assigned to ν(N⁺-H) of the protonated imidazole

ring. The hydrazone amide $\nu(\text{N-H})$ mode of both compounds absorb at 3150 and 3128 cm^{-1} , respectively for **X1NIC-(E)** and **X1NIC-(Z)**. This downshift is expected for the latter due to the intramolecular H-bond, which weakens the N-H linkage. Table 5 shows the main absorptions and assignments for both isomers.

Table 5. Selected infrared frequencies of the *N*-acylhydrazones **X1NIC-(E)** and **X1NIC-(Z)**, along with their assignments. Samples were prepared as KBr pellets.

Assignment	X1NIC-(E)	X1NIC-(Z)
	IR (cm^{-1})	IR (cm^{-1})
$\nu(\text{N}^+-\text{H})_{\text{imidazole}}$	3185	-
$\nu(\text{N-H})_{\text{hydrazone}}$	3150	3128
$\nu(\text{C=O})_{\text{amide}}$	1696	1685
$\nu(\text{C=N})_{\text{azomethine}}$	1621	1640
$\nu(\text{N-N})$	1100	1093

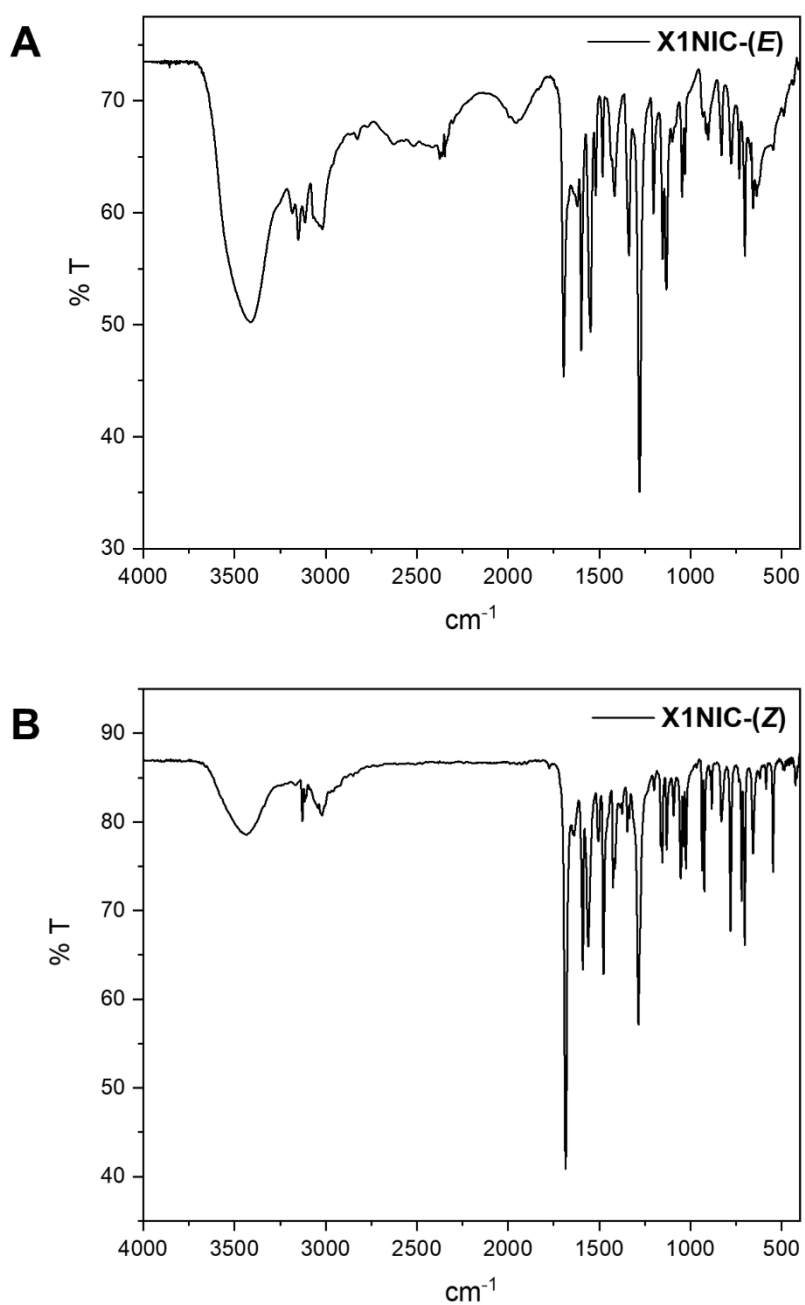


Figure 35. Mid-infrared spectra of (A) X1NIC-(E) and (B) X1NIC-(Z). Samples were prepared as KBr pellets.

5.2.2. Stability towards hydrolysis in buffered solution

Although our experience has shown that 1-methylimidazole-containing *N*-acylhydrazones are highly stable in aqueous solutions (Cukierman, 2021), it is important to individually assess each synthesized hydrazone to confirm such

properties. Thus, we evaluated the stability of the **X1NIC-(E)** and **X1NIC-(Z)** ligands towards hydrolysis in a 1% DMSO/Tris pH 7.4 medium, at a hydrazone concentration of $5 \times 10^{-5} \text{ mol L}^{-1}$.

Only one, intense band, centered at 316 nm, was observed in the UV-Vis spectrum of **X1NIC-(E)**, which can be seen in Figure 36 along with the absorptions of the precursor aldehyde and hydrazide. Absolutely no change was observed in the absorbance of the spectra taken over 12 hours, demonstrating the high stability of the evaluated hydrazone.

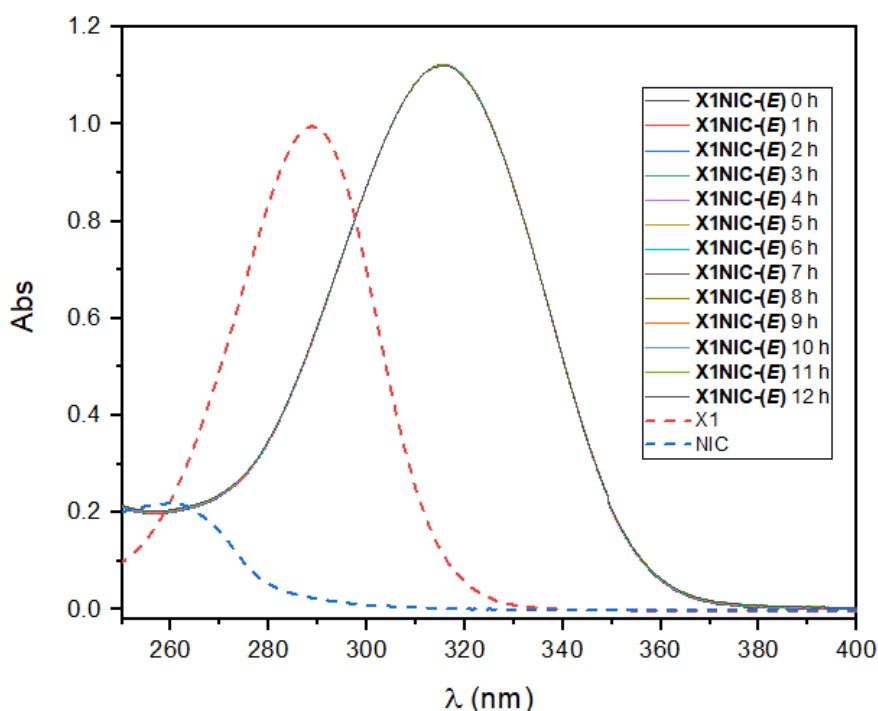


Figure 36. UV-Vis absorption spectra of **X1NIC-(E)** and its precursors ($5 \times 10^{-5} \text{ mol L}^{-1}$) in 1% DMSO/Tris (10 mmol L^{-1} , pH 7.4), obtained over a period of 12 h, at room temperature.

Similarly to **X1NIC-(E)**, the (Z) isomer of the nicotine-inspired hydrazone possesses only one intense absorption band centered at 319 nm (Figure 37). Although slightly less stable (small increase in the precursor-related band at around 265 nm), **X1NIC-(Z)** is still extremely resistant towards hydrolysis, as shown in the spectra acquired over time.

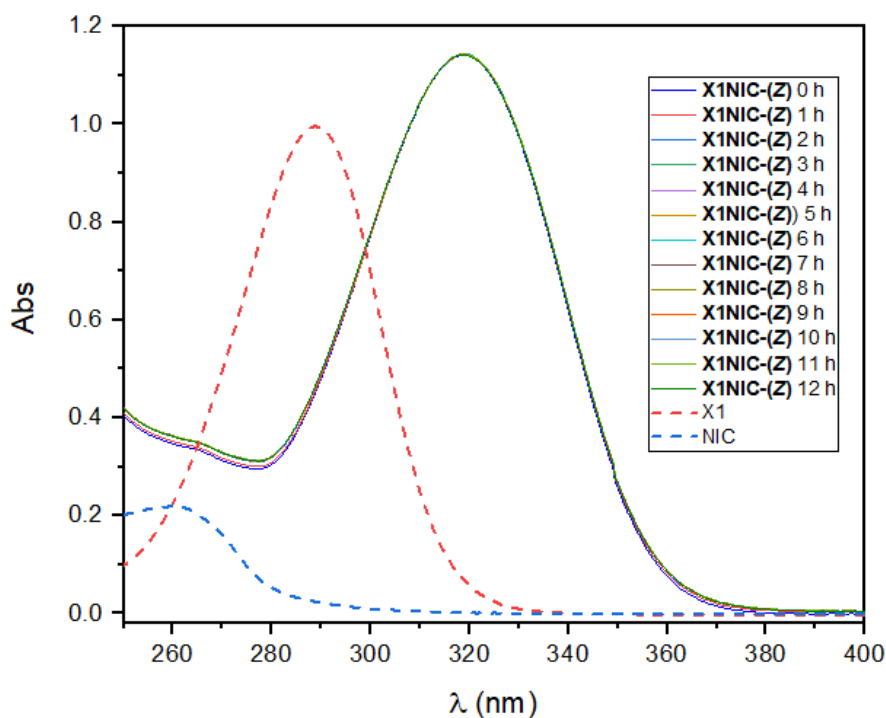


Figure 37. UV-Vis absorption spectra of **X1NIC-(Z)** and its precursors ($5 \times 10^{-5} \text{ mol L}^{-1}$) in 1% DMSO/Tris (10 mmol L^{-1} , pH 7.4), obtained over a period of 12 h, at room temperature.

5.2.3. Thermal stability of the isomers in solution

^1H NMR spectroscopy is a powerful tool widely employed in the assessment of isomerization of compounds in solution. With this technique, we conducted a study to examine the conversion of **X1NIC** isomers as a function of temperature. An initial measurement was performed at $25 \text{ }^\circ\text{C}$ (orange spectra in Figure 38 and Figure 39). Then, spectra were acquired every $10 \text{ }^\circ\text{C}$ increase (yellow, purple and dark green spectra), until $65 \text{ }^\circ\text{C}$ (blue), which is the limit of the spectrometer. Finally, temperature was reduced back to $25 \text{ }^\circ\text{C}$ and a final spectrum (shown in red in both figures) was registered.

We first analyzed the stability of **X1NIC-(E)**, which can be seen in Figure 38. The figure also shows the spectrum of **X1NIC-(Z)** at the initial temperature in light green, for comparison purposes. From $45 \text{ }^\circ\text{C}$ on, the appearance of signals related to the (Z) isomer can be seen. In Figure 38A, for example, which shows the spectral window of 2.0-5.0 ppm, the resonance of H11 (imidazolic methyl) of the (Z) isomer appears at 3.91 ppm, at a proportion of around 11%. In the aromatic range of the spectra (Figure 38B), all signals can also be observed, especially with increasing temperature. It is worth mentioning that the NH signal

of the (*Z*) isomer (14.84 ppm), only appears when the sample is cooled back to 25 °C (Figure 38C), due to fast exchange with the solvent. At 65 °C, the average proportion of the species in solution is 84% (*E*) and 16% (*Z*). When the temperature is brought back to 25 °C, the (*Z*) isomer that was formed during the assay is still present (18%), and the final solution corresponds to a mixture of both stereoisomers, dominated by **X1NIC-(*E*)**.

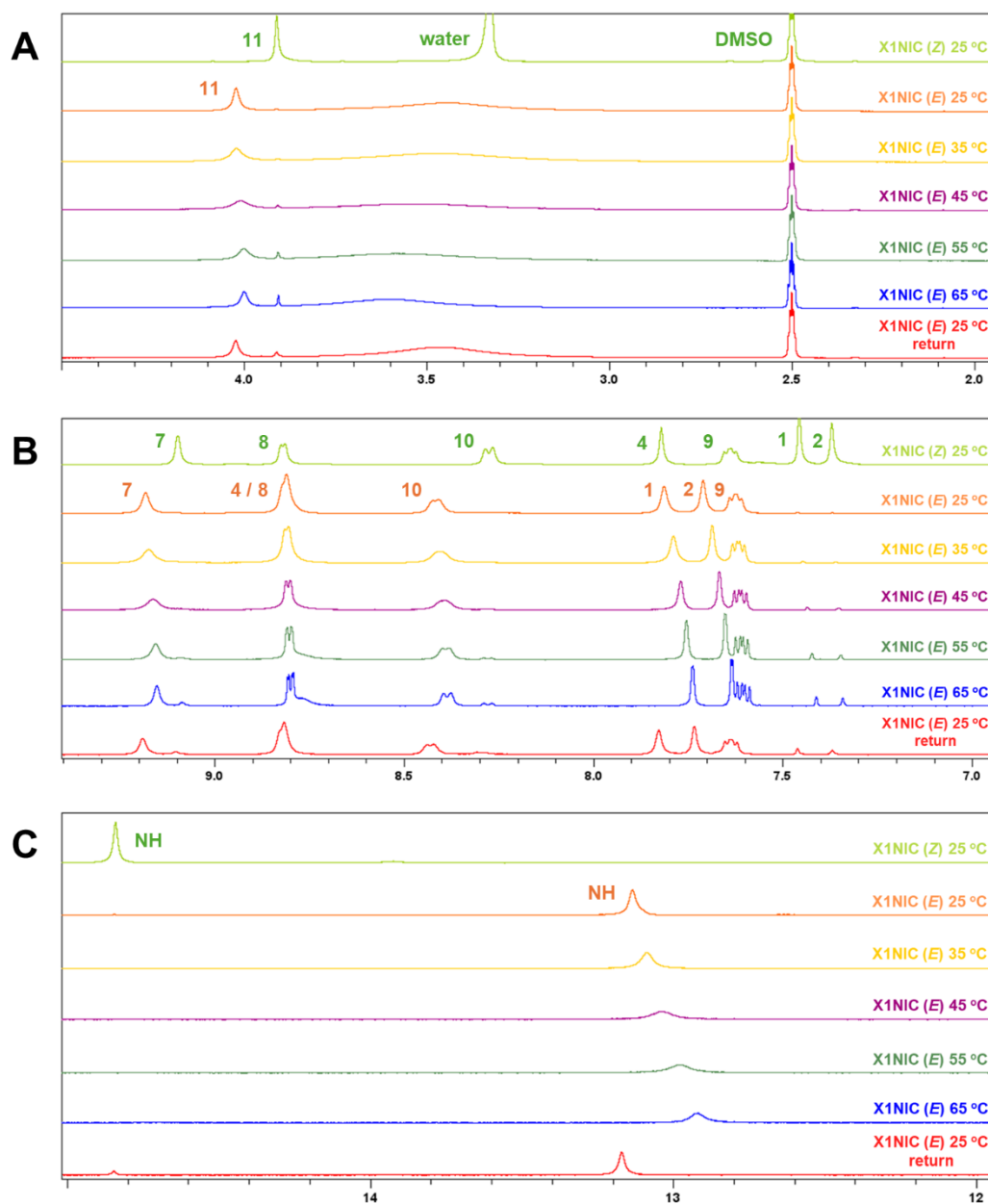


Figure 38. Thermal stability analysis of **X1NIC-(*E*)** assessed by ^1H NMR, with spectra taken every 10 °C, from 25 to 65 °C. A final spectrum was collected after cooling the sample back to room temperature (25 °C). Selected spectral windows: (A) 2.0 – 5.0 ppm; (B) 7.0 – 9.5 ppm; (C) 12.0 – 15.0 ppm.

X1NIC-(Z), on the other hand, does not seem to undergo thermally induced isomerization (Figure 39), which indicates that this is probably the thermodynamically favored product. One possible contributing factor to this stability, although certainly not the only one, may be the presence of the strong intramolecular H-bond in the (Z) isomeric form of **X1NIC**.

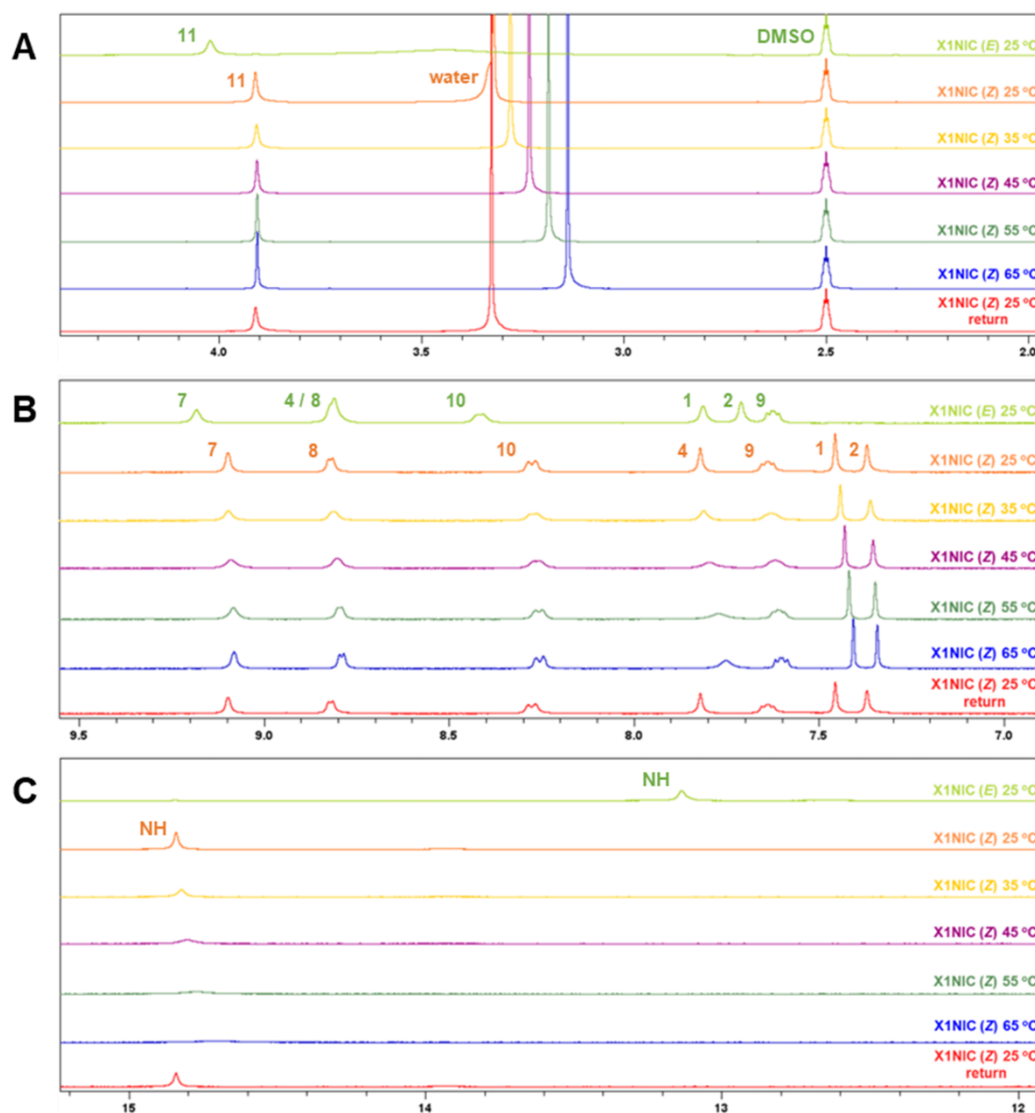


Figure 39. Thermal stability analysis of **X1NIC-(Z)** assessed by ^1H NMR, with spectra taken every $10\text{ }^\circ\text{C}$, from 25 to $65\text{ }^\circ\text{C}$. A final spectrum was collected after cooling the sample back to room temperature ($25\text{ }^\circ\text{C}$). Selected spectral windows: (A) $2.0 - 5.0$ ppm; (B) $7.0 - 9.5$ ppm; (C) $12.0 - 15.0$ ppm.

5.2.4. Pharmacological parameters

The Osiris Property Explorer: DataWarrior™ software was employed as a tool for the *in silico* predictions of some properties considered important for the design and development of new commercial drugs (Lipinski *et al.*, 2001). However, since the stereochemistry and atom connectivity are not considered in these calculations, the same values were obtained for both isomers, which are summarized in Table 6.

Table 6. Calculated (OSIRIS Property Explorer: DataWarrior™) descriptors of pharmacological relevance for **X1NIC**. MW: molecular weight, cLog P: calculated partition coefficient, cLog S: calculated water solubility, PSA: polar surface area.

	MW (g mol ⁻¹)	cLog P	cLog S	PSA (Å ²)	Druglikeness	DrugScore
X1NIC	229.00	0.38	-0.69	72.17	7.01	97%

The first verified property was the molecular weight of the compound, for which a smaller value represents an easier passage through cellular membranes. According to Lipinski's rule of five, **X1NIC** is in the ideal range (MW ≤ 500 g mol⁻¹). Then, log P is calculated, which is related to the hydrophilic-lipophilic balance of the molecule. In this context, the compound should be neither too hydrophilic or nor too lipophilic, as this can hinder its ability to penetrate the lipid bilayers and thus be absorbed by the body. Although Lipinski's original suggestion regarding log P values is that it stays below 5, new guidelines regarding the specific passage of a compound through the blood-brain barrier state that the values should be between 0 and 3 (Pajouhesh & Lenz, 2005). Log S, in turn, refers to the aqueous solubility of a compound which, together with the log P value, makes the analysis of cell permeability more complete and reliable. Regarding these two parameters, **X1NIC** is in consonance with the current guidelines, presenting good water solubility that allows it to be studied in pseudo-physiological media, but still some lipophilicity that will, most likely, facilitate its cellular penetration.

The polar surface area (PSA) is a parameter commonly used for evaluating the degree of polarity of a molecule and, for drugs targeting the central nervous system, PSA should be less than 90 Å² according to Van de Waterbeemd *et al.* (1998).

Additionally, a good *in silico* pharmacological analysis of a drug candidate usually considers the Druglikeness parameter, in which fragments belonging to a database of traded drugs and commercially available compounds is used to compare the structure of the molecule in question, to determine similarities. A positive value in Druglikeness, such as the one calculated for **X1NIC**, means that the studied compound contains mainly fragments which are usually seen in commercial drugs. However, it is important to note that it does not necessarily mean that these fragments are well balanced concerning other properties.

Finally, the DrugScore parameter combines all the previous values and includes an evaluation of the toxicity risks of the analyzed compound, resulting in a percentage merit that can be used to judge the candidate's overall potential to be developed as a drug. **X1NIC** had an estimated DrugScore of 97%, since it did not show any signs of possible mutagenic, tumorigenic, irritant, or reproductive effects.

Regarding the log P parameter, we also determined the experimental values for both hydrazones, using Tris buffer pH 7.4 as the aqueous phase and 1-octanol as the organic phase. It is important to note that these compounds are expected to be neutral in the selected (physiological) pH: the pKa of the 1-methylimidazole nitrogen, which is protonated in the solid state of **X1NIC-(E)**, is 5.3 in this type of hydrazones (Cukierman *et al.*, 2022), while that for the nicotinic nitrogen it is around 4.4 (Benković *et al.*, 2016), which means that both of these atoms are deprotonated, and therefore neutral, at pH 7.4. Moreover, the pKa of the amide nitrogen of 1-methylimidazolic *N*-acylhydrazones is above 9.5 (Cukierman *et al.*, 2022), thus being in the non-ionic, protonated form at the evaluated medium.

The values obtained for the (*E*) and the (*Z*) isomers were 0.62 ± 0.01 and 0.87 ± 0.02 , respectively. Both are in the optimal range considered for the blood-brain barrier crossing (0-3). Interestingly, **X1NIC-(Z)** is slightly more lipophilic than **X1NIC-(E)**, a fact that was also experimentally observed when comparing the water solubility of the compounds. The presence of an intramolecular hydrogen bond can, in fact, cause an increase in the apparent lipophilicity of the molecule (Ashwood *et al.*, 2001; Emami *et al.*, 2021). Nevertheless, both compounds still present good water solubility and a great hydrophilic-lipophilic balance.

5.2.5. Interactions of both isomers with copper(II) ions in solution

The interactions of each ligand with copper(II) were initially studied using the Job method, monitored through UV-Vis. Representative electronic spectra of the mixtures from 0.5 to 1.0 hydrazone molar fraction (Figure 40A and B) show the intra-ligand absorbance [315 nm for **X1NIC-(E)** and 319 nm for **X1NIC-(Z)**] that undergo bathochromic shifts upon complexation. Interestingly, this change is much more significant for the (*E*) isomer (372 nm) than for the (*Z*) compound (332 nm). Nevertheless, a Job plot (absorbance *versus* molar fraction) was constructed for both hydrazones at a wavelength in which only the complex absorbs [372 nm for **X1NIC-(E)** and 380 nm for **X1NIC-(Z)**], as shown in the *insets* of Figure 40. The maximum absorbance achieved by the complexes of both isomers was at the 0.5 molar fraction, which indicates that the complex with ML stoichiometry is the most stable. It is important to highlight that no copper(II) characteristic *d-d* band was observed due to the low concentration employed in this assay.

Although this method does not provide an absolute value for the stability constant of the complexes, a comparison between similar compounds that were evaluated under the same experimental conditions can be performed, with the calculation of an apparent constant value, K_{app} . Thus, the apparent affinity constants for complex formation between the studied *N*-acylhydrazones and copper(II) were estimated from their Job plots. **X1NIC-(E)** presented a $\log K_{app}$ of 5.82 ± 0.16 , while **X1NIC-(Z)** presented a lower $\log K_{app}$ value, equal to 5.04 ± 0.04 , both calculated from triplicates of the experiments. The higher value obtained for the (*E*) isomer is in perfect agreement with the fact that this compound can act as a tridentate ligand, while **X1NIC-(Z)** may only coordinate the copper(II) ions in a bidentate manner.

Moreover, these values can readily be compared to other structure-related 1-methylimidazole-containing *N*-acylhydrazones previously reported by our research group, or even synthesized in the first part of this work. For example, the mescaline-inspired **X1TMP** showed an apparent $\log K$ of 5.74 ± 0.15 , while its unsubstituted analogue **X1Benz** presented a slightly higher $\log K_{app}$ value, equal to 5.87 ± 0.11 , both in the same range of the tridentate **X1NIC-(E)**.

An interesting comparison is that with X1INH (structure shown in Figure 13), which has a K_{app} value of 5.66 ± 0.08 , calculated under similar conditions. This compound is a positional isomer of the studied nicotine-inspired hydrazone and has a proven capacity to affect the aggregation state of an amyloidogenic protein in a cellular model of parkinsonism. Additionally, the ligand had its metallophoric activity demonstrated for both Cu^{2+} and Cu^+ ions, by high field NMR spectroscopy (Cukierman *et al.*, 2020). Thus, one can conclude that, since the herein studied hydrazones, especially **X1NIC-(E)**, present a similar formation constant towards copper(II) ions as those of other ligands with indubitably metallophoric potential, these too might be promising MPACs, and certainly deserve further investigation in this sense.

It is worth noting that a moderate affinity is desired for these compounds, since the metallophore is expected to remove the metal from the amyloidogenic protein, but also to redistribute it throughout the affected organ or region, instead of completely eliminating it from the body as a strong chelator would, thus reducing the deleterious effects of metal dyshomeostasis.

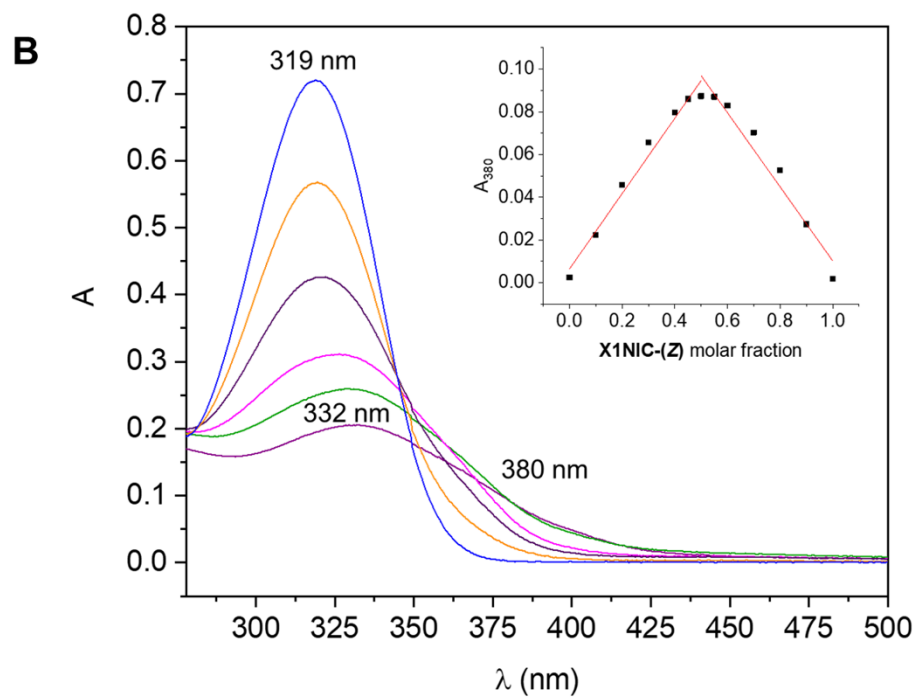
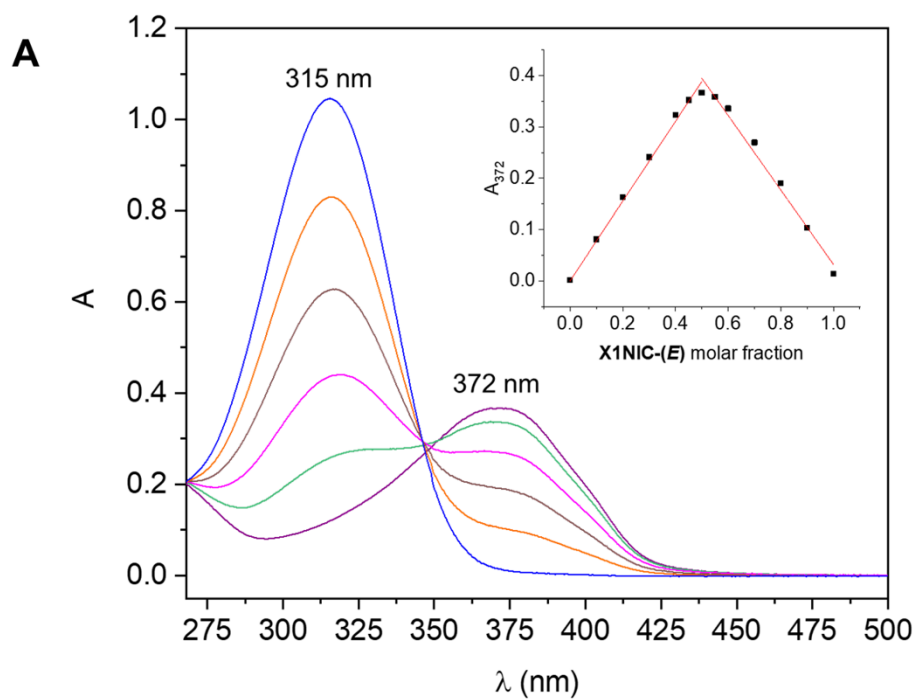


Figure 40. Method of continuous variations to evaluate the copper(II) binding affinity of the two isomers of X1NIC: (A) X1NIC-(E) and (B) X1NIC-(Z). Representative electronic spectra of ligand molar fractions from 0.5 to 1.0. *Insets:* absorbance versus molar fraction plots. Conditions: HEPES buffer (50 mmol L⁻¹, pH 7.4), 25 °C.

To further understand the coordination modes of these ligands towards copper(II), we performed a ^1H NMR analysis on a solution containing a mixture of both isomers at a 1:1 ratio, followed by the addition of 0.05 eq. CuCl_2 . Only a substoichiometric amount of the paramagnetic metal ion was added in order to avoid excessive broadening of the signals. Nevertheless, the presence of only 0.05 eq. of copper(II) caused the disappearance of practically all the (*E*) ligand signals (Figure 41). The remaining identified signals are marked in red in the figure, while proton attribution of the mixture prior to copper addition can be seen in orange for **X1NIC-(E)** and green for **X1NIC-(Z)**. The signals related to the imidazole hydrogen atoms (H1 and H2) of the (*E*) isomer, as well as its methyl protons (H11), are completely broadened, suggesting that this ring constitutes an anchoring site for copper(II) ions in this compound. The same signals, however, are not much affected in **X1NIC-(Z)**, confirming the bidentate nature of this latter ligand, and suggesting that the intramolecular hydrogen bond is maintained in this solution. In both cases, azomethine hydrogen (H4) and amide -NH signals are also broadened upon metal addition, due to the N,O-coordination mode of the hydrazonic moiety.

Interestingly, the signals related to the pyridine ring are also affected by the presence of copper, suggesting a possible contact through this monodentate site. In fact, the $\text{HC}=\text{N}-\text{NH}-\text{CO}-$ group is an efficient electron withdrawing group, affecting the *ortho* and *para* positions of the hydrazide-derived ring. Thus, the nitrogen of the *m*-pyridine ring (derived from nicotinic acid hydrazide) is more basic than that of the *p*-pyridine (derived from isonicotinic acid hydrazide – or isoniazid), which explains why this effect was observed for **X1NIC**.

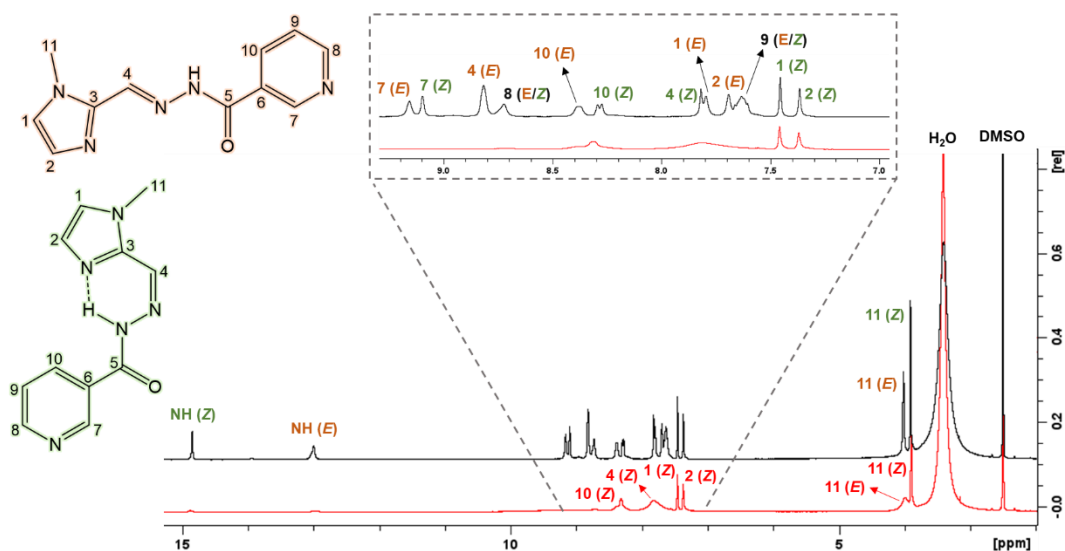


Figure 41. Simultaneous **X1NIC-(E)/X1NIC-(Z)**–copper(II) interactions studied through ^1H NMR (400 MHz) spectroscopy, at 25 °C. Black: Mixture of both **X1NIC** isomers at *E/Z* ratio 1:1, in $\text{DMSO-}d_6$. Red: Same mixture after addition of 0.05 eq. copper(II) resulting in a solution of $\text{DMSO-}d_6$ containing 1% D_2O .

5.2.6. Interactions of **X1NIC** isomers with the Cu^{2+} –hIAPP₁₈₋₂₂ system through high-field NMR

The use of protein or peptide fragments is a valid approach to study different aspects of such intricate systems and has been especially helpful in deciphering the coordinating features of amyloidogenic proteins and peptides towards endogenous metal ions such as copper(II) and zinc(II) (Sóvágó *et al.*, 2023). It allows us, for example, to study these proteins at higher concentrations without the concerns related to their aggregation. In the case of diabetes-related amylin, the hIAPP₁₈₋₂₂ fragment has been proposed as the coordinating portion of the peptide (Rivillas-Acevedo *et al.*, 2015; Sánchez-López *et al.*, 2016), and was employed in our studies of the interactions involving both **X1NIC** isomers with the copper(II)-peptide system. The chemical structure of the amino acid sequence of this fragment (HSSNN) can be seen below in the schematic Figure 42.

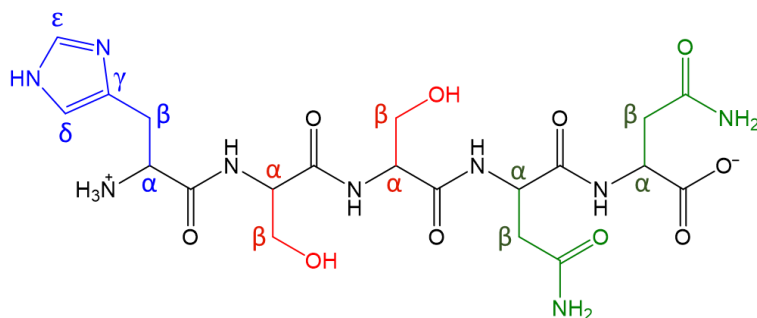


Figure 42. Structure of the hIAPP₁₈₋₂₂ peptide fragment (HSSNN) employed in this work. Side chains are marked in blue for H (histidine), red for S (serine) and green for N (asparagine).

First, we evaluated the interactions of hIAPP₁₈₋₂₂ with copper(II) ions through ¹H NMR spectroscopy using a high-field spectrometer (700 MHz). The spectrum of the free peptide is shown in Figure 43A. The signals related to histidine (H18) were assigned as a triplet at 4.00 ppm (H_α), a multiplet between 3.08 and 3.02 ppm (H_β) and two singlets at 7.01 and 7.80 ppm, associated with the δ and ε hydrogens of the imidazole ring, respectively. Regarding the two serine residues (S19/S20), their H_α signal compose a multiplet at 4.36 – 4.45 ppm, while the H_β signal was attributed as another multiplet at 3.76 – 3.83 ppm. The -OH group was identified through a singlet at 8.51 ppm. Finally, the amide -NH₂ protons from the side chain of the two asparagine residues (N21/N22) were observed at 7.92 and 8.39 ppm. The signals related to H_α and H_β of these residues were attributed as multiplets at 4.36-4.45 ppm and 2.55-2.78 ppm respectively. However, the proximity of the irradiation site to the hydrogen nuclei for water suppression affects the H_α signals of the serine and asparagine residues (S19/S20 and N21/N22), making them less intense and therefore difficult to observe.

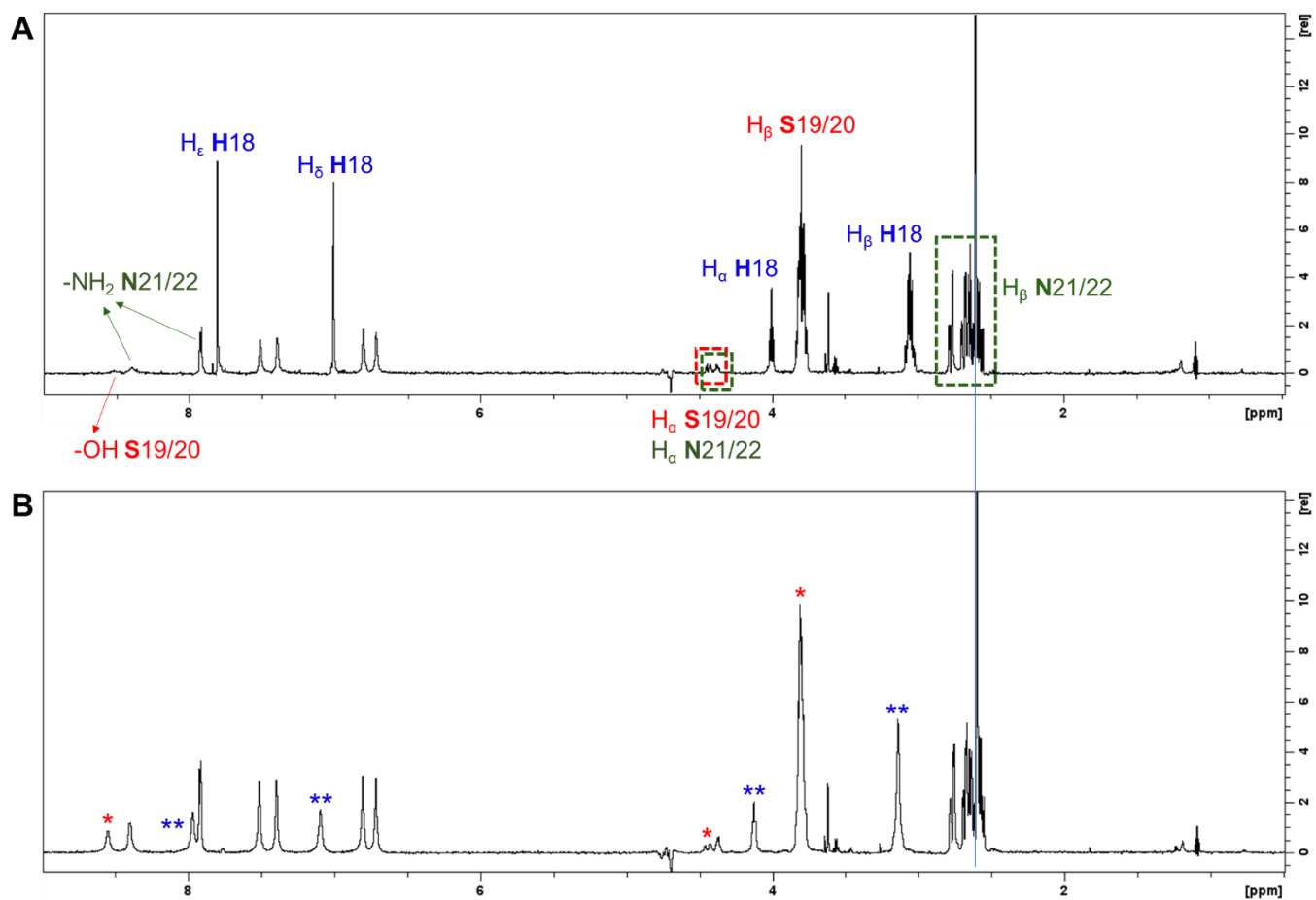


Figure 43. ^1H NMR spectra (700 MHz) of (A) pure hIAPP₁₈₋₂₂ and (B) hIAPP₁₈₋₂₂ + 0.1 eq. Cu^{2+} , both acquired at 25 °C. Samples were prepared in 20 mmol L^{-1} Tris- d_{11} at pH 7.4, with 8.5% D_2O and 4% $\text{DMSO-}d_6$. Histidine residues are highlighted in blue, while red was used for serine and green for asparagine. (**) indicates the most affected signals upon copper(II) addition, while (*) is showing signals moderately modified in this context.

Figure 43B shows the ^1H NMR spectrum of this peptide after the addition of 0.1 eq. of copper(II). Once again, substoichiometric amounts of the metal were employed. As expected, the most affected signals (represented by ** in the figure) were those of H18, confirming that this is the main anchoring site for the metal ion. This preference of copper(II) towards histidine is consistent with the prediction by Pearson's classification, in which histidine and Cu^{2+} are considered borderline base and acid, respectively. All hydrogen atoms of this residue are affected, especially those from the aromatic ring (H δ and H ϵ), which are directly related to the metal coordination site. A decrease in signal intensity can be observed, in addition to their broadening, due to the paramagnetic relaxation enhancement effect of copper(II). Serine-related signals are also affected, although to a lesser extent (marked with * in the figure), which lead us to propose an equatorial N_3O coordination mode similar to that reported by Rivillas-Acevedo *et al.* (2015). Sánchez-López *et al.* (2016) demonstrated through spectroscopic analyzes and theoretical studies using models of the Cu^{2+} -hIAPP $_{18-22}$ complex that coordination through the -OH is more favorable than through the carbonyl group of S20. This is explained by the fact that the first binding is stronger, with a bond distance to copper(II) of 2.12 Å, while the latter is weaker and distorted, with a bond distance of 2.40 Å. Finally, asparagine residues do not seem to be involved in coordination. Figure 44 shows a schematic representation of the Cu^{2+} -hIAPP $_{18-22}$ complex, as proposed above.

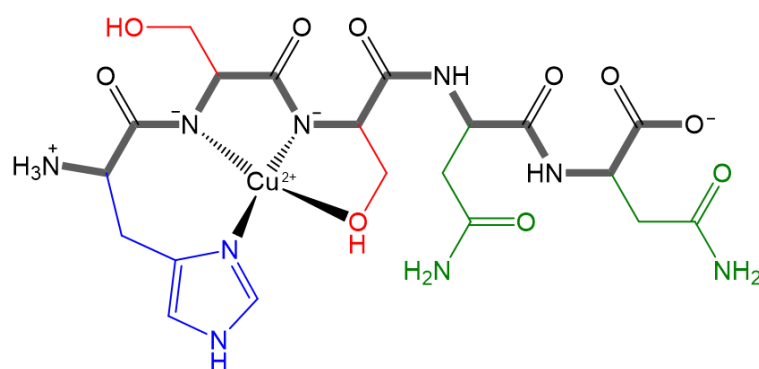


Figure 44. Proposed coordination sphere for the Cu^{2+} -hIAPP $_{18-22}$ complex. The peptide's main chain is highlighted in bold gray, while the side chains are marked in blue for H (histidine), red for S (serine) and green for N (asparagine).

This complex was then studied in the presence of 0.1 and 1.0 equivalents of each *N*-acylhydrazone, i.e. **X1NIC-(E)** and **X1NIC-(Z)**, as shown in Figure 45A

and B, respectively. The ^1H NMR spectra, acquired under the same experimental conditions, of each free hydrazone (black, top), the free peptide (black, bottom) and the copper(II)-peptide complex (blue), were added for the sake of comparison.

Interestingly, the addition of either 0.1 eq. or 1.0 eq. **X1NIC-(E)** not only does not recover the peptide's signal intensities but it also seems to broaden them even further (Figure 45A, dark yellow and orange spectra). Blue arrows identify this effect upon histidine-related signals while the color red was used for serine. All signals associated with the N21 and N22 amino acid residues remained unchanged, i.e., apart from not participating in coordination with copper(II), they also do not interact with **X1NIC-(E)**. This result is very similar to the one observed in the first part of this work, for the Alzheimer's related $\text{A}\beta\text{-Cu}^{2+}\text{-X1Benz}$ system (Carvalho *et al.*, 2023), being a strong indicative of the formation of a ternary $\text{hIAPP}_{18-22}\text{-Cu}^{2+}\text{-X1NIC-(E)}$ complex. In fact, our research group has already demonstrated, in 2019, the effect of a ternary peptide-metal-hydrazone complex on the intensity of the ^1H NMR signals, as well as thoroughly characterized, in 2022, such ternary interactions with 1-methylimidazole-containing hydrazones in aqueous solution (Cukierman *et al.*, 2019; Cukierman *et al.*, 2022). It is worth noting that, although there is a 10-fold ligand excess with respect to copper in the 1.0 eq. **X1NIC-(E)** sample, the signals related to the hydrazone are not observed at all, indicating fast exchange of the small molecule in this ternary complex.

Similarly to the experiment with the (E) isomer, the addition of **X1NIC-(Z)** also caused a decrease in the intensity of histidine- and serine-related signals and, once again, metal abstraction can be ruled out in favor of the formation of a ternary species. However, an important difference with the previous set of experiments was observed: the appearance of **X1NIC-(Z)** signals, which can be seen highlighted by red dotted lines in the spectra shown in Figure 45B. At the copper:**X1NIC-(Z)** equimolar condition 0.1 eq., this is a clear indicative that the interactions of this bidentate hydrazone with the $\text{Cu}^{2+}\text{-hIAPP}_{18-22}$ system are weaker than those of the (E) isomer. However, when the hydrazone is present in excess (1.0 eq.) with respect to the metal ion, it shows that the exchange of the ligand with the ternary complex is quite slow and both conditions (*i.e.*, free and bound ligand) can be identified in the NMR timescale. This could mean that, although the ternary complex with the (Z) isomer is thermodynamically less stable

(weaker interactions), it is probably kinetically more inert (slower change rates between the free and bound states).

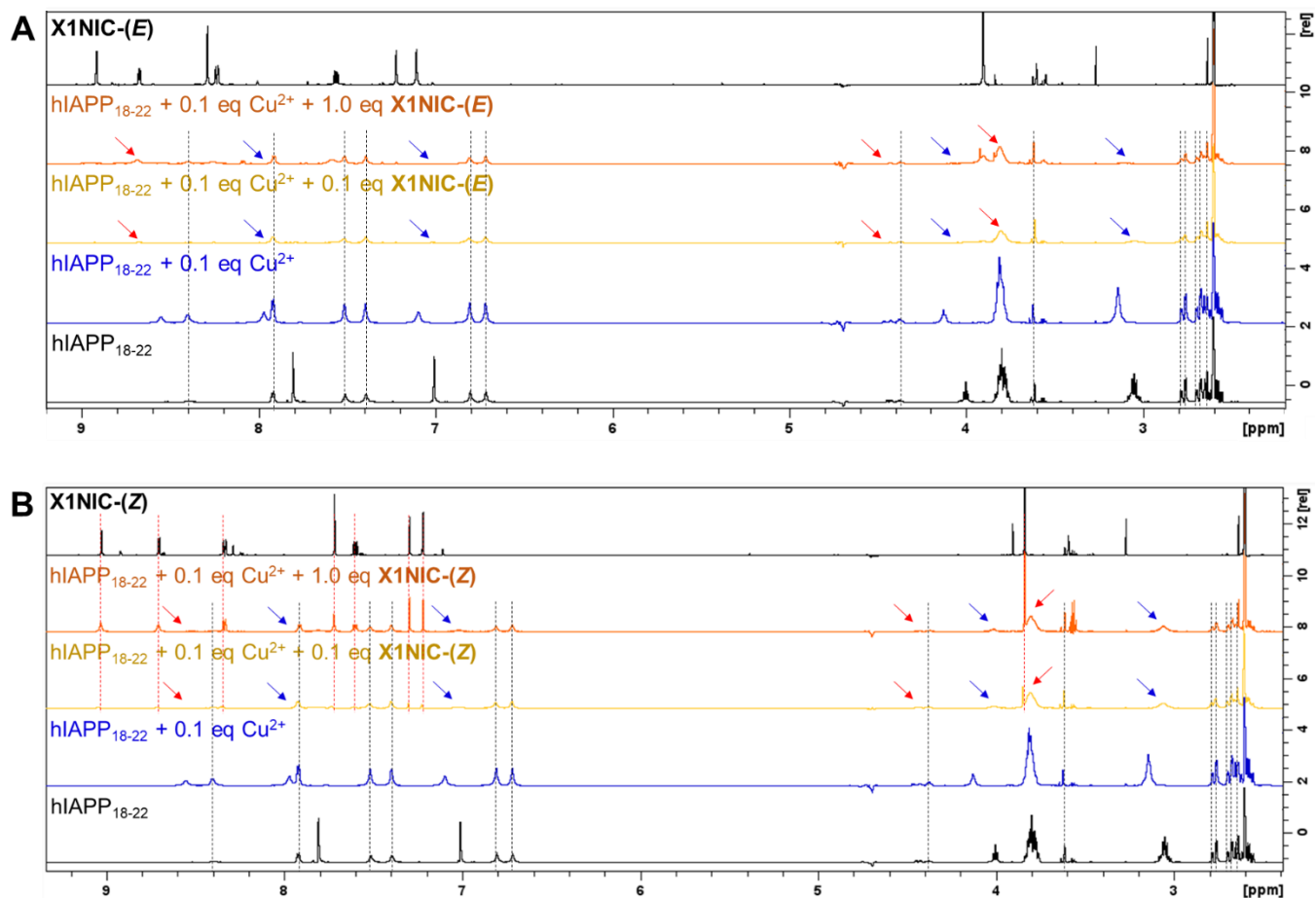


Figure 45. Interactions of (A) X1NIC-(E) and (B) X1NIC-(Z) with the Cu^{2+} -hIAPP₁₈₋₂₂ system. For each compound, from bottom to top: ^1H NMR spectra (700 MHz) of hIAPP₁₈₋₂₂, hIAPP₁₈₋₂₂ + 0.1 eq. Cu^{2+} , hIAPP₁₈₋₂₂ + 0.1 eq. Cu^{2+} + 0.1 eq. compound, hIAPP₁₈₋₂₂ + 0.1 eq. Cu^{2+} + 1.0 eq. compound, and pure compound spectrum for comparison purposes. All spectra were acquired at 25 °C. Samples were prepared in 20 mmol L⁻¹ Tris-*d*₁₁ pH 7.4, with 8.5% D₂O and 4% DMSO-*d*₆. Arrows point to relevant spectral changes: red is used for changes in serine-related signals while blue refers to histidine. Red dotted lines highlight compound signals that remained unchanged. Black dotted lines, on the other hand, were used to point out unaffected peptide signals.

5.2.7. Cyclic voltammetry study of both binary (Cu^{2+} -hIAPP₁₈₋₂₂ and Cu^{2+} -X1NIC) and ternary (X1NIC- Cu^{2+} -hIAPP₁₈₋₂₂) systems

Since copper is an electroactive element, due to the ready availability of the +1 and +2 oxidation states in an accessible potential range, we decided to follow the interactions of this metal both in the binary and in the ternary systems involving each X1NIC isomer and hIAPP₁₈₋₂₂ through cyclic voltammetry (CV). As this technique is mainly focused on the metal, it can be considered a complementary way to confirm the conclusions taken from the ligand-oriented NMR assays.

Cu^{2+} -hIAPP₁₈₋₂₂ binary system

On one hand, the voltammogram of CuCl_2 in buffer (50 mmol L⁻¹ HEPES pH 7.4, 100 mmol L⁻¹ NaCl) shows a *quasi*-reversible process at $E_{1/2} = + 160$ mV vs. Ag/AgCl, corresponds to the redox pair $\text{Cu}^{2+}/\text{Cu}^+$, as can be seen in the dark gray dotted line at the bottom of Figure 46. When present in a similar medium containing 5% of the coordinating solvent DMSO, on the other hand, the *quasi*-reversible process observed in the CV of CuCl_2 occurs at $E_{1/2} = + 90.5$ mV (black line in the top of Figure 46). Another anodic process can also be seen at $- 53$ mV. Together, these evidences suggest the existence of more than one metal species, possibly with one or more DMSO molecules coordinating copper in all of them.

The peptide on its own is not electroactive, as shown in red in Figure 46. However, in the presence of equimolar amounts of copper(II) (blue line), a *quasi*-reversible process at $E_{1/2} = + 90.5$ mV can be seen, indicating that there are still “free” metal ions in solution, *i.e.*, not bound to the peptide itself. Nevertheless, the anodic peak at $- 53$ mV is no longer observed and, in turn, another peak at $- 115$ mV arises. This was attributed to a process related to the binary complex Cu^{2+} -hIAPP₁₈₋₂₂. A diffuse cathodic process could also be detected around $- 200$ mV, corresponding to the reduction of Cu^{2+} into Cu^+ . This profile somewhat differs from the one reported by Seal and Dey (2018). However, although they employed both the complete human IAPP and its N-terminal region, the latter only contained the amino acid residues from 1 to 19, which may explain such difference, since it does not involve the same coordination set as the one in hIAPP₁₈₋₂₂.

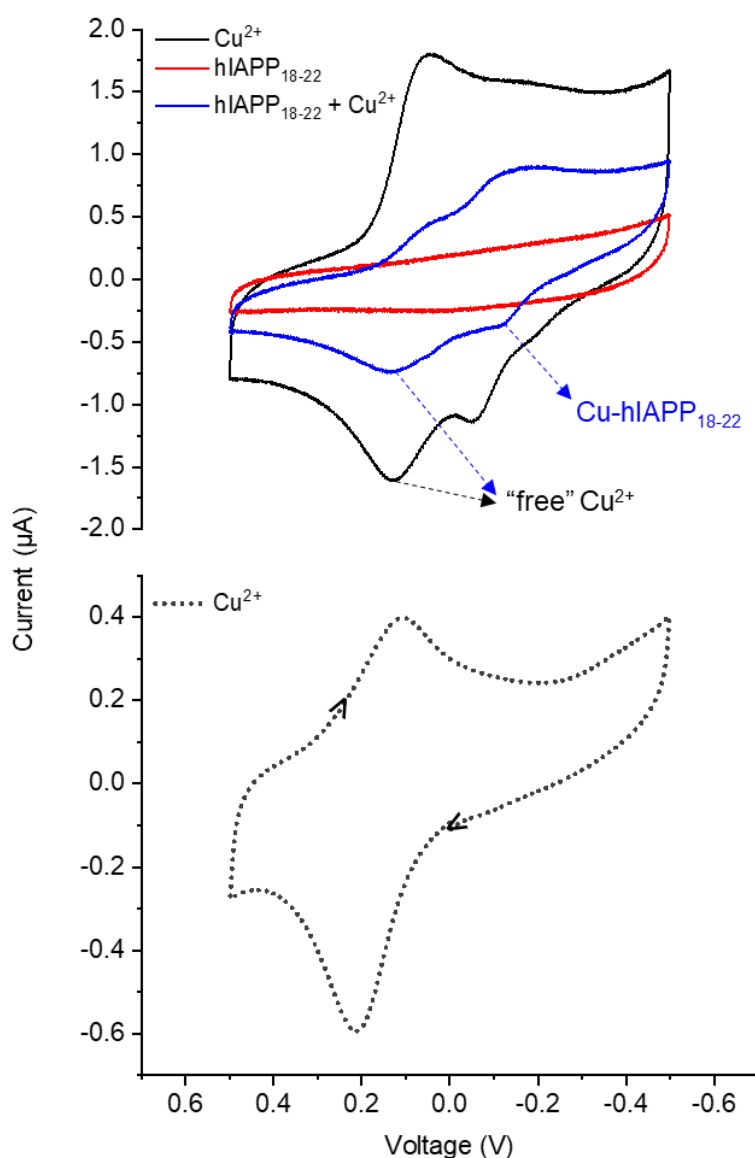


Figure 46. Cyclic voltammetry of the binary system involving Cu^{2+} and the human IAPP coordinating fragment hIAPP₁₈₋₂₂ (HSSNN). **Top:** CVs of Cu^{2+} at 0.1 mmol L⁻¹ (black), hIAPP₁₈₋₂₂ at 0.1 mmol L⁻¹ (red) and a 1:1 molar mixture of hIAPP₁₈₋₂₂ and Cu^{2+} (blue). Conditions: 5% DMSO / buffer (50 mmol L⁻¹ HEPES pH 7.4, 100 mmol L⁻¹ NaCl) solution, at room temperature. **Bottom:** CV of Cu^{2+} (0.1 mmol L⁻¹) in the absence of DMSO (50 mmol L⁻¹ HEPES pH 7.4, containing 100 mmol L⁻¹ NaCl), at room temperature.

Cu^{2+} -X1NIC binary systems

Similarly to the peptide, in the absence of copper, the (*E*) isomer of X1NIC is not electroactive (black line, Figure 47). When present at 1:1 stoichiometry with copper, two waves, one cathodic and the other anodic, can be clearly identified at the potentials of -135 mV and +195 mV, respectively, shown in yellow in the figure. These processes were attributed to the ML complex. Nevertheless, there is,

once again, a small amount of “free” copper in solution, as evidenced by the residual wave indicated by arrows in the figure. Upon complexation, Cu^{2+} becomes harder to be reduced in comparison to its “free” form, as can be stated by the displacement of the reduction process to a more negative potential. This is in accordance with the fact that tridentate **X1NIC-(E)** ligand probably occupies three of the four equatorial positions in the coordination sphere of the metal. Thus, in order to reduce it to Cu^+ , a **X1NIC-(E)**-related coordinated donor atom must be lost, so that the coordination sphere can be adjusted from square planar to tetrahedral. Once acting as a bidentate ligand, rearrangement of the geometry is easier for the oxidation process, which explains why this displacement is smaller for the anodic peak.

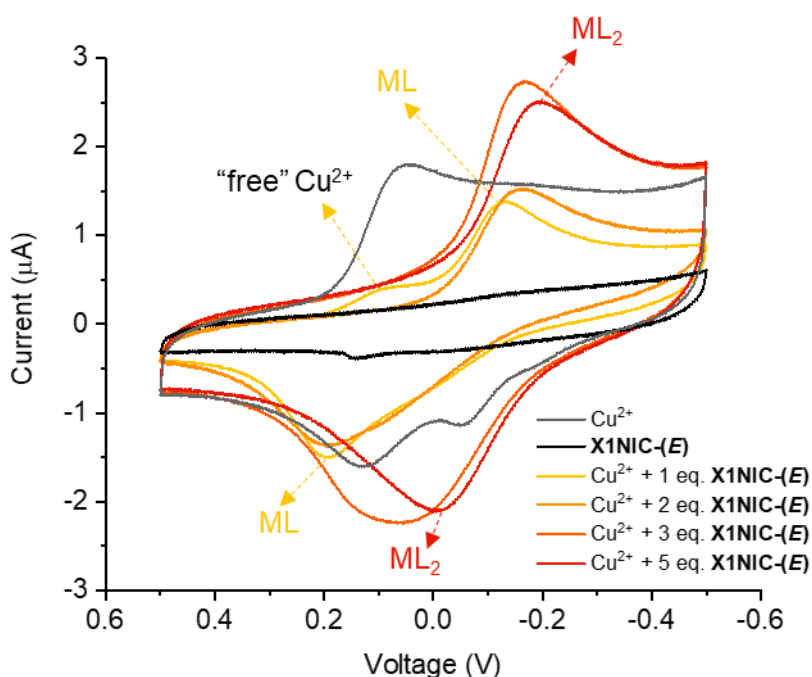


Figure 47. Cyclic voltammetry of the binary system involving Cu^{2+} and **X1NIC-(E)**. Conditions: 5% DMSO / buffer (50 mmol L^{-1} HEPES pH 7.4, 100 mmol L^{-1} NaCl) solution, at room temperature. $[\text{Cu}^{2+}] = 0.1 \text{ mmol L}^{-1}$. $[\text{X1NIC-(E)}] = 0.1\text{-}0.5 \text{ mmol L}^{-1}$. “Free” copper (at concentration of 0.1 mmol L^{-1}) voltammogram included for the sake of comparison (gray line).

Upon addition of a second equivalent of ligand, the remaining “free” copper appears to be completely consumed, and a mixture of the ML and ML_2 complexes compose the solution. Further increase in **X1NIC-(E)** concentration reduces the presence of the ML complex, favoring ML_2 stoichiometry until finally, with 5 eq. of ligand, this seems to be the main complex in solution, characterized by a *quasi-*

reversible process at $E_{1/2} = -102$ mV (red CV in Figure 47). It is worth mentioning that the need for a great excess of ligand to force ML_2 formation indicates that this complex is not thermodynamically favored, which is more than probably due to the Jahn-Teller effect observed for copper(II).

The same study was performed for the (*Z*) isomer, and the voltammograms are shown in Figure 48. Upon addition of the first equivalent of **X1NIC**, “free” copper can anew be observed, and seems to still be present, at a lesser amount, even after the second addition (2 eq.) of **X1NIC-(Z)**. An important feature of this system that is not seen in that of the (*E*) isomer is the presence of two reduction (located at -242 mV and -350 mV) and two oxidation (at -9 mV and $+225$ mV) processes, suggesting an equilibrium involving different species generated by the substitution of the labile sites in the complex. A mixture of ML and ML_2 complexes is discarded since this pattern remains even in the presence of 5 eq. of ligand, condition in which the ML species should no longer exist. In fact, very little variation is observed with the addition of 3 eq., in which “free” copper is not present anymore, or 5 eq. So, as indicated by other techniques discussed above, such as UV-Vis and 1H NMR, and confirmed by CV, the ligand **X1NIC-(Z)** is very different from its tridentate (*E*) isomer in terms of its coordination chemistry in solution.

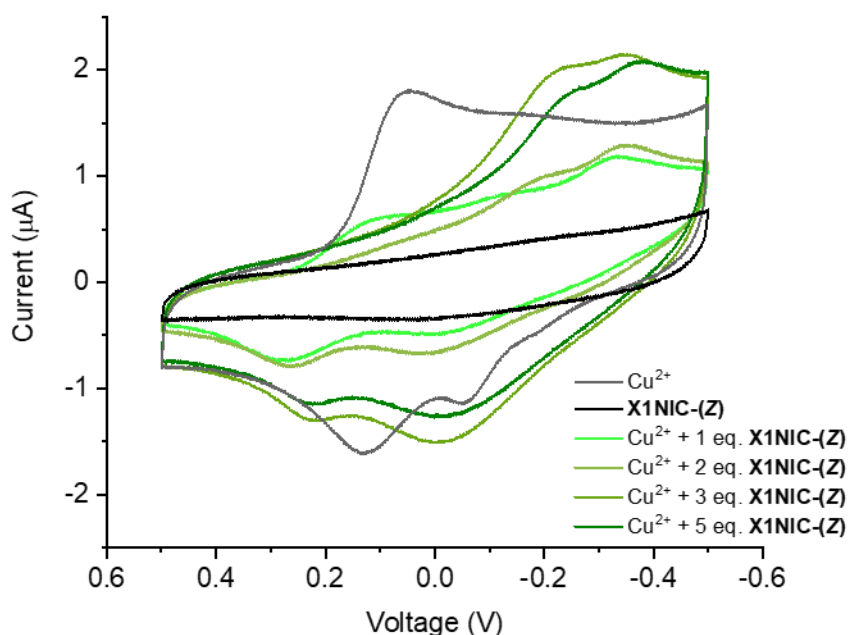


Figure 48. Cyclic voltammetry of the binary system involving Cu^{2+} and **X1NIC-(Z)**. Conditions: 5% DMSO / buffer (50 mmol L^{-1} HEPES pH 7.4, 100 mmol L^{-1} NaCl) solution, at room temperature. $[\text{Cu}^{2+}] = 0.1 \text{ mmol L}^{-1}$. $[\text{X1NIC-(Z)}] = 0.1\text{-}0.5 \text{ mmol L}^{-1}$. “Free” copper (at concentration of 0.1 mmol L^{-1}) voltammogram included for the sake of comparison (gray line).

X1NIC-Cu²⁺-hIAPP₁₈₋₂₂ ternary systems

After studying the binary systems individually, we decided to evaluate the metallophoric potential of the hydrazones by titrating the hIAPP₁₈₋₂₂-Cu²⁺ mixture with increasing amounts of each *N*-acylhydrazonic ligand. Additions corresponded to 0.1 eq., until the 1:1:1 ternary system was reached. A final CV was also recorded in the presence of an excess (2 eq.) of the small molecules.

For **X1NIC-(E)**, data are reported in Figure 49. Upon addition of increasing amounts of the ligand, not only the wave related to the remaining copper in solution progressively vanishes but also that of the Cu²⁺-hIAPP₁₈₋₂₂ complex (represented by the anodic process at -115 mV). When the 1:1:1 stoichiometry is reached (pink CV), a ternary complex can be proposed, characterized by a cathodic peak at around -175 mV and an anodic one, observed at +160 mV. Thus, we can conclude that both binary complexes, either with the (*E*)-hydrazone or with the peptide, are not completely favored, since in both cases there is still copper in solution. However, when the three components are present at equimolar amounts, this does not occur, and neither binary complex is observed individually

in this condition as well. This is in perfect agreement with the NMR results discussed above and indicate that the binding of **X1NIC-(E)** and hIAPP₁₈₋₂₂ to copper(II) is a cooperative process.

Finally, an excess of the tridentate (*E*) *N*-acylhydrazonic ligand (purple CV) seems to be able to start to promote the clearance of Cu²⁺ from hIAPP₁₈₋₂₂, as can be observed by the partial disappearance of the ternary complex-related process (at +160 mV) and the shift of the cathodic wave to more negative potentials which, by comparison to the one in the Cu²⁺-**X1NIC-(E)** binary system, may be related to the formation of the ML₂ species. Nevertheless, an even greater excess of hydrazone would be necessary to completely abolish the metal-peptide interaction.

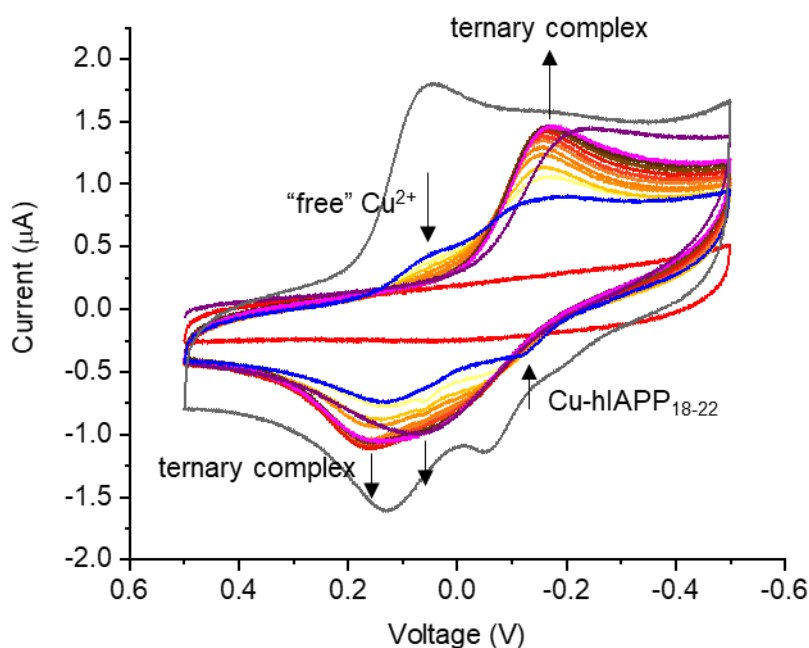


Figure 49. Titration of the Cu²⁺-hIAPP₁₈₋₂₂ system with increasing amounts of **X1NIC-(E)**. Conditions: 5% DMSO / buffer (50 mmol L⁻¹ HEPES pH 7.4, 100 mmol L⁻¹ NaCl) solution, at room temperature. Red: free hIAPP₁₈₋₂₂ (0.1 mmol L⁻¹). Dark gray: “free” Cu²⁺ (0.1 mmol L⁻¹). Blue: Cu²⁺-hIAPP₁₈₋₂₂ at 1:1 stoichiometry. From yellow to dark orange: additions of 0.1 eq. **X1NIC-(E)** (concentration range: 0.01-0.09 mmol L⁻¹). Pink: [**X1NIC-(E)**] = 0.1 mmol L⁻¹. Purple: [**X1NIC-(E)**] = 0.2 mmol L⁻¹. “Free” copper (at concentration of 0.1 mmol L⁻¹) voltammogram included for the sake of comparison (gray line).

The titration of the Cu-hIAPP₁₈₋₂₂ complex with **X1NIC-(Z)** (Figure 50), on the other hand revealed a much more intricate system. Although the same initial results are observed, *i.e.* the progressive reduction of the waves related to

“free” copper and Cu^{2+} -hIAPP₁₈₋₂₂ complex, two, instead of one, new cathodic (–225 mV and –380 mV) and anodic (at +5 mV and +260 mV) processes arise, which are different from those observed for the binary Cu^{2+} -**X1NIC-(Z)** system. For this reason, they were attributed to the formation of ternary species involving copper coordination by the azomethine nitrogen and the carbonyl oxygen from **X1NIC-(Z)** and the imidazole nitrogen from the histidine residue in the hIAPP₁₈₋₂₂ peptide. The fourth, available equatorial position in the coordination sphere of the metal can be responsible for the presence of more than one complex in solution.

Interestingly, addition of an excess of ligand (2 eq., represented in purple) does not induce any change in the voltammogram compared to the 1:1:1 system (shown in pink), indicating that the (Z) isomer, different from its (E) counterpart, cannot abstract copper(II) from hIAPP₁₈₋₂₂, and, thus, that the ternary species are somewhat stable. Once again, this is in agreement with the observations from NMR experiments, which point to an inert ternary complex when **X1NIC-(Z)** is involved.

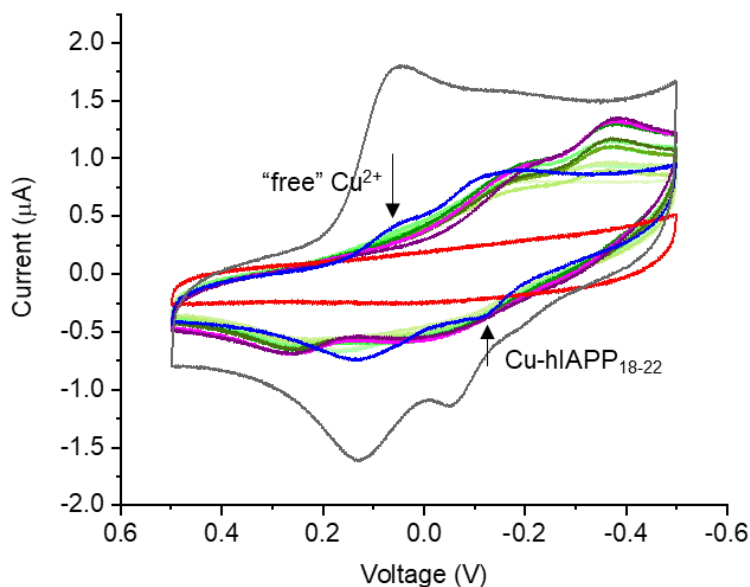


Figure 50. Titration of the Cu^{2+} -hIAPP₁₈₋₂₂ system with increasing amounts of **X1NIC-(Z)**. Conditions: 5% DMSO / buffer (50 mmol L⁻¹ HEPES pH 7.4, 100 mmol L⁻¹ NaCl) solution, at room temperature. Red: free hIAPP₁₈₋₂₂ (0.1 mmol L⁻¹). Dark gray: “free” Cu^{2+} (0.1 mmol L⁻¹). Blue: Cu^{2+} -hIAPP₁₈₋₂₂ at 1:1 stoichiometry. From light to dark green: additions of 0.1 eq. **X1NIC-(Z)** (concentration range: 0.01-0.09 mmol L⁻¹). Pink: [**X1NIC-(Z)**] = 0.1 mmol L⁻¹. Purple: [**X1NIC-(Z)**] = 0.2 mmol L⁻¹.

To the best of our knowledge, this is the first in depth description of the interactions of the coordinating fragment hIAPP₁₈₋₂₂ with copper(II) using this technique. Moreover, this work also reveals in great detail, and for the first time *via* cyclic voltammetry, the only recently proposed mechanism of action of tridentate hydrazonic metallophores that form stable ternary complexes at a 1:1:1 molar ratio, before disrupting the anomalous metal-protein interactions when present in molar excess. Nevertheless, it is important to mention that the ternary species are already enough to partially passivate the metal, avoiding deleterious redox cycling effects.

Copper is an essential metal for the normal functioning of the body, and changes in its concentration are associated with several diseases, including diabetes (Gembillo *et al.*, 2023). Since free copper can catalyze the formation of ROS through the cycling between its two oxidation states (+1 and +2), this metal is tightly regulated in living organisms. In the circulatory system, copper is bound to carrier proteins such as serum albumin, while its transport into cells is mediated by CTR1. Once in the cytoplasm, copper – in its reduced state copper(I) – is bound to ATOX1 protein, and in healthy, physiological circumstances, any excess of the metal is excreted in bile. Under pathological conditions, however, copper can be found bound to other proteins, including amyloidogenic peptides, such as IAPP. In this context, Qiu *et al.* (2017) performed a meta-analysis of plasma and serum copper concentrations and observed that patients affected by diabetes *mellitus* had higher levels of copper than healthy people, indicating that this pathology is related to an increase or improper distribution of this metal in the body. Therefore, the search for metallophores that can impair such abnormal interactions, either through metal sequestering, or through inactivation of its redox cycle is a valid approach that certainly deserve further investigation.

6. Conclusions

In this work, two new *N*-acylhydrazones derived from 1-methylimidazole-2-carboxaldehyde were proposed based on the structure of molecules with known receptors in the human body (mescaline and nicotine): **X1TMP** (1-methyl-1H-imidazole-2-carboxaldehyde 3,4,5-trimethoxybenzoyl hydrazone) and **X1NIC** (1-methyl-1H-imidazole-2-carboxaldehyde nicotinoyl hydrazone), respectively. The unsubstituted derivative of **X1TMP**, *i.e.* 1-methyl-1H-imidazole-2-carboxaldehyde benzoyl hydrazone (**X1Benz**), was also prepared and employed as a comparative model. The synthesis of **X1NIC** afforded a mixture of (*E*) and (*Z*) isomers. For this reason, conditions were optimized in order to prepare them individually as **X1NIC-(E)** and **X1NIC-(Z)**. Thus, all four compounds were isolated in moderate to good yields (30-83%) and high purity. With the exception of **X1NIC-(Z)**, which was obtained as the free-base with an intramolecular H-bond between the amide -NH and the imidazolic nitrogen, all the hydrazones were obtained as hydrochlorides, presenting only one set of signals in their ¹H NMR spectra, related to the (*E*)-amido tautomer. The compounds were characterized in the solid state through mid-IR, thermogravimetry and melting points. Moreover, the four *N*-acylhydrazones were completely stable in 1% DMSO/Tris pH 7.4 solution. The experimental log P values were determined as follows - **X1TMP**: 1.55 ± 0.17 ; **X1Benz**: 1.49 ± 0.13 ; **X1NIC-(E)**: 0.62 ± 0.01 and **X1NIC-(Z)**: 0.87 ± 0.02 , values which are all within the ideal range considered for oral administration and BBB crossing.

The isomerization of **X1NIC-(E)** and (*Z*) as a function of temperature was evaluated by ¹H NMR spectroscopy. While the (*E*) isomer is irreversibly converted into **X1NIC-(Z)**, the latter did not undergo thermally induced isomerization, indicating that it is the thermodynamically favored product.

Upon interaction with copper(II) ions, which is relevant in the context of both Alzheimer's disease and type-2 diabetes *mellitus*, all ligands preferably generate ML complexes, as demonstrated by the Job Method from UV-Vis measurements. Regarding the related **X1TMP** and **X1Benz**, comparable ligand-to-metal affinities were obtained, with log K_{app} values in aqueous buffered medium of 5.74 ± 0.15 and 5.87 ± 0.11 , respectively, indicating that the presence of methoxyl substituents in the former does not greatly influence the stability of

the complex formed. On the other hand, the nicotine-inspired ligands presented $\log K_{\text{app}}$ values of 5.82 ± 0.16 and 5.04 ± 0.04 , for the (*E*) and the (*Z*) isomers, correspondingly. The higher value (almost a logarithmic unit) obtained for **X1NIC-(E)** indicates greater affinity of this hydrazone for copper(II), which is consistent with the fact that it can perform as a tridentate ligand, while **X1NIC-(Z)** can only coordinate in a bidentate manner.

The metallophoric potential of these hydrazones was assessed in the context of copper-enhanced endocrine and neuroendocrine aggregopathies. As mescaline can selectively bind serotonin receptors in the brain, **X1TMP** (and its derivative **X1Benz**) was studied in models of Alzheimer's disease, using the $A\beta_{1-40}$ peptide and its coordinating fragment $A\beta_{1-16}$. In this sense, both compounds were able to lessen the production of ROS by the Cu($A\beta$)-system under pseudo-physiological conditions, with **X1TMP** being slightly more effective than **X1Benz**. Additionally, the hydrazones showed the capacity of preventing $A\beta$ aggregation at equimolar conditions in the presence and, quite unexpectedly, in the absence of copper. 2D ^1H - ^{15}N HSQC NMR experiments demonstrated a direct interaction between $A\beta$ and **X1Benz**, which can be at the core of this phenomenon. On the other hand, the activity behind the inhibition of copper-mediated $A\beta$ aggregates formation may be related to a 1:1:1 ternary species, as demonstrated for **X1Benz** by 1D ^1H NMR. Although **X1TMP** presented relatively low solubility compared to **X1Benz**, this probably does not represent a problem for its potential use as a metallophore, since the concentrations required to exert such a function in the CNS are generally very small, of the order of a few milligrams per kilogram of weight.

Regarding **X1NIC**, since nicotine has functional receptors in the pancreas and a close relationship with type-2 diabetes *mellitus*, its isomers were assessed in biophysical models of the human islet amyloid polypeptide, using the coordinating fragment hIAPP₁₈₋₂₂. First, a copper(II) N₃O-coordination mode was confirmed for this peptide using high-field NMR spectroscopy. CV measurements showed that this complex is characterized by an anodic peak at -115 mV. The susceptibility of the Cu^{2+} -hIAPP₁₈₋₂₂ system to the presence of each **X1NIC** isomer was then studied by both NMR and CV. Interestingly, the addition of either stereoisomer seemed to strengthen the interaction between peptide and metal and, in both cases, copper(II) abstraction was ruled out at low hydrazone

concentrations in favor of the formation of the correspondent ternary species. However, CV assays in a solution containing a 1:1:2 (peptide:metal:ligand) stoichiometry indicated that **X1NIC-(E)** is able to remove copper from hIAPP₁₈₋₂₂, while addition of (Z) isomer excess does not induce any apparent change. It is important to mention that the ternary species are already enough to partially passivate the metal, avoiding deleterious redox cycling effects.

In general, these new compounds that belong to the 1-methylimidazole family of *N*-acylhydrazones demonstrated a promising metallophoric activity, presenting moderate affinity towards copper(II) ions (in the same order of magnitude than other hydrazones previously reported by our research group), and proved ability to interfere with anomalous, deleterious copper-peptide interactions. Nevertheless, further investigation must be made to determine the toxicity of the ternary species identified and characterized in the present study.

Altogether with previous works by the group, these findings may suggest the need to adapt the current definition of metallophore in order to include not only those ligands that compete with the protein for the metal ion, but the ones that exercise their activity by the formation of stable, mostly inert, ternary species as well. More work needs to be done in order to understand the structural features that lead some *N*-acylhydrazones to exert their activity through this pathway.

7. References

ADLARD, P. A. *et al.* Rapid Restoration of Cognition in Alzheimer's Transgenic Mice with 8-Hydroxy Quinoline Analogs Is Associated with Decreased Interstitial A β . **Neuron**, v. 59, n. 1, p. 43-55, 10 jul. 2008. Available at: < <https://doi.org/10.1016/j.neuron.2008.06.018> >.

AHMAD, E. *et al.* A mechanistic approach for islet amyloid polypeptide aggregation to develop anti-amyloidogenic agents for type-2 diabetes. **Biochimie**, v. 93, n. 5, p. 793-805, 5 jan. 2011. Available at: < <https://doi.org/10.1016/j.biochi.2010.12.012> >.

ALGHRABLY, M. *et al.* Interaction of amylin species with transition metals and membranes. **Journal of Inorganic Biochemistry**, v. 191, p. 69-76, 2019. Available at: < <https://doi.org/10.1016/j.jinorgbio.2018.11.004> >.

ALGHRABLY, M. *et al.* Copper(II) and Amylin Analogues: A Complicated Relationship. **Inorganic Chemistry**, v. 59, n. 4, p. 2527-2535, 6 fev. 2020. Available at: < <https://doi.org/10.1021/acs.inorgchem.9b03498> >.

ALIREZAEI, Z. *et al.* Neurofilament Light Chain as a Biomarker, and Correlation with Magnetic Resonance Imaging in Diagnosis of CNS-Related Disorders. **Molecular Neurobiology**, v. 57, n. 1, p. 469-491, jan. 2020. Available at: < <https://doi.org/10.1007/s12035-019-01698-3> >.

ALMEIDA, Z. C. L. **Cinética de Agregação da Proteína Transtirretina: Contribuição para a compreensão dos processos de formação de amilóide.** Coimbra, 2010. 108p. Dissertation (Masters in Chemistry) – College of Sciences and Technology, University of Coimbra.

ALMEIDA-PITITTO, B. *et al.* Brazilian Type 1 & 2 Diabetes Disease Registry (BINDER): longitudinal, real-world study of diabetes mellitus control in Brazil. **Frontiers in Clinical Diabetes and Healthcare**, v. 3, 2022. Available at: < <https://doi.org/10.3389/fcdhc.2022.934629> >.

ALREFAI, H. A. *et al.* Pramlintide: Clinical Strategies for Success. **Diabetes Spectrum**, v. 23, n. 2, p. 124-130, 2010. Available at: < <https://doi.org/10.2337/diaspect.23.2.124> >.

ALZHEIMER'S ASSOCIATION. 2023 Alzheimer's disease facts and figures. **Alzheimer's and Dementia**, v. 19, n. 4, p. 1598-1695, apr. 2023. Available at: < <https://doi.org/10.1002/alz.13016> >.

ARAÚJO, S. R. M. *et al.* Doença de Alzheimer no Brasil: uma análise epidemiológica entre 2013 e 2022. **Research, Society and Development**, v. 12, n. 2, fev. 2023. Available at: < <https://doi.org/10.33448/rsd-v12i2.40345> >.

ASHWOOD, V. A. *et al.* Utilization of an intramolecular hydrogen bond to increase the CNS penetration of an NK1 receptor antagonist. **Journal of Medicinal Chemistry**, v. 44, n. 14, p. 2276-2285, 9 jun. 2001. Available at: < <https://doi.org/10.1021/jm010825z> >.

ASTHANA, S. *et al.* IAPP in type II diabetes: Basic research on structure, molecular interactions, and disease mechanisms suggests potential intervention strategies. **Biochimica et Biophysica Acta – Biomembranes**, v. 1860, n. 9, p. 1765-1782, 6 mar. 2018. Available at: < <https://doi.org/10.1016/j.bbamem.2018.02.020> >.

ATRIÁN-BLASCO, E. *et al.* Ascorbate Oxidation by Cu(Amyloid- β) Complexes: Determination of the Intrinsic Rate as a Function of Alterations in the Peptide Sequence Revealing Key Residues for Reactive Oxygen Species Production. **Analytical Chemistry**, v. 90, n. 9, p. 5909-5915, 3 apr. 2018. Available at: < <https://doi.org/10.1021/acs.analchem.8b00740> >.

ATWOOD, C. S. *et al.* Dramatic Aggregation of Alzheimer A by Cu(II) Is Induced by Conditions Representing Physiological Acidosis*. **The Journal of Biological Chemistry**, v. 273, n. 21, p. 12817-12826, 22 may 1998. Available at: < <https://doi.org/10.1074/jbc.273.21.12817> >.

AVRAM, O. R., CARAGEA, G., VARZARU, C. A. Copper and its role in the human body - the importance of establishing copper concentrations in the body. **Romanian Journal of Military Medicine**, v. 124, n. 2, p. 254-260, may 2021. Available at: < <https://www.revistamedicinamilitara.ro/wp-content/uploads/2021/04/Copper-and-its-role-in-the-human-body-%E2%80%93-the-importance-of-establishing-copper-concentrations-in-the-body-1.pdf> >.

BAREGGI, S. R., CORNELLI, U. Clioquinol: Review of its mechanisms of action and clinical uses in neurodegenerative Disorders. **CNS Neurosciences & Therapeutics**, v. 18, n. 1, p. 41-46, 2012. Available at: < <https://doi.org/10.1111/j.1755-5949.2010.00231.x> >.

BARTHOLD, D. *et al.* Pharmaceutical Treatment for Alzheimer's Disease and Related Dementias: Utilization and Disparities. **Journal of Alzheimer's Disease**, v. 76, n. 2, p. 579–589, 2020. Available at: < <https://doi.org/10.3233/JAD-200133> >.

BENKOVIĆ, T. *et al.* Acid–Base Properties and Kinetics of Hydrolysis of Aroylhydrazones Derived from Nicotinic Acid Hydrazide. **Journal of Solution Chemistry**, v. 45, n. 8, p. 1227–1245, 17 aug. 2016. Available at: < <https://doi.org/10.1007/s10953-016-0504-8> >.

BUDIMIR, A. Metal ions, Alzheimer's disease and chelation therapy. **Acta Pharmaceutica**, v. 61, n. 1, p. 1–14, 17 mar. 2011. Available at: < <https://doi.org/10.2478/v10007-011-0006-6> >.

BUXBAUM J. N. Amyloid nomenclature 2022: update, novel proteins, and recommendations by the International Society of Amyloidosis (ISA) Nomenclature Committee. **The Journal of Protein Folding Disorders**, v. 29, n. 4, p. 213–219, 2022. Available at: < <https://doi.org/10.1080/13506129.2022.2147636> >.

CARVALHO, A. *et al.* New mescaline-related N-acylhydrazone and its unsubstituted benzoyl derivative: Promising metallophores for copper-associated

deleterious effects relief in Alzheimer's disease. **Journal of Inorganic Biochemistry**, v. 238, p. 112033, jan. 2023. Available at: < <https://doi.org/10.1016/j.jinorgbio.2022.112033> >.

CASSELS, B. K., SÁEZ-BRIONES, P. Dark Classics in Chemical Neuroscience: Mescaline. **ACS Chemical Neuroscience**, v. 9, n. 10, p. 2448–2458, 2018. Available at: < <https://doi.org/10.1021/acschemneuro.8b00215> >.

CAVALCANTI, J. L., ENGELHARDT, E. Aspectos da fisiopatologia da doença de Alzheimer esporádica Pathophysiological features of sporadic Alzheimer's disease. **Revista Brasileira de Neurologia**, v. 48, n. 4, p. 21-29, 2012. Available at: < <https://pesquisa.bvsalud.org/portal/resource/pt/lil-666936> >.

CAVANAGH J. **Protein NMR Spectroscopy: Principles and Practice**. Second Edition. Boston: Academic Press, 2007. Available at: < <https://search.library.wisc.edu/catalog/9910027380502121> >.

CHANG, Y. J., CHEN, Y. R. The coexistence of an equal amount of Alzheimer's amyloid- β 40 and 42 forms structurally stable and toxic oligomers through a distinct pathway. **FEBS Journal**, v. 281, n. 11, p. 2674–2687, 10 apr. 2014. Available at: < <https://doi.org/10.1111/febs.12813> >.

CHASAPIS, C. T. *et al.* Recent aspects of the effects of zinc on human health. **Archives of Toxicology**, v. 94, n. 5, p. 1443–1460, 12 may 2020. Available at: < <https://doi.org/10.1007/s00204-020-02702-9> >.

CHIANG, P. K., LAM, M. A., LUO, Y. The Many Faces of Amyloid in Alzheimer's Disease. **Current Molecular Medicine**, v. 8, n. 6, p. 580-584, 2008. Available at: < <https://doi.org/10.2174/156652408785747951> >.

CHITI, F., DOBSON, C. M. Protein misfolding, functional amyloid, and human disease. **Annual Review of Biochemistry**, v. 75, p. 333–366, 2006. Available at: < <https://doi.org/10.1146/annurev.biochem.75.101304.123901> >.

CHITI, F., DOBSON, C. M. Protein Misfolding, Amyloid Formation, and Human Disease: A Summary of Progress Over the Last Decade. **Annual Review of Biochemistry**, v. 86, p. 27-60, jun. 2017. Available at: < <https://doi.org/10.1146/annurev-biochem> >.

CONTE-DABAN, A. *et al.* How Zn can impede Cu detoxification by chelating agents in Alzheimer's disease: A proof-of-concept study. **Dalton Transactions**, v. 45, n. 39, p. 15671–15678, 31 aug. 2016. Available at: < <https://doi.org/10.1039/c6dt02308h> >.

CONTESSOTO, V. G. *et al.* Introduction to the protein folding problem: An approach using simplified computational models. **Revista Brasileira de Ensino de Física**, v. 40, n. 4, p. e4307, 2018. Available at: < <https://doi.org/10.1590/1806-9126-RBEF-2018-0068> >.

CUKIERMAN, D. S. *et al.* Aroylhydrazones constitute a promising class of 'metal-protein attenuating compounds' for the treatment of Alzheimer's disease: a

proof-of-concept based on the study of the interactions between zinc(II) and pyridine-2-carboxaldehyde isonicotinoyl hydrazone. **Journal of Biological Inorganic Chemistry**, v. 23, n. 8, p. 1227–1241, 2018. Available at: < <https://doi.org/10.1007/s00775-018-1606-0> >.

CUKIERMAN, D. S. *et al.* Full Equilibrium Picture in Aqueous Binary and Ternary Systems Involving Copper(II), 1-Methylimidazole-Containing Hydrazonic Ligands, and the 103-112 Human Prion Protein Fragment. **Inorganic Chemistry**, v. 61, n. 1, p. 723–737, 2022. Available at: < <https://doi.org/10.1021/acs.inorgchem.1c03598> >.

CUKIERMAN, D. S. *et al.* Impact of pyridine-2-carboxaldehyde-derived aroylhydrazones on the copper-catalyzed oxidation of the M112A PrP103–112 mutant fragment. **Journal of Biological Inorganic Chemistry**, v. 24, n. 8, p. 1231–1244, 2019. Available at: < <https://doi.org/10.1007/s00775-019-01700-2> >.

CUKIERMAN, D. S. *et al.* X1INH, an improved next-generation affinity-optimized hydrazonic ligand, attenuates abnormal copper(i)/copper(ii)- α -Syn interactions and affects protein aggregation in a cellular model of synucleinopathy. **Dalton Transactions**, v. 49, n. 45, p. 16252–16267, 2020. Available at: < <https://doi.org/10.1039/d0dt01138j> >.

CUKIERMAN, D. S. *et al.* Crystal Structure and Hirshfeld Analysis of a Poorly Water Soluble Bis(ligand)copper(II) Complex Containing the Metallophore Pyridine-2-Carboxaldehyde 2-Furoyl Hydrazone. **Journal of Chemical Crystallography**, v. 53, n. 1, p. 8–15, 2023. Available at: < <https://doi.org/10.1007/s10870-022-00955-z> >.

CUKIERMAN, D. S. *et al.* A moderate metal-binding hydrazone meets the criteria for a bioinorganic approach towards Parkinson's disease: Therapeutic potential, blood-brain barrier crossing evaluation and preliminary toxicological studies. **Journal of Inorganic Biochemistry**, v. 170, p. 160–168, 2017. Available at: < <https://doi.org/10.1016/j.jinorgbio.2017.02.020> >.

CUKIERMAN, D. S., REY, N. A. Tridentate N-Acylhydrazones as Moderate Ligands for the Potential Management of Cognitive Decline Associated With Metal-Enhanced Neuroaggregopathies. **Frontiers in Neurology**, v. 13, p. 828654, 2022. Available at: < <https://doi.org/10.3389/fneur.2022.828654> >.

CUKIERMAN D. S. **Physico-chemical optimization and Structure-Activity Relationship studies of aldehyde-derived N-acylhydrazones: towards the improvement of moderate metal chelators as a strategy against metal-enhanced aggregopathies.** Rio de Janeiro, 2021. 218p. Thesis (Doctorate in Chemistry) - Chemistry department, Pontifical Catholic University of Rio de Janeiro.

DE FALCO, A. *et al.* Doença de Alzheimer: Hipóteses etiológicas e perspectivas de tratamento. **Química Nova**, v. 39, n. 1, p. 63–80, 2016. Available at: < <https://doi.org/10.5935/0100-4042.20150152> >.

DE FALCO, A. *et al.* The aroylhydrazone INHHQ prevents memory impairment induced by Alzheimer's-linked amyloid- β oligomers in mice. **Behavioural Pharmacology**, v. 31, n. 8, p. 738–747, 2020. Available at: < <https://doi.org/10.1097/FBP.0000000000000578> >.

DE FELICE, F. G., GONÇALVES, R. A., FERREIRA, S. T. Impaired insulin signalling and allostatic load in Alzheimer disease. **Nature Reviews Neuroscience**, v. 23, n. 4, p. 215-230, 2022. Available at: < <https://doi.org/10.1038/s41583-022-00558-9> >.

DE FREITAS, L. V. *et al.* Structural and vibrational study of 8-hydroxyquinoline-2-carboxaldehyde isonicotinoyl hydrazone - A potential metal-protein attenuating compound (MPAC) for the treatment of Alzheimer's disease. **Spectrochimica Acta - Part A: Molecular and Biomolecular Spectroscopy**, v. 116, p. 41–48, dec. 2013. Available at: < <https://doi.org/10.1016/j.saa.2013.06.105> >.

DE LA MONTE, S. M., WANDS, J. R. Alzheimer's disease is type 3 diabetes-evidence reviewed. **Journal of Diabetes Science and Technology**, v. 2, n. 6, p. 1101–1113, 2008. Available at: < <https://doi.org/10.1177/193229680800200619> >.

DORLET, P. *et al.* Pulse EPR spectroscopy reveals the coordination sphere of copper(II) Ions in the 1-16 amyloid- β peptide: A key role of the first two N-terminus residues. **Angewandte Chemie - International Edition**, v. 48, n. 49, p. 9273–9276, 23 nov. 2009. Available at: < <https://doi.org/10.1002/anie.200904567> >.

EATON, J. W., QIAN, M. Interactions of copper with glycated proteins: Possible involvement in the etiology of diabetic neuropathy. **Molecular and Cellular Biochemistry**, v. 234, p. 135-142, 2002. Available at: < <https://doi.org/10.1023/A%3A1015988817587> >.

ELIASSON B., TASKINEN M. R., SMITH U. Long-term use of nicotine gum is associated with hyperinsulinemia and insulin resistance. **Circulation**, v. 94, n. 5, p. 878–881, 1996. Available at: < <https://doi.org/10.1161/01.cir.94.5.878> >.

EMAMI, S. *et al.* Synthesis, in silico, in vitro and in vivo evaluations of isatin aroylhydrazones as highly potent anticonvulsant agents. **Bioorganic Chemistry**, v. 112, p. 104943, jul. 2021. Available at: < <https://doi.org/10.1016/j.bioorg.2021.104943> >.

FAGERSTRÖM, K. Nicotine: Pharmacology, toxicity and therapeutic use. **Journal of Smoking Cessation**, v. 9, n. 2, p. 53–59, 2013. Available at: < <https://doi.org/10.1017/jsc.2014.27> >.

FALCÃO, A. S. **Agregação e formação de amilóides por proteínas neuroinflamatórias S100A8 e S100A9 e implicações em processos neurodegenerativos.** Lisboa, 2015. 69p. Dissertation (Masters in Biochemistry) – College of Sciences and Technology, New University of Lisboa.

FALLER, P., HUREAU, C. Bioinorganic chemistry of copper and zinc ions coordinated to amyloid- β peptide. **Dalton Transactions**, n. 7, p. 1080–1094, 2009. Available at: < <https://doi.org/10.1039/b813398k> >.

FREUDE, S. *et al.* Neuronal IGF-1 resistance reduces A β accumulation and protects against premature death in a model of Alzheimer's disease. **The FASEB Journal**, v. 23, n. 10, p. 3315–3324, 2009. Available at: < <https://doi.org/10.1096/fj.09-132043> >.

GASPARINI, L. *et al.* Stimulation of beta-amyloid precursor protein trafficking by insulin reduces intraneuronal beta-amyloid and requires mitogen-activated protein kinase signaling. **The Journal of Neuroscience**, v. 21, n. 8, p. 2561–2570, 2001. Available at: < <https://doi.org/10.1523/JNEUROSCI.21-08-02561.2001> >.

GEMBILLO, G. *et al.* Potential Role of Copper in Diabetes and Diabetic Kidney Disease. **Metabolites**, v. 13, n. 1, p. 17, 2023. Available at: < <https://doi.org/10.3390/metabo13010017> >.

GULISANO, W. *et al.* The effect of amyloid- β peptide on synaptic plasticity and memory is influenced by different isoforms, concentrations, and aggregation status. **Neurobiology of Aging**, v. 71, p. 51–60, 2018. Available at: < <https://doi.org/10.1016/j.neurobiolaging.2018.06.025> >.

HALL, D. *et al.* Protein aggregate turbidity: Simulation of turbidity profiles for mixed-aggregation reactions. **Analytical Biochemistry**, v. 498, p. 78–94, 2016. Available at: < <https://doi.org/10.1016/j.ab.2015.11.021> >.

HANE, F., LEONENKO, Z. Effect of metals on kinetic pathways of amyloid- β aggregation. **Biomolecules**, v. 4, n. 1, p. 101–116, 2014. Available at: < <https://doi.org/10.3390/biom4010101> >.

HARTL, F. U. Protein Misfolding Diseases. **Annual Review of Biochemistry**, v. 86, p. 21–26, 2017. Available at: < <https://doi.org/10.1146/annurev-biochem> >.

HASANATO, R. M. W. Trace elements in type 2 diabetes mellitus and their association with glycemic control. **African Health Sciences**, v. 20, n. 1, p. 287–293, 2020. Available at: < <https://doi.org/10.4314/ahs.v20i1.34> >.

HAUSER-DAVIS, R. A. *et al.* Disruption of zinc and copper interactions with A β (1–40) by a non-toxic, isoniazid-derived, hydrazone: A novel biometal homeostasis restoring agent in Alzheimer's disease therapy? **Metallomics**, v. 7, n. 5, p. 743–747, 2015. Available at: < <https://doi.org/10.1039/c5mt00003c> >.

HEPPNER, F. L., RANSOHOFF, R. M., BECHER, B. Immune attack: The role of inflammation in Alzheimer disease. **Nature Reviews Neuroscience**, v. 16, n. 6, p. 358–372, 2015. Available at: < <https://doi.org/10.1038/nrn3880> >.

HUANG, Y. R., LIU, R. T. The toxicity and polymorphism of β -amyloid oligomers. **International Journal of Molecular Sciences**, v. 21, n. 12, p. 1–19, 2020. Available at: < <https://doi.org/10.3390/ijms21124477> >.

HULL, R. L. *et al.* Islet amyloid: A critical entity in the pathogenesis of type 2 diabetes. **Journal of Clinical Endocrinology and Metabolism**, v. 89, n. 8, p. 3629–3643, 2004. Available at: < <https://doi.org/10.1210/jc.2004-0405> >.

IDF Diabetes Atlas. International Diabetes Federation, 2021. 10th edition. Available at: < www.diabetesatlas.org >. Accessed on: January 2024.

JÚNIOR, Á. *et al.* Doença de alzheimer no Distrito Federal e Brasil: reflexos do envelhecimento populacional e da pandemia. **Revista Eletrônica Acervo Saúde**, v. 24, n. 1, p. e14634, 2024. Available at: < <https://doi.org/10.25248/reas.e14634.2024> >.

KABIR, M. T. *et al.* Molecular Mechanisms of Metal Toxicity in the Pathogenesis of Alzheimer's Disease. **Molecular Neurobiology**, v. 58, n. 1, p. 1–20, 2021. Available at: < <https://doi.org/10.1007/s12035-020-02096-w> >.

KARPENKO, M. N. *et al.* Role of Copper Dyshomeostasis in the Pathogenesis of Parkinson's Disease. **Bulletin of Experimental Biology and Medicine**, v. 164, n. 5, p. 596–600, 2018. Available at: < <https://doi.org/10.1007/s10517-018-4039-4> >.

KAWAHARA, M., KATO-NEGISHI, M., TANAKA, K. Amyloids: Regulators of Metal Homeostasis in the Synapse. **Molecules**, v. 25, n. 6, p. 1441, 2020. Available at: < <https://doi.org/10.3390/molecules25061441> >.

KELLAR, D., CRAFT, S. Brain insulin resistance in Alzheimer's disease and related disorders: mechanisms and therapeutic approaches. **The Lancet Neurology**, v. 19, n. 9, p. 758–766, 2020. Available at: < [https://doi.org/10.1016/S1474-4422\(20\)30231-3](https://doi.org/10.1016/S1474-4422(20)30231-3) >.

KHAN, A. R., AWAN, F. R. Metals in the pathogenesis of type 2 diabetes. **Journal of Diabetes & Metabolic Disorders**, v. 13, n. 16, 2014. Available at: < <https://doi.org/10.1186%2F2251-6581-13-16> >.

KOMMERA, S. P. *et al.* Pramlintide an Adjunct to Insulin Therapy: Challenges and Recent progress in delivery. **Journal of Pharmacology and Experimental Therapeutics**, v. 388, n. 1, p. 81-90, 2024. Available at: < <https://doi.org/10.1124/jpet.123.001679> >.

KOPITO, R. R. Aggresomes, inclusion bodies and protein. **Trends in Cell Biology**, v. 10, n. 12, p. 524-530, 2000. Available at: < [https://doi.org/10.1016/s0962-8924\(00\)01852-3](https://doi.org/10.1016/s0962-8924(00)01852-3) >.

KOWALIK-JANKOWSKA, T. *et al.* Coordination abilities of the 1-16 and 1-28 fragments of beta-amyloid peptide towards copper(II) ions: a combined potentiometric and spectroscopic study. **Journal of Inorganic Biochemistry**, v. 95, n. 4, p. 270–282, 2003. Available at: < [https://doi.org/10.1016/S0162-0134\(03\)00128-4](https://doi.org/10.1016/S0162-0134(03)00128-4) >.

KŘÍŽ, Z. *et al.* How Ionic Strength Affects the Conformational Behavior of Human and Rat Beta Amyloids - A Computational Study. **PLOS ONE**, v. 8, n. 5, p. e62914, 2013. Available at: < <https://doi.org/10.1371/journal.pone.0062914> >.

LACOR, P. N. *et al.* Synaptic targeting by Alzheimer's-related amyloid β oligomers. **Journal of Neuroscience**, v. 24, n. 45, p. 10191–10200, 2004. Available at: < <https://doi.org/10.1523/JNEUROSCI.3432-04.2004> >.

LANNFELT, L. *et al.* Safety, efficacy, and biomarker findings of PBT2 in targeting Abeta as a modifying therapy for Alzheimer's disease: a phase IIa, double-blind, randomised, placebo-controlled trial. **The Lancet Neurology**, v. 7, n. 4, p. 779–786, 2008. Available at: < [https://doi.org/10.1016/s1474-4422\(08\)70167-4](https://doi.org/10.1016/s1474-4422(08)70167-4) >.

LEE, S. J. C. *et al.* Structure and assembly mechanisms of toxic human islet amyloid polypeptide oligomers associated with copper. **Chemical Science**, v. 7, n. 8, p. 5398–5406, 2016. Available at: < <https://doi.org/10.1039/c6sc00153j> >.

LEE, S. J. C. *et al.* Towards an understanding of amyloid- β oligomers: characterization, toxicity mechanisms, and inhibitors. **Chemical Society Reviews**, v. 46, n. 2, p. 310–323, 2017. Available at: < <https://doi.org/10.1039/c6cs00731g> >.

LEESON, P. D., YOUNG, R. J. Molecular Property Design: Does Everyone Get It? **ACS Medicinal Chemistry Letters**, v. 6, n. 7, p. 722–725, 2015. Available at: < <https://doi.org/10.1021/acsmchemlett.5b00157> >.

LI, S. *et al.* Decoding the synaptic dysfunction of bioactive human AD brain soluble A β to inspire novel therapeutic avenues for Alzheimer's disease. **Acta Neuropathologica Communications**, v. 6, n. 1, p. 121, 2018. Available at: < <https://doi.org/10.1186/s40478-018-0626-x> >.

LIPINSKI, C. A. *et al.* Experimental and computational approaches to estimate solubility and permeability in drug discovery and development settings. **Advanced Drug Delivery Reviews**, v. 46, p. 3–26, 2001. Available at: < [https://doi.org/10.1016/s0169-409x\(00\)00129-0](https://doi.org/10.1016/s0169-409x(00)00129-0) >.

LOPES DE ANDRADE, V., MARREILHA DOS SANTOS, A. P., ASCHNER, M. Neurotoxicity of metal mixtures. **Advances in Neurotoxicology**, v. 5, p. 329–364, 2021. Available at: < <https://doi.org/10.1016/bs.ant.2020.12.003> >.

LOWE, J., TAVEIRA-DA-SILVA, R., HILÁRIO-SOUZA, E. Dissecting copper homeostasis in diabetes mellitus. **IUBMB Life**, v. 69, n. 4, p. 255–262, 2017. Available at: < <https://doi.org/10.1002/iub.1614> >.

LV, Z., GUO, Y. Metformin and Its Benefits for Various Diseases. **Frontiers in Endocrinology**, v. 11, p. 191, apr. 2020. Available at: < <https://doi.org/10.3389/fendo.2020.00191> >.

LYSSENKO, V. *et al.* Clinical Risk Factors, DNA Variants, and the Development of Type 2 Diabetes. **The New England Journal of Medicine**, v. 359, n. 21, p. 2220–2232, 2008. Available at: < <https://doi.org/10.1056/nejmoa0801869> >.

MAHLER, H. C. *et al.* Protein aggregation: pathways, induction factors and analysis. **Journal of Pharmaceutical Sciences**, v. 98, n. 9, p. 2909–2934, 2009. Available at: < <https://doi.org/10.1002/jps.21566> >.

MAKOWSKI G. S. **Advances in Clinical Chemistry**. First edition. United States: Academic Press, 2009. Available at: < <https://search.library.wisc.edu/catalog/9912368247902121> >.

MARCATTI, M. *et al.* A β /tau oligomer interplay at human synapses supports shifting therapeutic targets for Alzheimer's disease. **Cellular and Molecular Life Sciences**, v. 79, n. 4, p. 222, 2022. Available at: < <https://doi.org/10.1007/s00018-022-04255-9> >.

MARÍN-PENÁLVOR, J. J. *et al.* Update on the treatment of type 2 diabetes mellitus. **World Journal of Diabetes**, v. 7, n. 17, p. 354-395, 2016. Available at: < <https://doi.org/10.4239/wjd.v7.i17.354> >.

MATTHEWS, D. R. *et al.* Glycaemic durability of an early combination therapy with vildagliptin and metformin versus sequential metformin monotherapy in newly diagnosed type 2 diabetes (VERIFY): a 5-year, multicentre, randomised, double-blind trial. **The Lancet**, v. 394, n. 10208, p. 1519–1529, 2019. Available at: < [https://doi.org/10.1016/S0140-6736\(19\)32131-2](https://doi.org/10.1016/S0140-6736(19)32131-2) >.

MAURER, K., VOLK, S., GERBALDO, H. Auguste D and Alzheimer's disease. **The Lancet**, v. 349, n. 9064, p. 1546-1549, 24 may 1997. Available at: < [https://doi.org/10.1016/S0140-6736\(96\)10203-8](https://doi.org/10.1016/S0140-6736(96)10203-8) >.

MAY, N. V., JANCSÓ, A., ENYEDY, É. A. Binding Models of Copper(II) Thiosemicarbazone Complexes with Human Serum Albumin: A Speciation Study. **Molecules**, v. 26, n. 9, p. 2711, 5 may 2021. Available at: < <https://doi.org/10.3390/molecules26092711> >.

MENG, F. *et al.* Amyloid formation by pro-islet amyloid polypeptide processing intermediates: examination of the role of protein heparan sulfate interactions and implications for islet amyloid formation in type 2 diabetes. **Biochemistry**, v. 46, n. 43, p. 12091–12099, 30 oct. 2007. Available at: < <https://doi.org/10.1021/bi7004834> >.

METAXAS, A. Imbalances in Copper or Zinc Concentrations Trigger Further Trace Metal Dyshomeostasis in Amyloid-Beta Producing *Caenorhabditis elegans*. **Frontiers in Neuroscience**, v. 15, p. 755475, oct. 2021. Available at: < <https://doi.org/10.3389/fnins.2021.755475> >.

MITCHELL, B. L. *et al.* Exploring the genetic relationship between hearing impairment and Alzheimer's disease. **Alzheimer's and Dementia: Diagnosis, Assessment and Disease Monitoring**, v. 12, n. 1, p. e12108, 2020. Available at: < <https://doi.org/10.1002/dad2.12108> >.

MORALES, I. G., FARÍAS, G. G., MACCIONI, R. R. B. La neuroinflamación como factor detonante del desarrollo de la enfermedad de Alzheimer. **Revista chilena de neuro-psiquiatría**, v. 48, n. 1, p. 49-57, mar. 2010. Available at: < <http://dx.doi.org/10.4067/S0717-92272010000200007> >.

NAKA T. *et al.* Association of serum copper levels and glycemic control in patients with type 2 diabetes. **Endocrine Journal**, v. 60, n. 3, p. 393–396, 2013. Available at: < <https://doi.org/10.1507/endocrj.ej12-0342> >.

NGUYEN, T. T. *et al.* Role of Insulin Resistance in the Alzheimer's Disease Progression. **Neurochemical Research**, v. 45, n. 7, p. 1481–1491, 2020. Available at: < <https://doi.org/10.1007/s11064-020-03031-0> >.

NGUYEN, T. T. *et al.* Type 3 Diabetes and Its Role Implications in Alzheimer's Disease. **International Journal of Molecular Sciences**, v. 21, n. 9, p. 3165, 2020. Available at: < <https://doi.org/10.3390/ijms21093165> >.

OCHIISHI, T. *et al.* New Alzheimer's disease model mouse specialized for analyzing the function and toxicity of intraneuronal Amyloid β oligomers. **Scientific Reports**, v. 9, n. 1, p. 17368, 2019. Available at: < <https://doi.org/10.1038/s41598-019-53415-8> >.

OPIE, E. L. THE RELATION OF DIABETES MELLITUS TO LESIONS OF THE PANCREAS. HYALINE DEGENERATION OF THE ISLANDS OF LANGERHANS. **Journal of Experimental Medicine**, v. 5, n. 5, p. 527-540, 1901. Available at: < <https://doi.org/https://doi.org/10.1084/jem.5.5.527> >.

PAJOUHESH, H., LENZ, G. R. Medicinal Chemical Properties of Successful Central Nervous System Drugs. **NeuroRx**, v. 2, n. 4, p. 541-553, 2005. Available at: < <https://doi.org/10.1602/neurorx.2.4.541> >.

PALLA G. *et al.* Conformational behaviour and E/Z isomerization of N-acyl and N-aroylhydrazones. **Tetrahedron**, v. 42, n. 13, p. 3649–3654, 1986. Available at: < [https://doi.org/https://doi.org/10.1016/S0040-4020\(01\)87332-4](https://doi.org/https://doi.org/10.1016/S0040-4020(01)87332-4) >.

PAPPALARDO, G. *et al.* Environmental factors differently affect human and rat IAPP: Conformational preferences and membrane interactions of IAPP17-29 peptide derivatives. **Chemistry - A European Journal**, v. 13, n. 36, p. 10204–10215, 2007. Available at: < <https://doi.org/10.1002/chem.200700576> >.

PARK, C. R. *et al.* Intracerebroventricular insulin enhances memory in a passive-avoidance task. **Physiology & Behavior**, v. 68, n. 4, p. 509–514, 2000. Available at: < [https://doi.org/10.1016/s0031-9384\(99\)00220-6](https://doi.org/10.1016/s0031-9384(99)00220-6) >.

PARK, K. *et al.* Oxidative stress and insulin resistance: The Coronary Artery Risk Development in Young Adults study. **Diabetes Care**, v. 32, n. 7, p. 1302–1307, 2009. Available at: < <https://doi.org/10.2337/dc09-0259> >.

PARTHASARATHY, S. *et al.* Capturing a reactive state of amyloid aggregates: NMR-BASED CHARACTERIZATION OF COPPER-BOUND ALZHEIMER DISEASE AMYLOID B-FIBRILS IN A REDOX CYCLE. **Journal of Biological**

Chemistry, v. 289, n. 14, p. 9998–10010, 2014. Available at: < <https://doi.org/10.1074/jbc.M113.511345> >.

PATEL, A. N., JHAMANDAS, J. H. Neuronal receptors as targets for the action of amyloid-beta protein (A β) in the brain. **Expert Reviews in Molecular Medicine**, v. 14, p. e2, 2012. Available at: < <https://doi.org/10.1017/S1462399411002134> >.

PAULSSON, J. F. *et al.* Intracellular amyloid-like deposits contain unprocessed pro-islet amyloid polypeptide (proIAPP) in beta cells of transgenic mice overexpressing the gene for human IAPP and transplanted human islets. **Diabetologia**, v. 49, n. 6, p. 1237–1246, 2006. Available at: < <https://doi.org/10.1007/s00125-006-0206-7> >.

PEDROZO-PENAFIEL, M. J. *et al.* Square Wave Voltammetric Determination of 8-Hydroxyquinoline-2-Carboxaldehyde Isonicotinoyl Hydrazone (INHHQ), a Promising Metal-Protein Attenuating Compound for the Treatment of Alzheimer's Disease, Using a Multiwalled Carbon Nanotube (MWCNT) Modified Glassy Carbon Electrode (GCE). **Analytical Letters**, v. 53, n. 14, p. 2337–2354, 2020. Available at: < <https://doi.org/10.1080/00032719.2020.1741603> >.

PILKINGTON, E. H. *et al.* Pancreatic β -Cell Membrane Fluidity and Toxicity Induced by Human Islet Amyloid Polypeptide Species. **Scientific Reports**, v. 6, p. 21274, 2016. Available at: < <https://doi.org/10.1038/srep21274> >.

DEL PRATO, S., BIANCHI, C., DANIELE, G. **Textbook of Diabetes**. Fifth Edition. Pisa: Wiley Blackwell, 2017. Available at: < <https://search.library.wisc.edu/catalog/9912654346202121> >.

PRZYGONSKA, K. *et al.* His6, His13, and His14 residues in A β 1–40 peptide significantly and specifically affect oligomeric equilibria. **Scientific Reports**, v. 9, n. 1, p. 9449, 2019. Available at: < <https://doi.org/10.1038/s41598-019-45988-1> >.

QIU, Q. *et al.* Copper in Diabetes Mellitus: a Meta-Analysis and Systematic Review of Plasma and Serum Studies. **Biological Trace Element Research**, v. 177, n. 1, p. 53–63, 2017. Available at: < <https://doi.org/10.1007/s12011-016-0877-y> >.

QUINTANAR, L., LIM, M. H. Metal ions and degenerative diseases. **Journal of Biological Inorganic Chemistry**, v. 24, n. 8, p. 1137–1139, 2019. Available at: < <https://doi.org/10.1007/s00775-019-01744-4> >.

RADOVIĆ-JANOŠEVIĆ, D. *et al.* ANEMIA IN GYNECOLOGY AND PERINATOLOGY – NEW ATTITUDES. **Acta Medica Medianae**, v. 59, n. 3, p. 84–89, 2020. Available at: < <https://doi.org/10.5633/amm.2020.0311> >.

RAIMUNDO, A. F. *et al.* Islet Amyloid Polypeptide: A Partner in Crime With A β in the Pathology of Alzheimer's Disease. **Frontiers in Molecular Neuroscience**, v. 13, p. 35, 2020. Available at: < <https://doi.org/10.3389/fnmol.2020.00035> >.

RANA, M., SHARMA, A. K. Cu and Zn interactions with A β peptides: consequence of coordination on aggregation and formation of neurotoxic soluble A β oligomers. **Metallomics**, v. 11, n. 1, p. 64–84, 2019. Available at: < <https://doi.org/10.1039/c8mt00203g> >.

RIVILLAS-ACEVEDO, L. *et al.* Structural basis for the inhibition of truncated islet amyloid polypeptide aggregation by Cu(II): Insights into the bioinorganic chemistry of type II diabetes. **Inorganic Chemistry**, v. 54, n. 8, p. 3788–3796, 2015. Available at: < <https://doi.org/10.1021/ic502945k> >.

ROWLES, J. E. *et al.* Are heat shock proteins an important link between type 2 diabetes and alzheimer disease? **International Journal of Molecular Sciences**, v. 21, n. 21, p. 1–20, 2020. Available at: < <https://doi.org/10.3390/ijms21218204> >.

RYAN, G., BRISCOE, T. A., JOBE, L. Review of pramlintide as adjunctive therapy in treatment of type 1 and type 2 diabetes. **Drug Design, Development and Therapy**, v. 2, p. 203-214, 2008. Available at: < <https://doi.org/10.2147%2Fdddt.s3225> >.

SÁNCHEZ-LÓPEZ, C. *et al.* Copper Coordination Features of Human Islet Amyloid Polypeptide: The Type 2 Diabetes Peptide. **Inorganic Chemistry**, v. 55, n. 20, p. 10727–10740, 2016. Available at: < <https://doi.org/10.1021/acs.inorgchem.6b01963> >.

SCHNURR, T. M. *et al.* Obesity, unfavourable lifestyle and genetic risk of type 2 diabetes: a case-cohort study. **Diabetologia**, v. 63, n. 7, p. 1324–1332, 2020. Available at: < <https://doi.org/10.1007/s00125-020-05140-5> >.

SCHWARTZ, M. W., PORTE, D. Diabetes, obesity, and the brain. **Science**, v. 307, n. 5708, p. 375–379, 2005. Available at: < <https://doi.org/10.1126/science.1104344> >.

SCOTT, L. E., ORVIG, C. Medicinal inorganic chemistry approaches to passivation and removal of aberrant metal ions in disease. **Chemical Reviews**, v. 109, n. 10, p. 4885–4910, 2009. Available at: < <https://doi.org/10.1021/cr9000176> >.

SELKOE, D. J., HARDY, J. The amyloid hypothesis of Alzheimer's disease at 25 years. **EMBO Molecular Medicine**, v. 8, n. 6, p. 595–608, 2016. Available at: < <https://doi.org/10.15252/emmm.201606210> >.

SHARMA, A. K. *et al.* The effect of Cu²⁺ and Zn²⁺ on the A β ₄₂ peptide aggregation and cellular toxicity. **Metallomics**, v. 5, n. 11, p. 1529–1536, 2013. Available at: < <https://doi.org/10.1039/c3mt00161j> >.

SILVA, T. M. D. *et al.* Internação hospitalar de idosos por Doença de Alzheimer no Brasil, e custo associado: estudo ecológico. **Saúde e Pesquisa**, v. 16, n. 2, p. 1–13, 2023. Available at: < <https://doi.org/10.17765/2176-9206.2023v16n2.e11397> >.

SMITH, D. P. *et al.* Copper-mediated amyloid- β toxicity is associated with an intermolecular histidine bridge. **Journal of Biological Chemistry**, v. 281, n. 22, p. 15145–15154, 2006. Available at: < <https://doi.org/10.1074/jbc.M600417200> >.

SOREGHAN, B., KOSMOSKI, J., GLABE, C. Surfactant Properties of Alzheimer's A β Peptides and the Mechanism of Amyloid Aggregation*. **The Journal of Biological Chemistry**, v. 269, n. 46, p. 28551-28554, 1994. Available at: < [https://doi.org/10.1016/S0021-9258\(19\)61939-3](https://doi.org/10.1016/S0021-9258(19)61939-3) >.

STEEN, E. *et al.* Impaired insulin and insulin-like growth factor expression and signaling mechanisms in Alzheimer's disease – is this type 3 diabetes? **Journal of Alzheimer's Disease**, v. 7, n. 1, p. 63–80, 2005. Available at: < <https://doi.org/10.3233/jad-2005-7107> >.

STEFANIAK, E. *et al.* The Aggregation Pattern of A β 1–40 is Altered by the Presence of N-Truncated A β 4–40 and/or CuII in a Similar Way through Ionic Interactions. **Chemistry A European Journal**, v. 27, n. 8, p. 2798–2809, 2021. Available at: < <https://doi.org/10.1002/chem.202004484> >.

STELZMANN, R. A., SCHNITZLEIN H. N., MURTAGH, F. R. An English Translation of Alzheimer's 1907 Paper, "Über eine eigenartige Erkrankung der Hirnrinde." **Clinical Anatomy**, v. 8, p. 429-431, 1995. Available at: < <https://doi.org/10.1002/ca.980080612> >.

STORK, C. M., SCHREFFLER, S. M., WEXLER, P. **Encyclopedia of Toxicology**. Third Edition. London: Academic Press, 2014. Available at: < <https://search.library.wisc.edu/catalog/9913779129002121> >.

SYME, C. D. *et al.* Copper binding to the amyloid- β ($\text{a}\beta$) peptide associated with Alzheimer's disease: Folding, coordination geometry, pH dependence, stoichiometry, and affinity of A β -(1-28): insights from a range of complementary spectroscopic techniques. **Journal of Biological Chemistry**, v. 279, n. 18, p. 18169–18177, 2004. Available at: < <https://doi.org/10.1074/jbc.M313572200> >.

THEILLET, F. X. *et al.* Physicochemical properties of cells and their effects on intrinsically disordered proteins (IDPs). **Chemical Reviews**, v. 114, n. 13, p. 6661–6714, 2014. Available at: < <https://doi.org/10.1021/cr400695p> >.

TISOVSKÝ, P. *et al.* Effect of a =X-NH-Fragment, (X = C, N), on Z/E Isomerization and ON/OFF Functionality of Isatin Arylhydrazones, ((Arylamino)Methylene)Indolin-2-Ones and Their Anions. **Molecules**, v. 25, n. 13, p. 3082, 2020. Available at: < <https://doi.org/10.3390/molecules25133082> >.

TOMASELLO, M. F., SINOPOLI, A., PAPPALARDO, G. On the Environmental Factors Affecting the Structural and Cytotoxic Properties of IAPP Peptides. **Journal of Diabetes Research**, v. 2015, p. 918573, 2015. Available at: < <https://doi.org/10.1155/2015/918573> >.

TOMIZAWA, M., CASIDA, J. E. Neonicotinoid insecticide toxicology: Mechanisms of selective action. **Annual Review of Pharmacology and**

Toxicology, v. 45, p. 247–268, 2005. Available at: < <https://doi.org/10.1146/annurev.pharmtox.45.120403.095930> >.

TRIPATHY, D., CHAVEZ, A. O. Defects in insulin secretion and action in the pathogenesis of type 2 diabetes mellitus. **Current Diabetes Reports**, v. 10, n. 3, p. 184–191, 2010. Available at: < <https://doi.org/10.1007/s11892-010-0115-5> >.

TUOMI, T. *et al.* The many faces of diabetes: A disease with increasing heterogeneity. **The Lancet**, v. 383, n. 9922, p. 1084–1094, 2014. Available at: < [https://doi.org/10.1016/S0140-6736\(13\)62219-9](https://doi.org/10.1016/S0140-6736(13)62219-9) >.

VADUKUL, D. M. *et al.* Internalisation and toxicity of amyloid- β 1-42 are influenced by its conformation and assembly state rather than size. **FEBS Letters**, v. 594, n. 21, p. 3490–3503, 2020. Available at: < <https://doi.org/10.1002/1873-3468.13919> >.

VAN DE WATERBEEMD, H. *et al.* Estimation of blood-brain barrier crossing of drugs using molecular size and shape, and H-bonding descriptors. **Journal of Drug Targeting**, v. 6, n. 2, p. 151-165, 1998. Available at: < <https://doi.org/10.3109/10611869808997889> >.

VERMA, M., VATS, A., TANEJA, V. Toxic species in amyloid disorders: Oligomers or mature fibrils. **Annals of Indian Academy of Neurology**, v.18, n. 2, p. 138–145, 2015. Available at: < <https://doi.org/10.4103/0972-2327.144284> >.

VILAR, M. *et al.* The fold of α -synuclein fibrils. **Annals of Indian Academy of Neurology**, v.105, n. 25, p. 8637-8642, 2008. Available at: < <https://doi.org/10.1073/pnas.0712179105> >.

VILLEMAGNE, V. L. *et al.* A randomized, exploratory molecular imaging study targeting amyloid β with a novel 8-OH quinoline in Alzheimer's disease: The PBT2-204 IMAGINE study. **Alzheimer's & Dementia: Translational Research & Clinical Interventions**, v.3, n. 4, p. 622–635, nov. 2017. Available at: < <https://doi.org/10.1016/j.trci.2017.10.001> >.

WANG, L. *et al.* Current understanding of metal ions in the pathogenesis of Alzheimer's disease. **Translational Neurodegeneration**, v.9, p. 10, 2020. Available at: < <https://doi.org/10.1186/s40035-020-00189-z> >.

WANG, W. *et al.* Toxic amyloid- β oligomers induced self-replication in astrocytes triggering neuronal injury. **EBioMedicine**, v.42, p. 174–187, 2019. Available at: < <https://doi.org/10.1016/j.ebiom.2019.03.049> >.

WANG, W., NEMA, S., TEAGARDEN, D. Protein aggregation-Pathways and influencing factors. **International Journal of Pharmaceutics**, v.390, n. 2, p. 89–99, 2010. Available at: < <https://doi.org/10.1016/j.ijpharm.2010.02.025> >.

WEILAND S., BERTRAND D., LEONARD S. Neuronal nicotinic acetylcholine receptors: from the gene to the disease. **Behavioural Brain Research**, v. 113, p. 43–56, 2000. Available at: < [https://doi.org/10.1016/s0166-4328\(00\)00199-6](https://doi.org/10.1016/s0166-4328(00)00199-6) >.

WESTERMARK, P., ANDERSSON, A., WESTERMARK, G. T. Islet amyloid polypeptide, islet amyloid, and diabetes mellitus. **Physiological Reviews**, v. 91, n. 3, p. 795–826, 2011. Available at: < <https://doi.org/10.1152/physrev.00042.2009> >.

WESTERMARK, P. *et al.* A NOVEL PEPTIDE IN THE CALCITONIN GENE RELATED PEPTIDE FAMILY AS AN AMYLOID FIBRIL PROTEIN IN THE ENDOCRINE PANCREAS. **Biochemical and Biophysical Research Communications**, v. 140, n. 3, p. 827-831, 1986. Available at: < [https://doi.org/10.1016/0006-291x\(86\)90708-4](https://doi.org/10.1016/0006-291x(86)90708-4) >.

WHITE, A. R. *et al.* The Alzheimer's Disease Amyloid Precursor Protein Modulates Copper-Induced Toxicity and Oxidative Stress in Primary Neuronal Cultures. **The Journal of Neuroscience**, v. 19, n. 21, p. 9170-9179, 1999. Available at: < <https://doi.org/10.1523/jneurosci.19-21-09170.1999> >.

WOOD C. M., FARRELL A. P., BRAUNER C. J. **Homeostasis and Toxicology of Essential Metals**. First edition. Canada: Academic Press, 2012. Available at: < <https://search.library.wisc.edu/catalog/9910109856002121> >.

XIONG, L. L. *et al.* Single-cell RNA sequencing reveals B cell-related molecular biomarkers for Alzheimer's disease. **Experimental and Molecular Medicine**, v. 53, n. 12, p. 1888–1901, 2021. Available at: < <https://doi.org/10.1038/s12276-021-00714-8> >.

YAKUPOVA, E. I. *et al.* Congo Red and amyloids: History and relationship. **Bioscience Reports**, v. 39, n. 1, 2019. Available at: < <https://doi.org/10.1042/BSR20181415> >.

YIANNIKOURIDES, A., LATUNDE-DADA, G. O. A Short Review of Iron Metabolism and Pathophysiology of Iron Disorders. **Medicines**, v. 6, n. 3, p. 85, 2019. Available at: < <https://doi.org/10.3390/medicines6030085> >.

YIANNOPOULOU, K. G., PAPAGEORGIOU, S. G. Current and Future Treatments in Alzheimer Disease: An Update. **Journal of Central Nervous System Disease**, v. 12, p. 1-12, 2020. Available at: < <https://doi.org/10.1177/1179573520907397> >.

YOSHIKAWA, H., HELLSTRÖM-LINDAHL, E., GRILL, V. Evidence for functional nicotinic receptors on pancreatic β cells. **Metabolism: Clinical and Experimental**, v. 54, n. 2, p. 247–254, 2005. Available at: < <https://doi.org/10.1016/j.metabol.2004.08.020> >.

YU, Y. P. *et al.* Copper-induced cytotoxicity: Reactive oxygen species or islet amyloid polypeptide oligomer formation. **Chemical Communications**, v. 46, n. 37, p. 6909–6911, 2010. Available at: < <https://doi.org/10.1039/c0cc02141e> >.

ZAPADKA, K. L. *et al.* Factors affecting the physical stability (aggregation) of peptide therapeutics. **Interface Focus**, v. 7, n. 6, 2017. Available at: < <https://doi.org/10.1098/rsfs.2017.0030> >.

ZHANG, Y. *et al.* (2002). Selective cytotoxicity of intracellular amyloid beta peptide1-42 through p53 and Bax in cultured primary human neurons. **Journal of Cell Biology**, v. 156, n. 3, p. 519–529, 2002. Available at: < <https://doi.org/10.1083/jcb.200110119> >.



New mescaline-related *N*-acylhydrazone and its unsubstituted benzoyl derivative: Promising metallophores for copper-associated deleterious effects relief in Alzheimer's disease

Alessandra Carvalho^a, Barbara Marinho Barbosa^a, Jesica S. Flores^b, Phelippe do Carmo Gonçalves^b, Renata Diniz^c, Yraima Cordeiro^d, Claudio O. Fernández^b, Daphne S. Cukierman^{a,d}, Nicolás A. Rey^{a,*}

^a Department of Chemistry, Pontifical Catholic University of Rio de Janeiro (PUC-Rio), Rio de Janeiro 22451-900, Brazil

^b Max Planck Laboratory for Structural Biology, Chemistry and Molecular Biophysics of Rosario (MPLbioR, UNR-MPINAT), Partner Laboratory of the Max Planck Institute for Multidisciplinary Sciences (MPINAT, MPG), Centro de Estudios Interdisciplinarios, Universidad Nacional de Rosario, Rosario S2002LRK, Argentina

^c Department of Chemistry, ICEX, Universidade Federal de Minas Gerais (UFMG), Belo Horizonte 31270-901, Brazil

^d Faculty of Pharmacy, CCS, Universidade Federal do Rio de Janeiro (UFRJ), Rio de Janeiro 21941-902, Brazil

ARTICLE INFO

Keywords:

Mescaline
N-acylhydrazones
 Copper(II)
 Metallophores
 ROS
 Alzheimer's disease

ABSTRACT

Alzheimer's disease (AD) is related to the presence of extracellular aggregated amyloid- β peptide ($A\beta$), which binds copper(II) with high affinity in its N-terminal region. In this sense, two new 1-methylimidazole-containing *N*-acylhydrazone metallophores, namely, **X1TMP** and **X1Benz**, were synthesized as hydrochlorides and characterized. The compound **X1TMP** contains the 3,4,5-trimethoxybenzoyl moiety present in the structure of mescaline, a natural hallucinogenic protoalkaloid that occurs in some species of cacti. Single crystals of **X1Benz**, the unsubstituted derivative of **X1TMP**, were obtained. The experimental partition coefficients of both compounds were determined, as well as their apparent affinity for Cu^{2+} in aqueous solution. Ascorbate consumption assays showed that these *N*-acylhydrazones are able to lessen the production of ROS by the $Cu(A\beta)$ -system, and a short-time scale aggregation study, measured through turbidity and confirmed by TEM images, revealed their capacity in preventing $A\beta$ fibrillation at equimolar conditions in the presence and absence of copper. $^1H-^{15}N$ HSQC NMR experiments demonstrated a direct interaction between $A\beta$ and **X1Benz**, the most soluble of the compounds. The Cu^{2+} sequestering potential of this hydrazone towards $A\beta$ was explored by 1H NMR. Although increasing amounts of **X1Benz** were unexpectedly not efficient at removing the metal-induced perturbations in $A\beta$ backbone amides, the broadening effects observed on the compound's signals indicate the formation of a ternary $A\beta$ -copper-**X1Benz** species, which can be responsible for the observed ROS-lessening and aggregation-preventing activities. Overall, the *N*-acylhydrazones **X1TMP** and **X1Benz** have shown promising prospects as agents for the treatment of AD.

"The man who comes back through the Door in the Wall will never be quite the same as the man who went out."

The Doors of Perception – Aldous Huxley (1894–1963)

1. Introduction

Alzheimer's disease (AD) is the foremost cause of dementia worldwide. This age-related neurodegenerative condition is characterized by

memory loss and impaired cognitive function, as well as by behavioral and personality alterations [1]. These are the results of chronic neuroinflammation and synapse loss, which are thought to be related to activated microglia [2]. From a mechanistic point of view, AD is considered to be the result of an intricate interplay between both genetic and environmental components. Classic neuropathological hallmarks of AD are the presence of different aggregation states of extracellular amyloid- β ($A\beta$) peptide, as oligomers and fibrillar plaques, and intracellular accumulation of neurofibrillary tangles, composed of

* Corresponding author.

E-mail address: nicoarey@puc-rio.br (N.A. Rey).

<https://doi.org/10.1016/j.jinorgbio.2022.112033>

Received 10 August 2022; Received in revised form 3 October 2022; Accepted 15 October 2022

Available online 19 October 2022

0162-0134/© 2022 Elsevier Inc. All rights reserved.

hyperphosphorylated tau protein [3]. Concerning A β , its monomeric forms have been associated with memory consolidation [4]. However, its functional role is limited to low, picomolar physiological concentrations [5]. At the nanomolar range, A β starts to aggregate into toxic oligomers (A β Os) [6]. It is now widely accepted that the formation of soluble oligomeric A β species is the key event in AD pathogenesis [7,8].

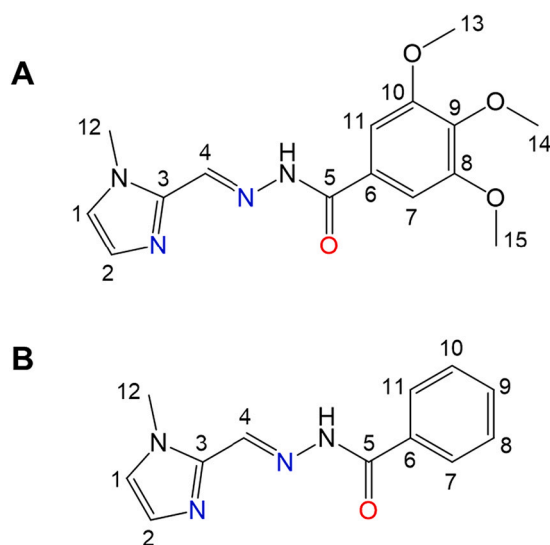
In terms of their bioinorganic chemistry, the A β peptide and its fragments are particularly interesting since they bind biometals with high affinity, especially in the N-terminal region. In the specific case of copper(II), a distorted square-planar geometry is observed, involving, at lower pH values, the amine of Asp1, the carbonyl from Asp1-Ala2 amide bond and imidazole nitrogen atoms from two histidine residues, His6 and His13 or His14 [9,10]. At more basic medium, the nitrogen from Asp1-Ala2 amide bond is deprotonated, and binds copper, along with the terminal Asp1 amine, the carbonyl from the Ala2-Glu3 peptide bond and an imidazole nitrogen from one of the His residues [11].

It has been shown that metal homeostasis is disturbed in the brains of AD patients [12]. Metal ion binding leads to conformational changes in the peptide [13]. Specifically, A β -Cu interactions lead to the formation of toxic oligomeric species [14,15], besides the catalytic production of reactive oxygen species (ROS) [16], which are responsible for the widespread oxidative damage observed in this pathology. Thus, targeting abnormal metal-protein interactions through the use of metallophores, also known as Metal-Protein Attenuating Compounds (MPACs), has become a relevant query in the literature. These are compounds that bind selectively and moderately to copper(II) ions, employed with the goal of preventing A β oligomerization through the competition for *in vivo* binding to this physiological metal, as well as redistributing and normalizing its basal levels, thus restoring homeostasis, and reducing copper-mediated oxidative damage [17].

Over the last decade, our research group has shown the suitability of metallophores belonging to the class of *N*-acylhydrazones as modulators of abnormal metal-protein interactions for a series of metal-enhanced aggregopathies [18–25]. In the context of AD, our lead-compound INHHQ is able to compete *in vitro* with the A β peptide for the binding of copper(II) and zinc(II) [18]. The compound was detected in the brain of Wistar rats after intraperitoneal injection and is non-toxic at high concentrations for these animals [19]. Not long ago we showed that INHHQ is able to prevent A β oligomer-induced memory deficit in Swiss mice, as well as to decrease *in vitro* copper-mediated ROS production [22]. However, INHHQ aqueous solubility is not ideal. In this sense, we have recently pointed to novel 1-methylimidazole-containing *N*-acylhydrazones as a next generation family of compounds with improved pharmacological prospect and as promising agents for the management of neurodegenerative diseases. We have already shown the suitability of the new lead X1INH in synucleinopathies, with implications to Parkinson's disease [23].

In his notorious 1954 best-seller “The Doors of Perception”, the English writer and philosopher Aldous Huxley recounted the controlled experience he had on the use of natural hallucinogenic protoalkaloid mescaline, which occurs in some species of cacti, particularly the one known by the name peyote (*Lophophora williamsii*) [26]. This compound, 3,4,5-trimethoxyphenethylamine, selectively binds and activates brain serotonin receptor 5-HT_{2A} with high affinity [27], acting as a partial agonist. As part of a bioinspired approach aiming to the obtention of metallophores with improved pharmacological properties, we designed a new 1-methylimidazole-containing *N*-acylhydrazone, X1TMP, which contains the trimethoxybenzoyl moiety present in the structure of mescaline. For the sake of comparison, the unsubstituted benzoyl derivative X1Benz was also synthesized (Scheme 1).

Thus, this report intends to evaluate whether the presence of the three methoxyl substituents in X1TMP would impact some pharmacologically relevant parameters such as the partition coefficient, the coordinating ability towards copper(II), and, consequently, the metallophore potential of this *N*-acylhydrazone.



Scheme 1. Structure of (A) 1-methyl-1H-imidazole-2-carboxaldehyde 3,4,5-trimethoxybenzoyl hydrazone (X1TMP) and (B) 1-methyl-1H-imidazole-2-carboxaldehyde benzoyl hydrazone (X1Benz). Potential coordinating atoms are highlighted in color.

2. Materials and methods

2.1. Syntheses and characterization

All reagents and solvents used in this work were purchased from commercial sources in the highest purity available and were employed without further purification.

Ligands were prepared through Schiff base condensations between 1-methyl-2-imidazolecarboxaldehyde (0.110 g, 1.0 mmol) and either 3,4,5-trimethoxybenzoic acid hydrazide (0.226 g, 1.0 mmol), for X1TMP, or benzoic acid hydrazide (0.136 g, 1.0 mmol), for X1Benz, in 10 mL ethanol. Two drops of concentrated HCl were added as catalyst to the mixture, which was kept under reflux for 4 h (Scheme S1, Supplementary Material). The precipitates were isolated through filtration after slow evaporation of the solvent, washed with cold ethanol and dried at room temperature.

1-methyl-1H-imidazole-2-carboxaldehyde 3,4,5-trimethoxybenzoyl hydrazone hydrochloride monohydrate (X1TMP·HCl·H₂O); Yield: 83%; M.p.: 153 ± 2 °C; IR (KBr, cm⁻¹) – main bands (Fig. S1): 3426 (νOH_{water}); 3125 (νNH_{imidazole}⁺); 3105 (νNH); 2965 and 2944 (νCH_{methoxy}); 1664 (νCO_{amide}); 1605 (νCN_{azomethine}); 1552 (skeletal mode, imidazolium cation); 1504 1466 and 1452 (νCC_{benzene}); 1524 and 1418 (coupled νCN / νCC_{imidazole}); 1100 (νNN); 1226 and 1130 (νCO_{methoxy}). ESI-MS(+): *m/z* = 319.30.

1-methyl-1H-imidazole-2-carboxaldehyde benzoyl hydrazone hydrochloride trihydrate (X1Benz·HCl·3H₂O); Yield: 72%; M.p.: 128 ± 1 °C; IR (KBr, cm⁻¹) – main bands (Fig. S2): 3508, 3438 and 3422 (νOH_{water}); 3153 (νNH_{imidazole}⁺); 3102 (νNH_{hydrazone}); 1680 (νCO_{amide}); 1648 (δH₂O); 1619 (νCN_{azomethine}); 1602, 1494 and 1446 (νCC_{benzene}); 1562 and 1557 (skeletal modes, imidazolium cation); 1525, 1481 and 1419 (coupled νCN / νCC_{imidazole}); 1131 (νNN). ESI-MS (+): *m/z* = 229.16.

The mass spectra of X1TMP and X1Benz are displayed in Fig. S3.

The descriptor parameters Molecular Weight, cLog P, cLog S, PSA, Druglikeness and Drug Score were determined with Osiris Property Explorer: DataWarrior™, software freely available for download at <http://www.organic-chemistry.org/prog/peo/>. Melting point determinations were performed in a Fisatom™ model 431 apparatus, in triplicate. Infrared vibrational spectroscopy (IR) was performed in a 100 FT-IR Perkin-Elmer™ spectrophotometer, and the data was collected in the region 4000–400 cm⁻¹. Pellets of the samples were prepared in

potassium bromide. Hydrogen and carbon nuclear magnetic resonance spectra were obtained in a Bruker™ Avance III HD-400 spectrophotometer at 25 °C. *N*-acylhydrazones were dissolved in 0.6 mL of deuterated dimethylsulfoxide (DMSO-*d*₆) and the spectra, calibrated based on the residual solvent signal (quintet at 2.50 ppm for ¹H and septet at 39.52 for ¹³C). Electrospray ionization mass spectrometry [ESI-MS(+)] analyses were collected on a Perkin-Elmer SQ-300 mass spectrometer. Stock solutions of the samples were prepared by dissolving 1.0 mg of the ligands in 1.0 mL of methanol. Aliquots of 20 μL of these solutions were diluted in 980 μL of methanol and analyzed by direct infusion. Standard configuration parameters were used.

The single crystal XRD data were collected in an Oxford-Rigaku Gemini A Ultra diffractometer, using MoKα (λ = 0.71073 Å) radiation at 293(2) K. Data collection, reduction and cell refinement were performed using CRYSLISPRO software [28]. The structures were solved by direct methods through SIR program [29] and refined by SHELXL-2018/3 [30], with the WinGX system [31]. All non-hydrogen atoms were refined with anisotropic thermal parameters. H atoms connected to carbon were placed in idealized positions and treated by rigid model, with Uiso(H) = 1.2Ueq (C or N) for aromatic rings, CH groups and NH of imine group, and Uiso(H) = 1.5Ueq (C) for the methyl group. Figures were drawn using ORTEP-3 for Windows [32] and Mercury [33].

2.2. Experimental octanol-water partition coefficient

The distribution coefficient (P) in the 1-octanol/water system was calculated using the shake flask method. Tris buffer pH 7.4 (10⁻² M) was used as the aqueous phase. The organic and aqueous phases were prepared containing low concentrations of hydrazone (5 × 10⁻⁵ M). The analyses were performed in triplicate and P was calculated as the average concentration ratio Co/Cw, in which Co is the final concentration in the organic phase and Cw is the final concentration in the aqueous phase. Concentrations were estimated from calibration curves using an Agilent™ Cary 100 spectrophotometer.

2.3. Method of continuous variations

The apparent affinity of both ligands for copper(II) ions and the stoichiometry of the reactions were evaluated, in solution, using the Method of Continuous Variations (Job's method) monitored through UV-Vis (Agilent™ Cary 100 spectrophotometer), in triplicates. While this method is mainly used for determining complex stoichiometries, under some specific conditions, such as the formation of only one complex species, little or no overlapping of free and complexed ligand bands, and strong metal-ligand affinity, an apparent constant (*K*_{app}) can be obtained from the data. To do so, initially, the molar absorptivity of the ligand was determined through a calibration curve in HEPES buffer (50 mM, pH 7.4). Then, mixtures of different ligand to metal molar fractions were prepared as usual, from stock solutions of each ligand and CuCl₂·2 H₂O, also in HEPES, at a concentration of 5 × 10⁻⁵ M. The mixtures were stirred at 25 °C and 500 rpm until the moment of analysis. A "theoretical" molar absorptivity for the formed complex is calculated at the point of intersection of the lines using the Lambert-Beer equation. The complex concentration at the equilibrium is then estimated from this ε value according to the maximum experimental absorbance of its band. The free ligand concentration at the equilibrium, on the other hand, is determined from the remaining absorbance of the hydrazone band in the sample of molar fraction related to the observed stoichiometry. Finally, an apparent affinity constant can be characterized considering the equilibrium concentrations of complex, ligand, and metal (calculated taking into account the reaction stoichiometry) by the fundamental equation $K_{app} = \frac{[ML]}{[L][M]}$, valid for a 1:1 complex.

2.4. Ascorbate consumption assay

The ascorbate consumption assay was performed by measuring ascorbate absorbance at 265 nm (ε = 14,500 M⁻¹ cm⁻¹) as a function of time, in an Agilent™ Cary 100 spectrophotometer. A kinetics method was employed, with measurements being registered every 0.1 s. The fragment Aβ₁₋₁₆ (GenScript™, amino acid sequence DAEFRHDS-GYEVHHQK) was employed since it constitutes the coordinating portion of the Aβ peptide. Stock solutions of the evaluated *N*-acylhydrazones (5.00 mM), copper(II) chloride (2.25 mM) and Aβ₁₋₁₆ peptide (2.50 mM) were prepared in ultrapure water, while ascorbate (5.00 mM) was freshly prepared in HEPES buffer (50 mM, pH 7.4) before each measurement. For every experiment, to a 1.0 cm pathlength 3 mL cuvette, 2450 μL of buffer was added, followed by the addition of 50 μL of ascorbate stock solution and, after two minutes, 10 μL of Aβ₁₋₁₆ peptide. 10 μL from Cu²⁺ stock solution was added two minutes later. When the compounds were involved, when absorbance reached ~1 A.U., either 5, 15 or 25 μL were added for 1, 3 and 5 eq. respectively. Thus, final concentrations in the cuvette were: [ascorbate] = 100 μM, [Cu²⁺] = 9 μM, [Aβ₁₋₁₆] = 10 μM, [ligand] = 0, 10, 30 or 50 μM and [HEPES] = 50 mM. Measurements were performed in triplicate. Statistics (*t*-tests with significance level of *p* < 0.05) were performed in GraphPad Prism software.

2.5. Aggregation experiment

A peptide stock solution (577.39 μM) was prepared by dissolving 1 mg of lyophilized synthetic human Aβ₁₋₄₀ (GenScript™) in 400 μL NaOH 10 mM, separated into 20 μL aliquots and kept in -20 °C until analyses. CuCl₂·2 H₂O stock solution (500 μM) was prepared in ultrapure water, while stock solutions of ligands (500 μM) were prepared in HEPES buffer (20 mM, pH 6.6) containing NaCl 150 mM. The turbidity assay was conducted in triplicate in flat-bottomed 96-well assay plates. The reaction mixture (100 μL final volume) in the wells were composed of this buffer solution. Final concentration on the wells were: [Aβ₁₋₄₀] = 25 μM, [Cu²⁺] = 25 μM, [ligand] = 25 or 75 μM. Aggregation was performed in the presence of 7.7 mM sodium azide to prevent biological contamination. The solutions were incubated for 3 h at 37 °C under constant agitation (1100 rpm, KASVI) and absorbance was measured at 405 nm using a Varioskan™ LUX Thermo Scientific™ plate reader. Ligands, metal and buffer were subtracted correspondingly. Alternately, for the copper-containing samples, the same preparation was assembled in black 96-well plates, with addition of 10 μM thioflavin-T, and measured with excitation at 450 nm and emission spectra recorded between 460 and 600 nm after 3 h incubation at 37 °C and 1100 rpm.

Transmission electron microscopy (TEM) images were performed with pooled samples obtained at the end of the aggregation assay. Samples were adhered to a formvar/carbon coated grid and then stained with 2% uranyl acetate solution. Images were acquired with a FEI Tecnai™ T20 electron microscope (National Center for Structural Biology and Bioimaging – CENABIO, UFRJ, Rio de Janeiro, Brazil).

2.6. Protein NMR spectroscopy

These experiments were performed only for the more soluble compound **X1Benz**.

Non-labeled and ¹⁵N isotopically enriched Aβ₁₋₄₀ peptide samples were purchased from EZBiolab (Carmel, IN) and Alexotech (Oslo, Norway), respectively. NMR spectra were acquired on a 600 MHz Avance III (Bruker, Billerica, MA) equipped with a cryogenically cooled triple-resonance ¹H(¹³C/¹⁵N) TCI probe. Heteronuclear NMR experiments were performed with pulsed-field-gradient-enhanced sequences on 80 μM ¹⁵N-labeled peptide samples in 20 mM Tris buffer (pH 7.3) at 15 °C containing 1% of DMSO. 1D ¹H NMR experiments, on the other hand, were acquired on unlabeled Aβ₁₋₄₀ samples under the same

experimental conditions. Aggregation did not occur at such low temperature and in the absence of stirring.

For the mapping experiments, ^1H – ^{15}N heteronuclear single quantum correlation (HSQC) amide cross-peaks affected during **X1Benz** titration were identified by comparing their chemical shifts with those of the same cross-peaks in the data set of samples lacking the compound. Mean weighted chemical shift displacements (^1H – ^{15}N MWCS) were calculated as $[(\Delta\delta\ ^1\text{H})^2 + (\Delta\delta\ ^{15}\text{N})^2/25]^{1/2}$ [34]. Acquisition and processing of NMR spectra were performed using TOPSPIN 7.0 (Bruker Biospin). 2D spectra analysis and visualization were performed with CCPN.

3. Results and discussion

3.1. Characterization of the ligands

Both hydrazones were obtained in the hydrochloride form since the N2 imidazole nitrogen is protonated in the synthesis due to the acidic conditions employed.

X1Benz, the simpler, unsubstituted **X1TMP** derivative, was isolated as a white crystalline solid, which adopts the monoclinic system, space group $P2_1/c$. Crystal, data collection and refinement parameters are summarized in Table 1, while selected bond distances, as well as important bond and dihedral angles, can be found in Table 2. The ORTEP representation is displayed in Fig. 1A. As expected, **X1Benz** exhibits an (*E*)-configuration around its C4–N3 double bond. There are no intramolecular H bonds. Each unit cell (Fig. 1B) contains four **X1Benz**-derived cations, four chloride anions and twelve water molecules. The only direct hydrazone-hydrazone interactions are π - π stacking contacts involving 1-methylimidazole and hydrazone-derived benzene rings of two neighboring **HX1Benz**⁺ units (centroid-centroid distance: 3.532 Å). On the other hand, an intricate network of conventional and unconventional H bonds connects, in a rather indirect manner, these pairs through crystallization water molecules and chloride counter-ions, giving rise to unidimensional zig-zag chains parallel to the crystallographic axis *b*. Geometric parameters for such interactions are displayed in Table 3.

Typically, hydrazones have a rich solution chemistry involving (*E*)/(*Z*) isomers, *anti*/*syn* conformations and amido/iminol tautomers, that can be studied through ^1H NMR spectroscopy [20]. Nevertheless, our own experience indicates that the hydrochlorides of *N*-acylhydrazones containing 1-methylimidazole usually display just one set of signals in

Table 2

Selected geometric parameters for compound **X1Benz**.

Bond distance (Å)		Bond angle (°)		Torsion angle (°)	
C3–C4	1.447(2)	C3–C4–N3	115.6(1)	C3–C4–N3–N4	–178.9(1)
C4–N3	1.272(2)	C4–N3–N4	118.2(1)	C4–N3–N4–C5	176.7(1)
N3–N4	1.356(2)	N3–N4–C5	117.6(1)	N3–N4–C5–C6	–178.9(1)
N4–C5	1.365(2)	N4–C5–C6	116.4(1)	N3–N4–C5–O1	1.2(2)
C5–O1	1.223(2)	N4–C5–O1	121.5(1)	C7–C6–C5–O1	–14.2(2)
C5–C6	1.489(2)	C6–C5–O1	122.5(1)		

DMSO- d_6 solution, suggesting the presence of only one major constituent in solution. This is also the case for both studied ligands herein, **X1TMP** and **X1Benz**, as can be seen in Fig. 2A and B, respectively. The main difference between both spectra is related to the signals at 3.74 (3H) and 3.88 (6H) ppm, assigned to the three methoxyl substituents in **X1TMP**. This also implies a lesser number of aromatic signals for this compound. NMR spectroscopy shows that both compounds were obtained at a high purity level. On the other hand, carbon NMR spectra are shown in Fig. S4.

3.2. Pharmacological parameters

Both compounds are in accordance with the Lipinski's Rule of Five, *i. e.*, $\log P \leq 5$ (partition coefficient), $\text{MW} \leq 500\ \text{g mol}^{-1}$ (molecular weight), $\text{HBA} \leq 10$ (hydrogen bond acceptors) and $\text{HBD} \leq 5$ (hydrogen bond donors) [35]. These rules allow for a good theoretical prediction of the oral bioavailability and permeability of new molecules. Calculated values for $\log P$ and other important descriptors, are shown in Table 4.

A smaller MW is related to easier cellular membrane crossing. In this sense, the majority of drugs orally administered currently in the market present MW in the range of 200–450 g mol^{-1} [36], like the synthesized *N*-acylhydrazones **X1TMP** and **X1Benz**. $\log P$ represents the hydrophilic-lipophilic balance of the molecule that, combined with the solubility of the compound in aqueous solution ($\log S$), is of extreme importance in the context of cellular permeability. A compromise between them must be reached in order for the potential drug to cross the lipid bilayer of the membranes. Finally, PSA is the polar surface area, which evaluates the degree of polarity of the molecule. Regarding blood-brain barrier crossing, it has been reported that compounds should exhibit a PSA of $<90\ \text{Å}^2$ [37]. In this sense, both metallophores are in agreement with such guideline.

Other parameters that can be taken into account in the analysis of a drug candidate are the Druglikeness and the DrugScore. The first is determined from the comparison of compound fragments with databases of both commercially available drugs and non-drug compounds. The latter, on the other hand, is a combination of the previously mentioned properties and expected toxicity risks in one value that is used to estimate the compound's overall potential to qualify for a drug. No indication of mutagenicity or tumorigenicity was found for the *N*-acylhydrazones **X1TMP** and **X1Benz**, nor any warnings for irritating or reproductive effects. For this reason, DrugScore values obtained were above 90%.

Apart from the calculated $\log P$ parameter, we determined its experimental values for both synthesized *N*-acylhydrazones through the shake flask method. A Tris buffer pH 7.40 was employed as the aqueous phase and 1-octanol was used as the organic phase. Nowadays the optimal range of $\log P$ values for blood-brain barrier crossing is considered between 0 and 3 [38]. The values obtained for **X1TMP** and **X1Benz** are, respectively, 1.55 ± 0.17 and 1.49 ± 0.13 , close to the predicted values and inside the ideal range. It is important to note that, from the calculations, it was expected a lower $\log P$ for the mescaline derivative **X1TMP**, which was not experimentally observed, since both hydrazones presented virtually the same value for this parameter. Moreover, despite the similarity of the calculated $\log S$, a lower water solubility was experimentally observed for **X1TMP**, indicating that the

Table 1

Crystal, data collection and refinement parameters for compound **X1Benz**.

Formula	$\text{C}_{12}\text{H}_{19}\text{N}_4\text{O}_4\text{Cl}$
Formula weight (g mol^{-1})	318.76
Crystal system	Monoclinic
Space group	$P2_1/c$
<i>a</i> (Å)	9.4095(6)
<i>b</i> (Å)	23.9779(10)
<i>c</i> (Å)	7.4947(5)
$\alpha = \gamma$ (°)	90.00
β (°)	110.961(8)
<i>V</i> (Å ³)	1579.05(18)
<i>Z</i>	4
Temperature (K)	293(2)
Crystal size (mm)	$0.42 \times 0.52 \times 1.00$
μ (Mo K α) (mm^{-1})	0.263
Refl. measured/ independent	20,662 / 4022
R_{int}	0.0322
Refined parameters	191
R_{obs} [$F_o > 2\sigma(F_o)$]	0.0436
R_{all}	0.0668
wR_{obs} [$F_o^2 > 2\sigma(F_o)^2$]	0.1043
wR_{all}	0.1185
<i>S</i>	1.020
$\Delta\rho_{\text{max}}, \Delta\rho_{\text{min}}$ (e Å^{-3})	0.310 / -0.226

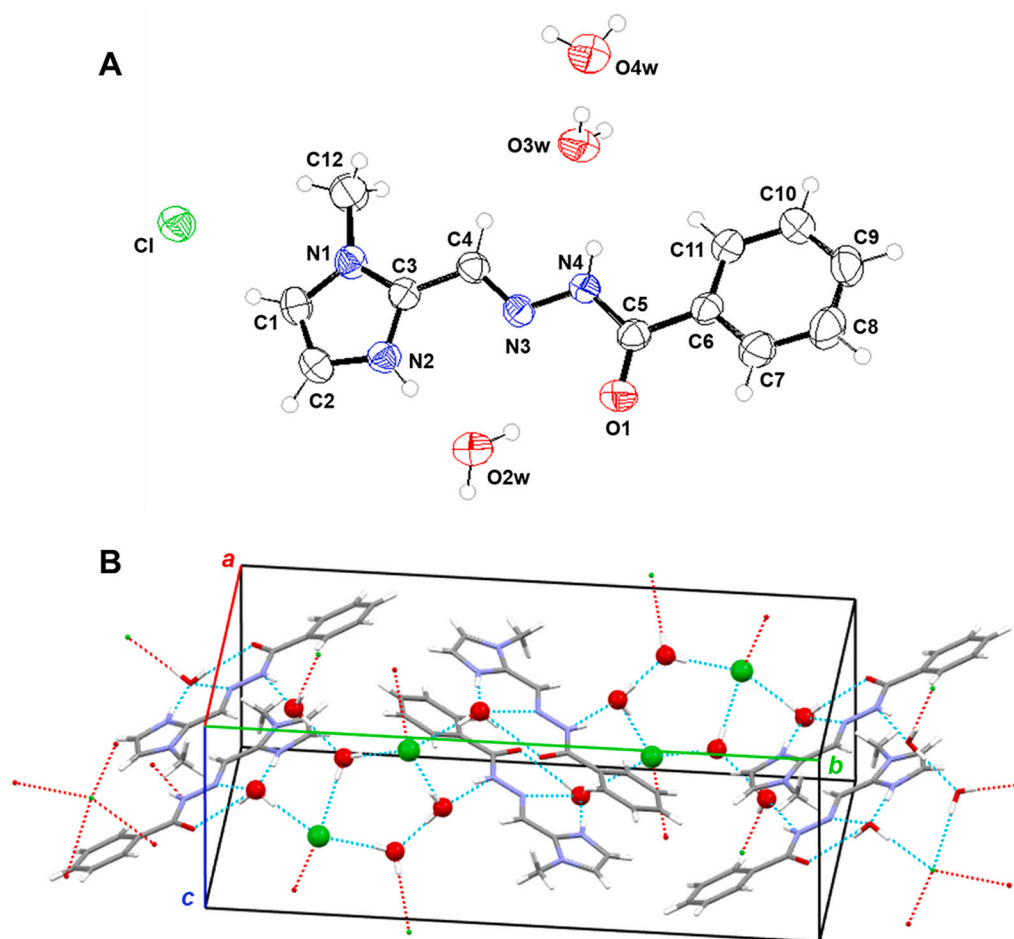


Fig. 1. Crystal structure of *N*-acylhydrazone **X1Benz**. (A) ORTEP representation. Ellipsoids were drawn at the 50% probability level. (B) Unit cell packing and intermolecular interactions.

Table 3
H-bonding parameters for compound **X1Benz**.

D–H A	D–H (Å)	H...A (Å)	D...A (Å)	D–H...A (°)
N2–H2 O2w	0.86	1.87	2.727(2)	173.0
N4–H4 O3w	0.80	2.05	2.818(2)	159.0
O2w–H2a Cl ⁱ	0.91	2.22	3.130(2)	174.0
O2w–H2b O1	0.83	2.15	2.959(2)	163.0
O2w–H2b N3	0.83	2.47	2.975(2)	120.0
O3w–H3a O4w	0.88	1.91	2.786(2)	174.0
O3w–H3b Cl ⁱⁱ	0.85	2.30	3.141(2)	170.0
O4w–H4a Cl ⁱⁱⁱ	0.79	2.44	3.223(2)	174.0
O4w–H4b Cl ^{iv}	0.84	2.34	3.178(2)	174.0

Symmetry code: *i* (1 + *x*, *y*, *z*); *ii* (−*x*, −*y*, −*z*); *iii* (−*x*, ½ + *y*, ½ − *z*); *iv* (−*x*, −*y*, 1 − *z*).

presence of the methoxyl substituents somewhat impairs its solubility in the biological fluid. This trend is contrary to what would be expected from the theoretical relative PSA values. Nevertheless, **X1TMP** still presents enough solubility that allowed us to work in physiological-like conditions for most of the experiments.

3.3. Interactions with copper(II) in buffered, pH 7.4, aqueous solution

The Method of Continuous Variations (Job Method) using UV–Vis spectroscopy as a suitable monitoring technique, was applied to estimate the apparent affinity of both ligands towards copper(II) ions. The electronic spectra of **X1TMP** and **X1Benz** display only one main intra-ligand band each, centered at 318 nm ($\epsilon = 23,950 \pm 110 \text{ M}^{-1} \text{ cm}^{-1}$) and

315 nm ($\epsilon = 25,660 \pm 125 \text{ M}^{-1} \text{ cm}^{-1}$), respectively. Upon complexation, those absorptions undergo strong bathochromic shifts to 380 and 372 nm, correspondingly (Fig. 3A and B). On the other hand, no copper (II) characteristic *d-d* band was observed due to the low concentration employed in this assay.

In both cases, the maximum absorbance was achieved at the molar fraction of 0.5 (Fig. 3A and B, insets), suggesting the formation of ML stoichiometry complexes. **X1TMP** and **X1Benz** seem to interact with copper(II) ions in a similar manner and with analogous affinities. While **X1TMP** showed an apparent log *K* of 5.74 ± 0.15 , **X1Benz** presented a slightly higher apparent log *K* value, equal to 5.87 ± 0.11 . The fact that both constants were obtained under exactly the same experimental conditions makes a direct comparison between them perfectly reliable. Thus, we can conclude that the electronic effects derived from the inclusion of methoxyl substituents in the phenyl group do not appear to cause major changes in the affinity of the ligands for copper(II) ions, which, for both hydrazones, is in the moderate range expected for a functional metallophore.

Our previous works involving 1-methylimidazole-containing *N*-acylhydrazones have shown that these compounds exhibit a higher water solubility and a remarkable resistance towards hydrolysis [23,24]. This allowed us to work in buffered 100% aqueous media for ROS production and A β aggregation assays, a more physiological condition.

3.4. Interactions with the copper(II)-A β system: Effect on ROS production

Free copper is highly effective in the generation of ROS through the cycling between its two physiologically available oxidation states [39].

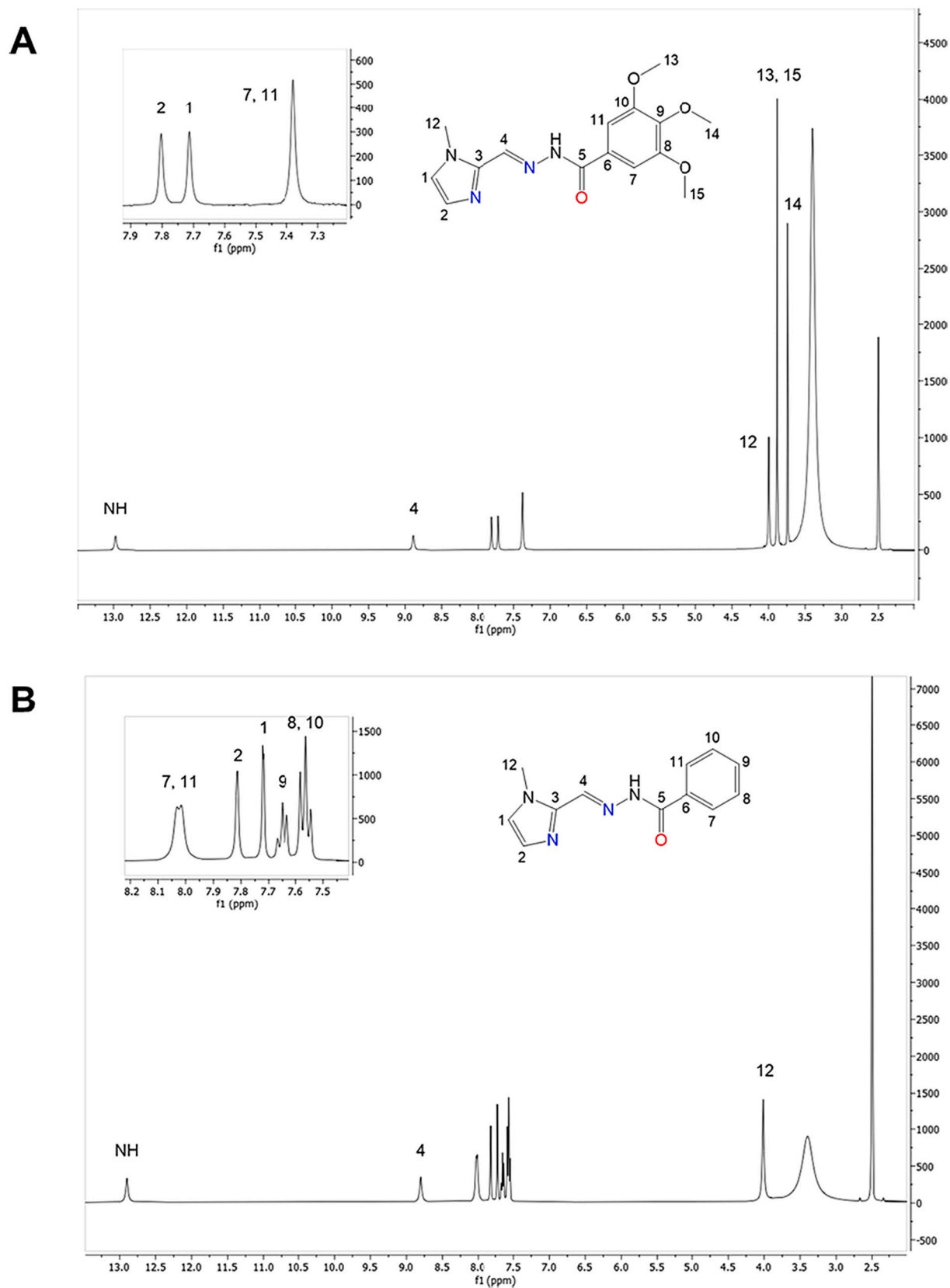


Fig. 2. ^1H NMR spectra (400 MHz) of the studied *N*-acylhydrazones in $\text{DMSO}-d_6$ at 25°C . (A) δ_{X1TMP} : 3.74 (s, 3H), 3.88 (s, 6H), 4.00 (s, 3H), 7.38 (s, 2H), 7.71 (s, 1H), 7.80 (s, 1H), 8.89 (s, 1H), 12.97 (s, 1H). (B) δ_{X1Benz} : 4.01 (s, 3H), 7.56 (t, 2H), 7.65 (t, 1H), 7.72 (d, 1H), 7.81 (s, 1H), 8.02 (d, 2H), 8.80 (s, 1H), 12.90 (s, 1H). s: singlet; t: triplet; d: doublet.

Table 4

Calculated (OSIRIS Property Explorer: DataWarrior™) descriptors of pharmaceutical relevance for **X1Benz** and **X1TMP**. MW: molecular weight, cLog P: calculated partition coefficient, cLog S: calculated water solubility, PSA: polar surface area.

	MW (g mol ⁻¹)	cLog P	cLog S	PSA (Å ²)	Druglikeness	DrugScore
X1TMP	318.00	1.17	-1.54	86.97	12.08	93%
X1Benz	228.00	1.38	-1.48	59.28	6.03	95%

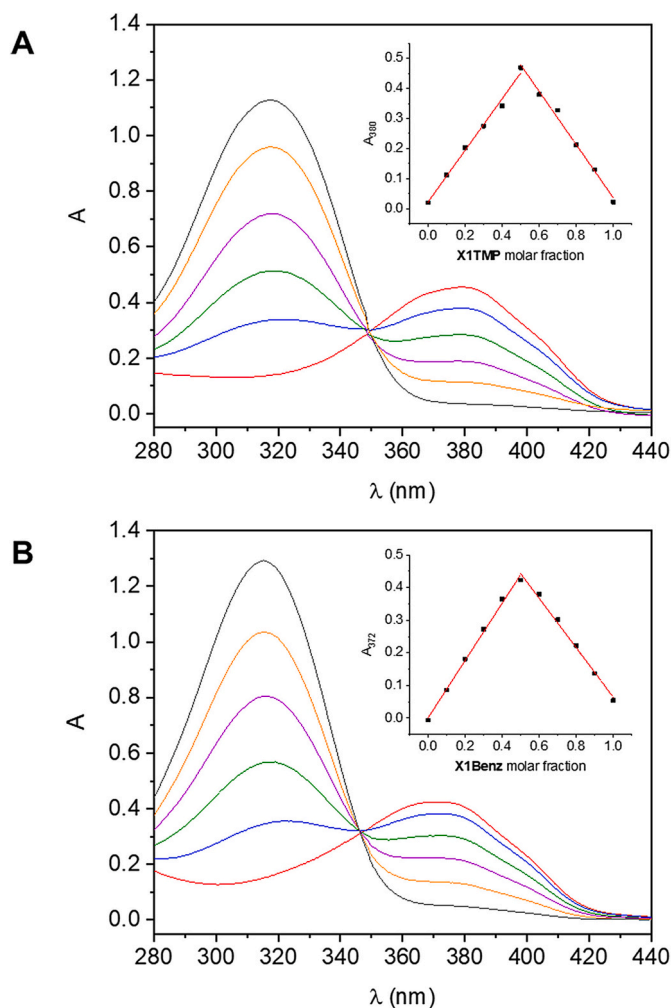


Fig. 3. Method of continuous variations to evaluate the binding affinity of the new hydrazones (A) **X1TMP** and (B) **X1Benz** towards copper(II) – representative electronic spectra of ligand molar fractions from 0.5 to 1.0. *Insets:* absorbance versus molar fraction plots. HEPES buffer (50 mM, pH 7.4), 25 °C.

Although certainly less than free copper, the Cu(A β) complex is still quite competent in catalyzing the production of ROS in the presence of dioxygen and ascorbate. In fact, ascorbate consumption mirrors ROS production and can be employed as a useful assay to determine the efficacy of copper-targeted metallophores in reducing oxidative stress [40,41]. *N*-acylhydrazones **X1TMP** and **X1Benz** showed the ability to reduce copper-mediated ROS production in the preliminary study performed in the presence of A β ₁₋₁₆ (Fig. 4). This fragment was used as a model for copper coordination with respect to the full-length peptide, since it comprises the binding region for the oxidized form of this metal [42].

The addition of copper(II) to a solution containing ascorbate and A β ₁₋₁₆ at pH 7.4 triggers an intensity reduction of the ascorbate

absorption band centered at 265 nm. The initial consumption rate was estimated as $37.9 \pm 4.1 \mu\text{M min}^{-1}$. After addition of 1 eq. of each hydrazone, we observed that the consumption profile does not change appreciably until the ascorbate concentration reaches 50% of its original value. From that moment on, a clear divergence can be noticed (gray box in Fig. 4). The slope of the consumption curves (inset), normalized with respect to the Cu(A β) control condition, was employed as a measurement of the ascorbate oxidation rate at 25 °C. The bar graphs indicate that both compounds are able to reduce the ROS production by around 30–40%, being **X1TMP** slightly more active. The addition of a hydrazone excess (3 eq.) further prevents ascorbate oxidation. At this ratio, **X1TMP** is able to inhibit up to 60% of the reaction, against the 50% of hampering related to **X1Benz**. Another indication of the protective effect of the compounds can be assessed by the time needed to reach the equilibrium (when a variation in absorbance is no longer noticeable). While the Cu(A β) system stabilizes after 20 min, addition of **X1TMP** delays stabilization to around 30 min (1 eq.) and 35 min (3 eq.). Concerning the unsubstituted **X1Benz**, the values are around 25 min (1 eq.) and 35 min (3 eq.). Taken together, and in spite of the inherent limitations of the method, these data indicate that the presence of the studied *N*-acylhydrazones hinders ascorbate oxidation and, therefore, Cu(A β)-mediated ROS production.

3.5. Inhibition of A β aggregation via turbidity assay

Besides catalyzing the production of ROS, copper binding to A β also accelerates its amyloidogenic aggregation, as well as increases neuronal toxicity [43]. Therefore, the next step in our investigation was to evaluate whether the synthesized *N*-acylhydrazone metallophores would be able to interfere with this essential process as well. Since protein aggregates are known to scatter light in the visible region, we carried out a turbidity assay to determine the impact of the ligands in copper-mediated A β ₁₋₄₀ aggregation [44]. The pH of the medium was adjusted to slightly acidic (buffer solution at pH 6.6), since it has been described that optimal metal-binding leading to aggregation occurs under these specific conditions [11,45]. TEM and thioflavin-T fluorescence spectroscopy were used as supporting techniques in order to characterize the aggregates formed.

First, we assessed the effect of the compounds in the absence of copper(II) ions. Interestingly, equimolar amounts of both *N*-acylhydrazones were able to radically prevent aggregation, as can be observed in Fig. 5A (bars 1–3). This was confirmed through TEM images, which show the characteristic fibril formation in the untreated A β sample (panel 5B) and its absence upon treatment with 1 eq. of **X1TMP** (5C) or **X1Benz** (5D).

Regarding the metal-induced process, it is important to note that copper is known to preferably stabilize intermediate oligomeric species over the well-structured, insoluble amyloid fibrils [46,47]. Thus, the presence of this physiological metal slightly increases solution turbidity in comparison to free A β , being the precipitate clearly characterized as mainly amorphous by TEM (dotted bar –4- on Fig. 5A and image in panel 5E) and confirmed through thioflavin-T assay, which indicates a fibrillization lessening of >50% (Fig. S5). The addition of 1 eq. of *N*-acylhydrazones **X1TMP** or **X1Benz** significantly reduces absorbance at 405 nm, indicating a hampering of the aggregation process (light gray bars –5 and 7- in Fig. 5A). Representative microscopy images of the aggregates formed can be observed in panels 5F-G, which seem to present similar nature to those generated in the absence of the metallophores, although in fewer amounts. Once again, thioflavin-t-tests confirm a further reduction in fibrils' development (Fig. S5A).

Finally, when an excess (3 eq.) of ligand is present, there is an *a priori* unexpected increase in the media turbidity for both metallophores, in comparison to the samples treated with only 1 eq. of the compounds (dark gray bars –6 and 8- in Fig. 5A), probably due to precipitation of the uncharged, poorly water soluble bis(hydrazone)copper(II) species, as described recently by us for the related system Cu²⁺-HPCFur, in the

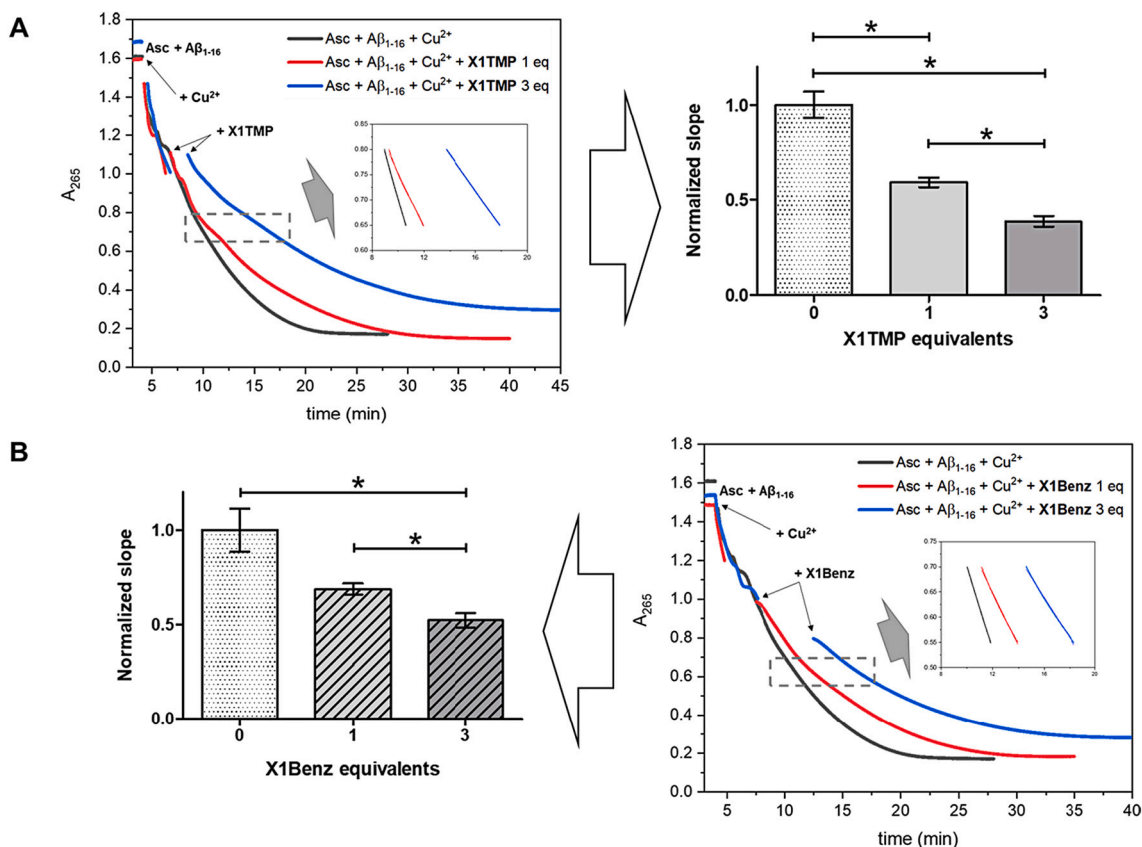


Fig. 4. Cu(Aβ)-induced ascorbate consumption. (A) **Left:** Representative plots showing ascorbate consumption through absorbance decrease at 265 nm for Cu(Aβ) (black), Cu(Aβ) + 1 eq. **X1TMP** (red) and Cu(Aβ) + 3 eq. **X1TMP** (blue). The sharp increase observed after compound addition in excess is due to the intrinsic absorbance of the resulting Cu(**X1TMP**) interaction. *Inset:* Linear segment of the ascorbate consumption curve for $0.80 \leq A_{265} \leq 0.65$. Figures of merit: black line slope: -0.09018 ± 0.00009 , $R^2 = 0.999$; red line slope: -0.05430 ± 0.00009 , $R^2 = 0.996$; blue line slope: -0.036210 ± 0.000008 , $R^2 = 1.000$. **Right:** Bar graph representing the normalized mean slopes of the linear segments, which parallel ROS production, for each condition tested. Significant differences (*t*-tests) are characterized by (*) for $p < 0.05$. (B) **Right:** Representative plots showing ascorbate consumption through absorbance decrease at 265 nm for Cu(Aβ) (black), Cu(Aβ) + 1 eq. **X1Benz** (red) and Cu(Aβ) + 3 eq. **X1Benz** (blue). The sharp increase observed after compound addition in excess is due to the intrinsic absorbance of the resulting Cu(**X1Benz**) interaction. *Inset:* Linear segment of the ascorbate consumption curve for $0.70 \leq A_{265} \leq 0.55$. Figures of merit: black line slope: -0.08240 ± 0.00005 , $R^2 = 1.000$; red line slope: -0.05267 ± 0.00007 , $R^2 = 0.997$; blue line slope: -0.03997 ± 0.00004 , $R^2 = 0.997$. **Left:** Bar graph representing the normalized mean slopes of the linear segments.

presence of a decapeptide at pH around 7 [48]. In fact, this can also be observed in TEM, through the presence of regions with material accumulation consisting of crystals of the putative neutral [Cu(**X1TMP**)₂] (needle-like) or [Cu(**X1Benz**)₂] (sheet-like) complexes associated with mostly amorphous protein precipitation (panels 5H–I, respectively). Thioflavin-T fluorescence assays (Fig. S5B) show a slight fibrillization increase in this samples, close to that observed for the Cu(Aβ) sample itself.

3.6. Mechanistic insights through 1D- and 2D-NMR experiments

As NMR spectroscopy requires higher compounds' concentrations, experiments were performed only with **X1Benz**, the most water soluble hydrazone.

Since both metallophores seem to impair Aβ aggregation, even in the absence of copper(II), we decided to investigate this system by firstly analyzing the interactions of **X1Benz** directly with Aβ₁₋₄₀, using ¹H–¹⁵N heteronuclear single quantum correlation (HSQC) spectroscopy. The central region of the spectrum of an 80 μM sample of uniformly ¹⁵N-labeled Aβ is shown in Fig. 6A (black contours). Resonances are well resolved and sharp, with a limited dispersion of chemical shifts, reflecting the disordered nature and the high degree of mobility of the backbone. Upon titration with increasing concentrations of **X1Benz**, the ¹H–¹⁵N HSQC spectra retained the excellent resolution of the free

peptide but presented measurable chemical shift changes in a discrete number of residues distributed throughout its amino acid sequence (Figs. 6A –blue/red contours- and 6B). Close analysis of the backbone amide signals exhibiting chemical shift changes upon interaction with **X1Benz** revealed that they correspond to amino acids located in the proximity of aromatic residues, namely: a Phe residue in position 4, a Tyr residue in 10, as well as two Phe residues (positions 19 and 20). Altogether, these results unequivocally demonstrate that **X1Benz** binds to the monomeric form of Aβ₁₋₄₀, with aromatic residues possibly playing a very important role as anchoring moieties for binding of this compound to the peptide. It is worth noting that such a behavior was quite unexpected, not observed for other *N*-acylhydrazones previously described by our research group [18,20].

Additional experiments are clearly needed to determine if the identified **X1Benz** binding sites at positions F4, Y10, and F19–20 constitute independent, non-interactive motifs, consistent with the binding of at least three **X1Benz** molecules per peptide unit, and to fully characterize the interaction modes and binding strengths.

The copper(II) sequestering potential of **X1Benz** towards Aβ₁₋₄₀ was explored at single residue resolution by 1D ¹H NMR spectroscopy. As reported earlier [18], addition up to 1 eq. of Cu²⁺ to Aβ₁₋₄₀ samples caused the severe broadening of specific resonances, clearly indicating their involvement as metal coordinating sites for this physiological ion (Figs. 7A and B). Interestingly, increasing amounts of **X1Benz** were not

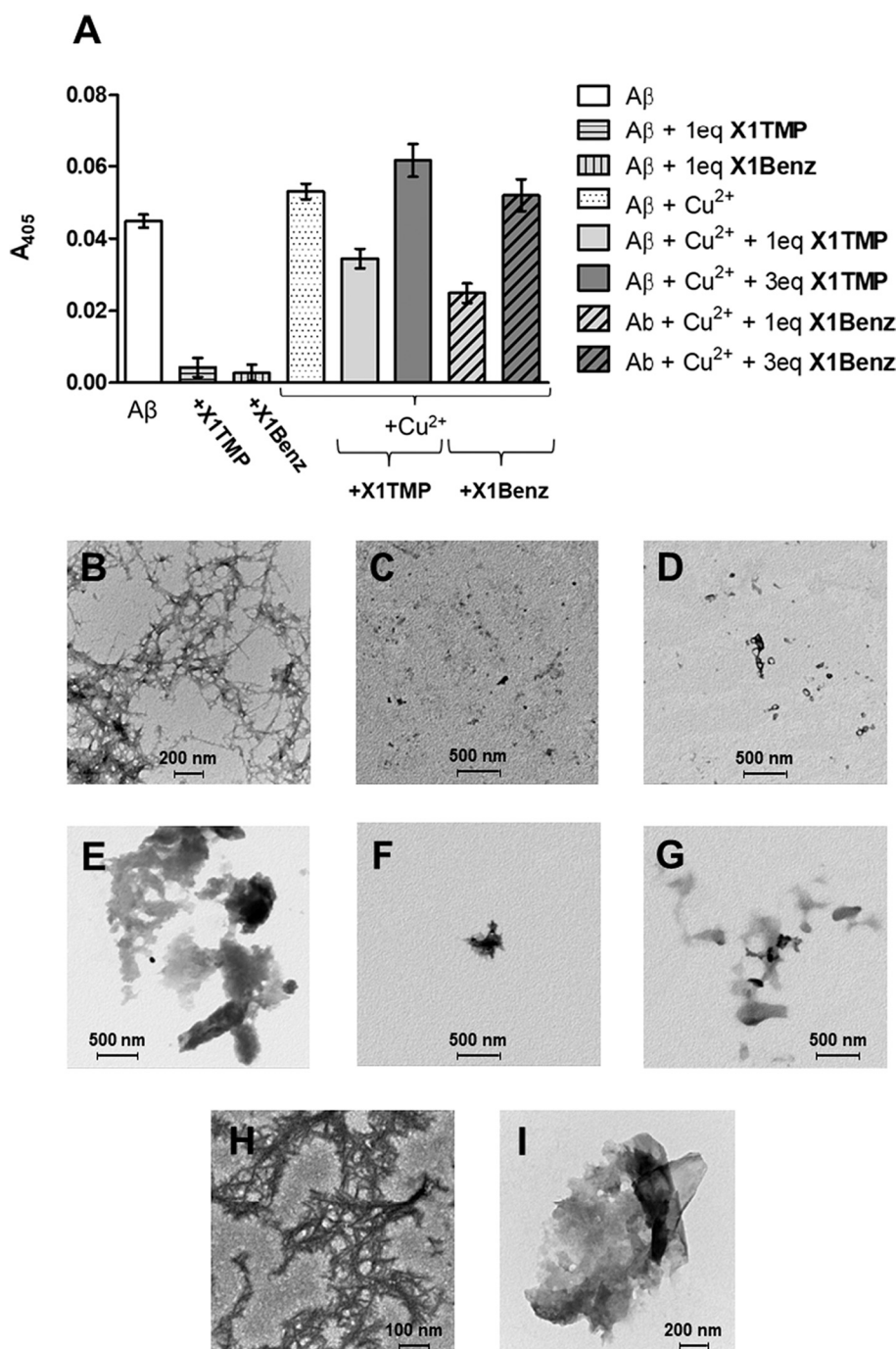


Fig. 5. A β_{1-40} aggregation in the absence and presence of copper(II) and the *N*-acylhydrazones, in HEPES 20 mM, NaCl 150 mM, pH 6.6, 37 °C and 1100 rpm after 3 h. (A) Aggregation as measured by turbidity at 405 nm. Data are reported as mean and standard deviation. (B–I) Transmission Electron Microscopy (TEM) of the different conditions of the assay: (B) A β (C) A β + 1 eq. X1TMP (D) A β + 1 eq. X1Benz (E) A β + 1 eq. Cu²⁺, hereafter referred to as Cu(A β) (F) Cu(A β) + 1 eq. X1TMP (G) Cu(A β) + 1 eq. X1Benz (H) Cu(A β) + 3 eq. X1TMP (I) Cu(A β) + 3 eq. X1Benz.

efficient at removing the metal-induced perturbations in A β backbone amides, even upon the addition of 5 eq. of the compound (Fig. 7C). However, the broadening effects observed on the signals belonging to X1Benz might be an indicative of copper(II) coordination by this compound, probably generating a ternary A β -copper-X1Benz species. Such a result is in perfect agreement with our previously reported findings regarding the formation of ternary complexes involving *N*-acylhydrazones, Cu²⁺ and small prion protein fragments [21,24]. In the context of the present work, it seems that this ternary species is the one responsible for impairing ROS production and preventing A β aggregation.

In order to verify the formation of a ternary A β -copper-X1Benz complex through a different experimental technique, we obtained UV-Vis spectra of freshly prepared 1:1 (Cu:A β_{1-16}), 1:1 (Cu:X1Benz) and 1:1:1

(Cu:A β_{1-16} :X1Benz) mixtures in 20 mM, pH 7.3 Tris buffer solution (Fig. S6). While binary Cu(A β) species virtually does not absorb light in the studied region, the Cu(X1Benz) system showed an overlapped multi-band absorption pattern centered at 360 nm. The ternary A β -copper-X1Benz mixture, instead, exhibited a different spectral profile, with the most prominent band centered at 320 nm. Very similar results were obtained by May, Jancsó & Enyedy [49] for a ternary complex involving copper(II), the tetrapeptide DAHK and the thiosemicarbazone Triapine.

On the other hand, addition of EDTA completely abolishes metal-interactions with both A β and X1Benz (Fig. 7D). Nevertheless, some signals of the free peptide (Fig. 7A) and the hydrazone (Fig. 7E) cannot be recovered, especially, in the latter, those related to the imidazole moiety. In fact, the spectrum in Fig. 7D is exactly the same obtained for a sample containing only A β + 5 eq. X1Benz (not shown), suggesting that

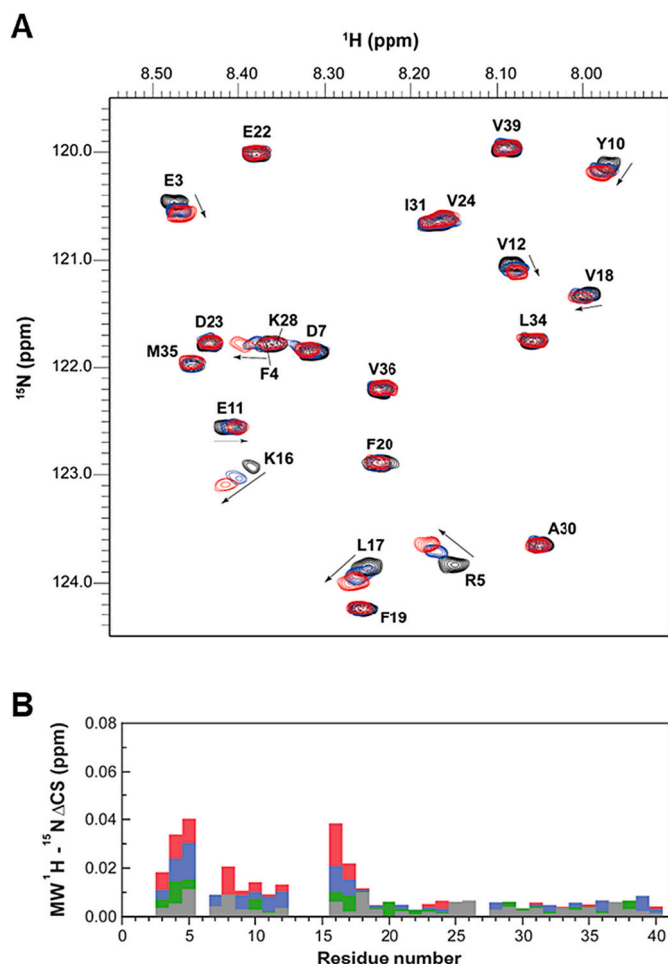


Fig. 6. NMR analysis of **X1Benz** binding to $A\beta_{1-40}$. (A) Overlaid contour plots of $^1H-^{15}N$ HSQC spectra of $A\beta$ in the absence (black) and presence of increasing **X1Benz** concentrations: 3 eq. (blue) and 5 eq. (red). Most affected residues are labeled (for the sake of simplicity, the one letter amino acid code was employed). (B) Differences in the mean weighted chemical shift ($MW^1H-^{15}N\Delta CS$) displacements between free and **X1Benz**-bound $A\beta$ at molar ratios of 1:1 (gray), 2:1 (green), 3:1 (blue) and 5:1 (red). Experiments were recorded at 15 °C (80 μM $A\beta$ in Tris 20 mM pH 7.3).

$A\beta$ -**X1Benz** interactions are preserved. Thus, the general broadening observed on $A\beta$ resonances upon addition of EDTA is consistent with the occurrence of a peptide's self-association process, probably mediated by **X1Benz**.

4. Conclusions

The *N*-acylhydrazones **X1TMP** and **X1Benz** were obtained in the hydrochloride form, with good yields and high purity. Calculated and experimental log *P* values are very similar for both compounds, and within the ideal 0–3 range. Theoretical PSA were, respectively, 87.0 and 59.3 Å². In general, all physico-chemical parameters evaluated are in accordance with the guidelines for drugs targeting the CNS.

Upon interaction with copper(II) ions, relevant in the context of Alzheimer's disease, both hydrazones preferably generate an ML complex, as demonstrated by the Job Method. Comparable ligand-to-metal affinities were obtained, with apparent log *K* values in aqueous buffered medium of 5.74 ± 0.15 and 5.87 ± 0.11 , respectively, for **X1TMP** and **X1Benz**, indicating that the presence of methoxyl substituents in the former does not greatly influence the stability of the copper(II) complex formed.

Both compounds are able to lessen the production of ROS by the Cu

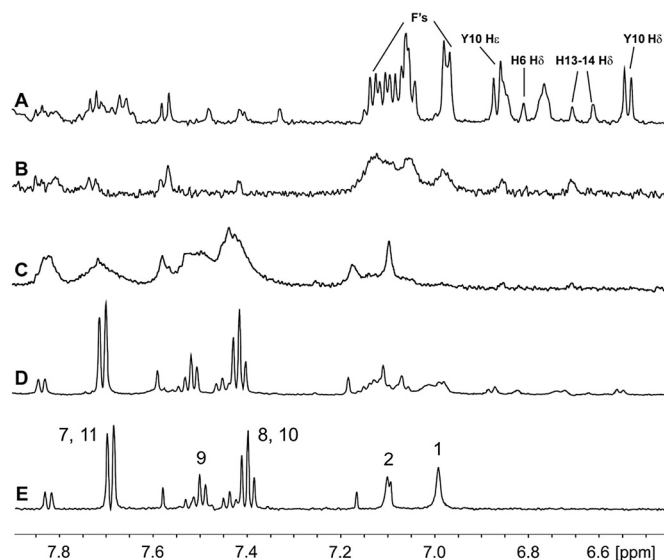


Fig. 7. 1H NMR of the aromatic side chains of $A\beta_{1-40}$ in the presence of copper (II) and **X1Benz**. Spectra were registered at 15 °C in Tris 20 mM pH 7.3 of samples containing (A) $A\beta$ (80 μM) (B) $A\beta$ + 1 eq. Cu^{2+} (C) $A\beta$ + 1 eq. Cu^{2+} + 5 eq. **X1Benz** (D) $A\beta$ + 1 eq. Cu^{2+} + 5 eq. **X1Benz** followed by addition of 10 mM EDTA. Spectral region with the resonances of 400 μM **X1Benz** are shown in (E) along with the signals' assignment. For the sake of simplicity, the one letter amino acid code was employed.

($A\beta$)-system under pseudo-physiological conditions, with **X1TMP** being slightly more effective than **X1Benz**. Additionally, the hydrazones have the capacity of preventing $A\beta$ aggregation at equimolar conditions in the presence and, quite unexpectedly, in the absence of copper. 2D $^1H-^{15}N$ HSQC NMR experiments demonstrated a direct interaction between $A\beta$ and **X1Benz**, which can be at the core of this phenomenon. On the other hand, the activity behind the inhibition of copper-mediated $A\beta$ aggregates formation may be related to a 1:1:1 ternary species, as demonstrated for **X1Benz** by 1D 1H NMR.

The data reported herein certainly reinforce the relevance of ternary species in the mode of action of *N*-acylhydrazones as metallophores in the context of metal-enhanced neurodegeneration. The formation of such complexes can impair the production of ROS through steric- or kinetic-related mechanisms. Regarding the peptide's aggregation, once again, the formation of $A\beta$ -copper-hydrazone adducts seems to drive the emergence of "off-pathway" aggregates, which cannot mature into fibrils, as supported by TEM images and thioflavin-T assays. Altogether with our previous works, these findings may suggest the need to adapt the current definition of metallophore in order to include not only those ligands that compete with the protein for the metal ion, but the ones that exercise their activity by the formation of stable, mostly inert, ternary species as well. In fact, the relative reactivity / toxicity of this kind of aggregates is under investigation and will be the subject of future reports.

Finally, the relatively low solubility of **X1TMP** in comparison to that of **X1Benz** will probably not represent a problem to its potential use as a metallophore, since the concentrations required to exert such a role in the central nervous system are usually very small, of the order of a few milligrams per kilogram of weight.

Overall, the novel 1-methylimidazole-containing *N*-acylhydrazones **X1TMP** and **X1Benz** have shown promising prospects as agents for the treatment of AD, and deserve further studies in biophysical and pre-clinical models of the disease.

Accession code

CCDC 2195202 contains the supplementary crystallographic data for

X1Benz. These data can be obtained free of charge via www.ccdc.cam.ac.uk/data_request/cif, or by emailing data_request@ccdc.cam.ac.uk, or by contacting Cambridge Crystallographic Data Centre, 12 Union Road, Cambridge CB2 1EZ, UK; fax: +44 1223 336033.

Declaration of Competing Interest

DSC and NAR are inventors of technology protected by the Pontifical Catholic University of Rio de Janeiro through Brazilian (BR1020200054236) and international (PCT/BR2021/050107) patent applications, involving a series of 1-methylimidazole-2-carboxaldehyde-derived *N*-acylhydrazones and their use in the treatment of both amyloid and non-amyloid aggregopathies. Apart from this, authors declare no competing interest.

Acknowledgements

Authors are grateful to the scientific Brazilian funding agencies CNPq (Conselho Nacional de Desenvolvimento Científico e Tecnológico, Brazil), CAPES (Coordenação de Aperfeiçoamento de Pessoal de Nível Superior, Brazil), FAPERJ (Fundação Carlos Chagas Filho de Amparo à Pesquisa do Estado do Rio de Janeiro, Brazil), FAPEMIG (Fundação de Amparo à Pesquisa do Estado de Minas Gerais, Brazil) and FINEP (Financiadora de Estudos e Projetos, Brazil). We also acknowledge CENABIO (Centro Nacional de Biologia Estrutural e Bioimagem, UFRJ, Brazil), for the access to the TEM facility. The authors thank LAMEM-UFF (Laboratório Multiusuário de Espectrometria de Massas da Universidade Federal Fluminense) for the mass spectrometry analyses.



This work is dedicated to the memory of Professor Ademir Neves. Thank you very much for the teachings and for the example of a committed, rigorous and, at the same time, enthusiastic scientist. Paraphrasing Aldous Huxley, the student who comes back from Professor Ademir's lab will never be quite the same as the one who went out.

Appendix A. Supplementary data

Supplementary data to this article containing a synthetic scheme for the reported *N*-acylhydrazones **X1TMP** and **X1Benz**, their mid-infrared, ESI-MS(+) and ¹³C NMR spectra, as well as complementary thioflavin-T assays and UV-Vis measurements can be found online at <https://doi.org/10.1016/j.jinorgbio.2022.112033>

References

- [1] A. De Falco, D.S. Cukierman, R.A. Hauser-Davis, N.A. Rey, Doença De Alzheimer: hipóteses etiológicas e perspectivas de tratamento, *Química Nova* 39 (2016) 63–80.
- [2] J.W. Kinney, S.M. Bemiller, A.S. Murtishaw, A.M. Leisgang, A.M. Salazar, B. T. Lamb, Inflammation as a central mechanism in Alzheimer's disease, *Alzheimers Dement (N Y)* 4 (2018) 575–590.
- [3] A. Serrano-Pozo, M.P. Froesch, E. Masliah, B.T. Hyman, Neuropathological alterations in Alzheimer disease, *Cold Spring Harb. Perspect. Biol.* 3 (12) (Dec, 2011).
- [4] H.M. Brothers, M.L. Gosztyla, S.R. Robinson, The physiological roles of amyloid- β peptide hint at new ways to treat Alzheimer's disease, *Front. Aging Neurosci.* 10 (2018) 118.
- [5] J.E. Morley, S.A. Farr, Hormesis and amyloid- β protein: physiology or pathology? *J. Alzheimers Dis.* 29 (3) (2012) 487–492.
- [6] B. Penke, F. Bogár, G. Paragi, J. Gera, L. Fülöp, Key peptides and proteins in Alzheimer's disease, *Curr. Protein Pept. Sci.* 20 (6) (2019) 577–599.
- [7] M.P. Lambert, A.K. Barlow, B.A. Chromy, C. Edwards, R. Freed, M. Liosatos, T. E. Morgan, I. Rozovsky, B. Trommer, K.L. Viola, P. Wals, C. Zhang, C.E. Finch, G. A. Krafft, W.L. Klein, Diffusible, nonfibrillar ligands derived from Abeta1-42 are potent central nervous system neurotoxins, *Proc. Natl. Acad. Sci. U. S. A.* 95 (11) (May, 1998) 6448–6453.
- [8] E.N. Cline, M.A. Bicca, K.L. Viola, W.L. Klein, The amyloid- β oligomer hypothesis: beginning of the third decade, *J. Alzheimers Dis.* 64 (s1) (2018) S567–S610.
- [9] T. Kowalik-Jankowska, M. Ruta, K. Wiśniewska, L. Lankiewicz, Coordination abilities of the 1-16 and 1-28 fragments of beta-amyloid peptide towards copper(II) ions: a combined potentiometric and spectroscopic study, *J. Inorg. Biochem.* 95 (4) (2003) 270–282. Jul 01.
- [10] P. Dorlet, S. Gambarelli, P. Faller, C. Hureau, Pulse EPR spectroscopy reveals the coordination sphere of copper(II) ions in the 1-16 amyloid-beta peptide: a key role of the first two N-terminus residues, *Angew. Chem. Int. Ed. Eng.* 48 (49) (2009) 9273–9276.
- [11] C.D. Syme, R.C. Nadal, S.E. Rigby, J.H. Viles, Copper binding to the amyloid-beta (Abeta) peptide associated with Alzheimer's disease: folding, coordination geometry, pH dependence, stoichiometry, and affinity of Abeta-(1-28): insights from a range of complementary spectroscopic techniques, *J. Biol. Chem.* 279 (18) (2004) 18169–18177. Apr 30.
- [12] L. Wang, Y.L. Yin, X.Z. Liu, P. Shen, Y.G. Zheng, X.R. Lan, C.B. Lu, J.Z. Wang, Current understanding of metal ions in the pathogenesis of Alzheimer's disease, *Transl. Neurodegener.* 9 (2020) 10.
- [13] M. Rana, A.K. Sharma, Cu and Zn interactions with A β peptides: consequence of coordination on aggregation and formation of neurotoxic soluble A β oligomers, *Metallomics* 11 (1) (2019) 64–84, 01 23.
- [14] A.K. Sharma, S.T. Pavlova, J. Kim, L.M. Mirica, The effect of Cu(2+) and Zn(2+) on the A β 42 peptide aggregation and cellular toxicity, *Metallomics* 5 (11) (Nov, 2013) 1529–1536.
- [15] D.P. Smith, D.G. Smith, C.C. Curtain, J.F. Boas, J.R. Pilbrow, G.D. Ciccotosto, T. L. Lau, D.J. Tew, K. Perez, J.D. Wade, A.I. Bush, S.C. Drew, F. Separovic, C. L. Masters, R. Cappai, K.J. Barnham, Copper-mediated amyloid-beta toxicity is associated with an intermolecular histidine bridge, *J. Biol. Chem.* 281 (22) (2006) 15145–15154. Jun 02.
- [16] S. Parthasarathy, B. Yoo, D. McElheny, W. Tay, Y. Ishii, Capturing a reactive state of amyloid aggregates: NMR-based characterization of copper-bound Alzheimer disease amyloid β -fibrils in a redox cycle, *J. Biol. Chem.* 289 (14) (2014) 9998–10010. Apr 04.
- [17] L.E. Scott, C. Orvig, Medicinal inorganic chemistry approaches to passivation and removal of aberrant metal ions in disease, *Chem. Rev.* 109 (10) (Oct, 2009) 4885–4910.
- [18] R.A. Hauser-Davis, L.V. de Freitas, D.S. Cukierman, W.S. Cruz, M.C. Miotto, J. Landeira-Fernandez, A.A. Valiente-Gabioud, C.O. Fernández, N.A. Rey, Disruption of zinc and copper interactions with A β (1-40) by a non-toxic, isoniazid-derived, hydrazone: a novel biometal homeostasis restoring agent in Alzheimer's disease therapy? *Metallomics* 7 (2015) 743–747. April 01.
- [19] D.S. Cukierman, A.B. Pinheiro, S.L. Castineiras-Filho, A.S. da Silva, M.C. Miotto, A. De Falco, T.P. de Ribeiro, S. Maisonette, A.L. da Cunha, R.A. Hauser-Davis, J. Landeira-Fernandez, R.Q. Aucélio, T.F. Outeiro, M.D. Pereira, C.O. Fernández, N. A. Rey, A moderate metal-binding hydrazone meets the criteria for a bioinorganic approach towards Parkinson's disease: therapeutic potential, blood-brain barrier crossing evaluation and preliminary toxicological studies, *J. Inorg. Biochem.* 170 (May, 2017) 160–168.
- [20] D.S. Cukierman, E. Accardo, R.G. Gomes, A. De Falco, M.C. Miotto, M.C.R. Freitas, M. Lanznaster, C.O. Fernández, N.A. Rey, Aroylhydrazones constitute a promising class of 'metal-protein attenuating compounds' for the treatment of Alzheimer's disease: a proof-of-concept based on the study of the interactions between zinc(II) and pyridine-2-carboxaldehyde isonicotinoyl hydrazone, *J. Biol. Inorg. Chem.* 23 (8) (Dec, 2018) 1227–1241.
- [21] D.S. Cukierman, N. Bodnár, B.N. Evangelista, L. Nagy, C. Kállay, N.A. Rey, Impact of pyridine-2-carboxaldehyde-derived aroylhydrazones on the copper-catalyzed oxidation of the M112A PrP, *J. Biol. Inorg. Chem.* 24 (8) (2019) 1231–1244, 12.
- [22] A. De Falco, G.C. Kincheski, E. Atrián-Blasco, C. Hureau, S.T. Ferreira, N.A. Rey, The aroylhydrazone INHHQ prevents memory impairment induced by Alzheimer's-linked amyloid- β oligomers in mice, *Behav. Pharmacol.* 31 (8) (Dec, 2020) 738–747.
- [23] D.S. Cukierman, D.F. Lázaro, P. Sacco, P.R. Ferreira, R. Diniz, C.O. Fernández, T. F. Outeiro, N.A. Rey, X1INH, an improved next-generation affinity-optimized hydrazone ligand, attenuates abnormal copper(I)/copper(II)- α -Syn interactions

- and affects protein aggregation in a cellular model of synucleinopathy, *Dalton Trans.* 49 (45) (Nov, 2020) 16252–16267.
- [24] D.S. Cukierman, N. Bodnár, R. Diniz, L. Nagy, C. Kállay, N.A. Rey, Full Equilibrium picture in aqueous binary and ternary systems involving copper(II), 1-methylimidazole-containing hydrazonic ligands, and the 103–112 human prion protein fragment, *Inorg. Chem.* 61 (1) (2022) 723–737.
- [25] D.S. Cukierman, N.A. Rey, Tridentate N-acylhydrazones as moderate ligands for the potential management of cognitive decline associated with metal-enhanced neuroaggregopathies, *Front. Neurol.* 13 (2022), 2022-February-16.
- [26] B.K. Cassels, P. Sáez-Briones, Dark classics in chemical neuroscience: mescaline, *ACS Chem. Neurosci.* 9 (10) (2018) 2448–2458.
- [27] C.M. Stork, S.M. Schreffler, P. Wexler, Peyote, Academic Press, Oxford, 2014, pp. 841–843.
- [28] O. Rigaku, CrysAlis PRO. Rigaku Oxford Diffraction, Yarnton, England, 2015.
- [29] M.C. Burla, R. Caliandro, B. Carrozzini, G.L. Casciarano, C. Cuocci, C. Giacovazzo, M. Mallamo, A. Mazzone, G. Polidori, Crystal structure determination and refinement via SIR2014, *J. Appl. Crystallogr.* 48 (1) (2015) 306–309.
- [30] G.M. Sheldrick, Crystal structure refinement with SHELXL, *Acta Crystallogr. C Struct. Chem.* 71 (Pt 1) (Jan, 2015) 3–8.
- [31] L.J. Farrugia, WinGX and ORTEP for Windows: an update, *J. Appl. Crystallogr.* 45 (4) (2012) 849–854, 2020/05/11.
- [32] C. Barnes, ORTEP-3 for Windows - a version of ORTEP-III with a Graphical User Interface (GUI) by J. Farrugia, *J. Appl. Crystallogr.* 30 (5 Part 1) (1997) 568.
- [33] C.F. Macrae, I.J. Bruno, J.A. Chisholm, P.R. Edgington, P. McCabe, E. Pidcock, L. Rodriguez-Monge, R. Taylor, J. Van De Streek, P.A. Wood, Mercury CSD 2.0—new features for the visualization and investigation of crystal structures, *J. Appl. Crystallogr.* 41 (2) (2008) 466–470, 2020/03/18.
- [34] J. Cavanagh, N.J. Skelton, W.J. Fairbrother, M. Rance, A.G. Palmer, *Protein NMR Spectroscopy: Principles and Practice*, Elsevier, Amsterdam, 2006.
- [35] C.A. Lipinski, F. Lombardo, B.W. Dominy, P.J. Feeney, Experimental and computational approaches to estimate solubility and permeability in drug discovery and development settings, *Adv. Drug Deliv. Rev.* 46 (1–3) (Mar, 2001) 3–26.
- [36] P.D. Leeson, R.J. Young, Molecular property design: does everyone get it? *ACS Med. Chem. Lett.* 6 (7) (2015) 722–725, Jul 09.
- [37] H. van de Waterbeemd, G. Camenisch, G. Folkers, J.R. Chretien, O.A. Raevsky, Estimation of blood-brain barrier crossing of drugs using molecular size and shape, and H-bonding descriptors, *J. Drug Target.* 6 (2) (1998) 151–165.
- [38] H. Pajouhesh, G.R. Lenz, Medicinal chemical properties of successful central nervous system drugs, *NeuroRx* 2 (4) (Oct, 2005) 541–553.
- [39] G. Multhaup, C.L. Masters, *Metal Ions in Biological Systems Volume 36: Interrelations Between Free Radicals and Metal Ions in Life Processes*, CRC Press, 1999, p. 365.
- [40] A. Conte-Daban, A. Day, P. Faller, C. Hureau, How Zn can impede Cu detoxification by chelating agents in Alzheimer's disease: a proof-of-concept study, *Dalton Trans.* 45 (39) (Oct, 2016) 15671–15678.
- [41] E. Atrián-Blasco, M. Del Barrio, P. Faller, C. Hureau, Ascorbate oxidation by Cu (Amyloid- β) complexes: determination of the intrinsic rate as a function of alterations in the peptide sequence revealing key residues for reactive oxygen species production, *Anal. Chem.* 90 (9) (May, 2018) 5909–5915.
- [42] P. Faller, C. Hureau, Bioinorganic chemistry of copper and zinc ions coordinated to amyloid-beta peptide, *Dalton Trans.* 7 (Feb, 2009) 1080–1094.
- [43] F. Hane, Z. Leonenko, Effect of metals on kinetic pathways of amyloid- β aggregation, *Biomolecules* 4 (1) (2014) 101–116.
- [44] D. Hall, R. Zhao, I. Dehlsen, N. Bloomfield, S.R. Williams, F. Arisaka, Y. Goto, J. A. Carver, Protein aggregate turbidity: Simulation of turbidity profiles for mixed-aggregation reactions, *Anal. Biochem.* 498 (2016) 78–94, Apr 01.
- [45] C.S. Atwood, R.D. Moir, X. Huang, R.C. Scarpa, N.M. Bacarra, D.M. Romano, M. A. Hartshorn, R.E. Tanzi, A.I. Bush, Dramatic aggregation of Alzheimer abeta by Cu (II) is induced by conditions representing physiological acidosis, *J. Biol. Chem.* 273 (21) (May, 1998) 12817–12826.
- [46] K. Przygońska, M. Pacewicz, W. Sadowska, J. Poznański, W. Bal, M. Dadlez, His6, His13, and His14 residues in A β 1–40 peptide significantly and specifically affect oligomeric equilibria, *Sci. Rep.* 9 (1) (2019) 9449, 07 01.
- [47] E. Stefaniak, E. Atrián-Blasco, W. Goch, L. Sabater, C. Hureau, W. Bal, The aggregation pattern of A β 1–40 is altered by the presence of N-truncated A β 4–40 and/or CuII in a similar way through ionic interactions, *Chem. Eur. J.* 27 (8) (2021) 2798–2809, 2022/10/01.
- [48] D.S. Cukierman, C.B.P. Ligiero, R.R. de Avillez, N.A. Rey, Crystal Structure and Hirshfeld Analysis of a Poorly Water Soluble Bis(ligand)copper(II) Complex Containing the Metallophore Pyridine-2-Carboxaldehyde 2-Furoyl Hydrazone, 2022.
- [49] N.V. May, A. Jancsó, É.A. Enyedy, Binding models of copper(II) thiosemicarbazone complexes with human serum albumin: a speciation study, *Molecules* 26 (9) (2021).